Three-Dimensional Virus Scaffolds for Energy Storage and Microdevice Applications

By

F. John Burpo

B.S. Aerospace Engineering, United States Military Academy
M.S. Chemical Engineering, Stanford University

SUBMITTED TO THE DEPARTMENT OF
BIOLOGICAL ENGINEERING
IN PARTIAL FULFILLMENT OF THE REQUIREMENT OF THE DEGREE OF

DOCTORATE OF PHILOSOPHY

AT THE
MASSACHUSETTS INSTITUTE OF TECHNOLOGY

JANUARY 2012
[February 2012]

Signature of Author: _____

F. John Burpo
Department of Biological Engineering
January 6, 2012

Certified By: _____

Angela M. Belcher
Professor of Materials Science and Engineering and Biological Engineering
Thesis Supervisor

Accepted By: _____

Forest White
Chair, Course XX Graduate Program Committee
Associate Professor of Biological Engineering

Three-Dimensional Virus Scaffolds for Energy Storage and Microdevice Applications

By F. John Burpo

Submitted To the Department of Biological Engineering in Partial Fulfillment of the Requirements for the Degree of Doctor of Philosophy

Abstract

With constantly increasing demand for lightweight power sources, electrode architectures that eliminate the need for conductive and organic additives will increase mass specific energy and power densities. The increased demand for lightweight power is coupled with increasing device miniaturization. As the scale of devices decreases, current battery technologies add mass on the same scale as the device itself. A dual functional electro-mechanical material that serves as both the device structural material and the power source would dramatically improve device integration and range for powered movement.

To address the demand for lightweight power with the objective of a dual functional electro-mechanical material, the M13 bacteriophage was used to create novel 3-dimensional nano-architectures. To synthesize 3-dimensional nanowire scaffolds, the M13 virus is covalently linked into a hydrogel that serves as a 3-dimensional bio-template for the mineralization of copper and nickel nanowires. Control of nanowire diameter, scaffold porosity, and film thickness is demonstrated. The nanowire scaffolds are found to be highly conductive and can be synthesized as free-standing films.

To demonstrate the viability of the 3-dimensional nanowire networks for electrical energy storage, copper nanowires were galvanically displaced to a mixed phase copper-tin system. These tin based anodes were used for lithium rechargeable batteries and demonstrated a high storage capacity per square area and stable cycling approaching 100 cycles.

To determine the viability of the 3-dimensional nanowire networks as dual functional electro-mechanical materials and the mechanical stability of processing intermediates, phage hydrogels, aerogels, and metal nanowire networks were examined with nano-indentation. The elastic moduli of the metal networks are in the range of open cell metal foams

The demonstration of 3-dimensional virus-templated metal nanowire networks as electrically conductive and mechanically robust should facilitate their implementation across a broad array of device applications to include photovoltaics, catalysis, electrochromics, and fuel cells.

Thesis Advisor: Angela M. Belcher
Title: Professor of Materials Science Engineering and Biological Engineering

Thesis Committee: Professor Douglas A. Lauffenbuger, Professor Donald R. Sadoway

BIOGRAPHICAL NOTE

EDUCATION

Present	Ph.D. Candidate, Biological Engineering, Massachusetts Institute of Technology
2002	M.S. Chemical Engineering, Stanford University
1992	B.S. Aerospace Engineering, United States Military Academy, West Point

PROFESSIONAL EXPERIENCE

2011-2012	U.S. Army War College, Military Fellow in the MIT Security Studies Program
2004-2005	Command and General Staff College, Fort Leavenworth, KS
2002-2004	Assistant Professor and Instructor of Biochemistry and General Chemistry, Department of Chemistry and Life Science, United States Military Academy, West Point, NY.
1992-Present	Army Officer, United States Army. Assignments include airborne, Vicenza, Italy; mechanized-armor, Fort Hood, TX; and Stryker, Fort Lewis, WA. Operational deployments include Rwanda, Bosnia and Iraq.

AWARDS

2011-2012	Selection as a Senior Service College Fellow, Security Studies Program, MIT
2008-2011	Army Fully Funded Graduate Fellowship, Massachusetts Institute of Technology
2008-2011	Energy Fellow, Massachusetts Institute of Technology
2007	Selection as a tactical artillery battalion commander, Unites States Army
2006	Selection as an Academy Professor, United States Military Academy, West Point
2005	MacArthur Writing Award. U.S. Army Command and General Staff College
2000-2002	Army Fully-Funded Graduate Fellowship, Stanford University
1992-Present	Military Awards & Decorations. *Badges*: Combat Action Badge, Senior Parachutist Badge, Air Assault Badge, Ranger Tab, German Jump Wings. *Individual Awards*: Bronze Star, Purple Heart, Meritorious Service Medal (2xOLC), Army Commendation Medal (5xOLC), Army Achievement Medal (1xOLC), National Defense Service Medal, Armed Forces Expeditionary Medal, Global War on Terror Service Medal, Armed Forces Service Medal, Humanitarian Service Medal, Army Service Ribbon, Overseas Service Ribbon (2), NATO Medal. *Unit Awards*: Joint Meritorious Unit Award, Meritorious Unit Commendation, Army Superior Unit Award

TABLE OF CONTENTS

LIST OF FIGURES

LIST OF TABLES

LIST OF ACRONYMS

AFM	Atomic Force Microscope
ALD	Atomic Layer Deposition
CVD	Chemical Vapor Deposition
E3 (E4)	E3 bacteriophage with three glutamatic acid residues on the p8 coat protein. Mutation from E4 with four glutamates led to E3, which has three gluatamates and one aspartate residue.
EDS/EDX	Energy Dispersive X-Ray Spectroscopy; EDS used interchangeably with EDX
ELD	Electroless Deposition
ESEM	Environmental Scanning Electron Microscope
FIB	Focused Ion Beam
FTO	Fluorine-doped Tin Oxide
ITO	Indium Tin Oxide
LPEI	Linear Polyethylenimine
M13	M13 filamentous bacteriophage
MEMS	Microelectricalmechanical systems
NNW	Nano-Network
p3	Protein 3 on the M13 virus; a proximal end protein
p8	Protein 8 on the M13 virus; the capsid coat protein
PAA	Polyacrylic Acid
PEM	Polyelectrolyte Multilayer
PEG	Polyethylene Glycol
PET	Polyethylene Terephthalate
SEM	Scanning Electron Microscope
SWCNT	Single Wall Carbon Nanotubes
TEM	Transmission Electron Microscope
Y21M	M13 phage with a tyrosine to methionine mutation at the 21st amino acid position on the p8 protein; "stiff phage"

CHAPTER 1

Introduction

1.1 Background and Significance

The demand for electrical energy storage is ubiquitous and ever increasing with new devices introduced almost daily. The micro to industrial scale dimensions of these devices comes with a commensurate scale of electrical energy storage requirements. Lithium rechargeable batteries have emerged as a high energy density means to address a wide range of this demand, but the increase of battery storage capacity has not increased at a rate similar to other technologies such as transistor density in the computer industry.[1] The numerous battery design parameters, many of which work at cross purposes, create a field that is both challenging and open to novel approaches. Many of these challenges are more pronounced for small scale batteries.[2] In addition to the demands of material handling and processing conditions, specific capacity at this scale suffers from the addition of conductive matrices and organic binders.[3] Micro to macro scale battery assembly approaches that do not require these additional materials would present a significant advantage in specific storage capacity. Recent work in microbatteries indicates a 10 fold capacity advantage for 3D compared to 2D electrode architectures.[4] These architectures involve nanorods grown perpendicularly to the current collector, providing an advantage for increased capacity, lower electrode resistance, benign reaction conditions, and fewer assembly steps compared to solid state thin film and micro-batteries. Thin film and micro-battery capacity increases would benefit the powering of micro-electromechanical systems (MEMS) devices and microelectronic circuits for greater periods of time than currently available.[5]

1.2 Biotemplating Overview

While at first biological systems may not have appeared as a route to solve the challenges of traditionally inorganic materials, they have emerged as a means to nucleate, synthesize and organize a broad array of materials at the nanoscale.[6, 7] Biological soft templates provide a wide diversity of architectures on which to build inorganic structures. Where these natural systems developed over an evolutionary time scale, genetic manipulation enables the rapid development of biological organisms assayed against conditions they do not normally encounter in nature.[8] This creates a nearly endless combination of possibilities for nanomaterials development and manipulation.

M13 filamentous bacteriophage. The M13 filamentous bacteriophage offers a genetically tunable platform to engineer binding specificities that facilitate the synthesis of specific inorganic material crystal structures and assembly into increasingly complex architectures. The M13 virus is a 880nm long particle with a 6.5nm diameter. The nearly micron long capsid is axially covered with 2,700 copies of the pVIII (p8) protein, with five copies of the pIII (p3) and pVI (p6) proteins each at the proximal end of the phage and roughly five copies each of the pVII (p7) and pIX (p9) proteins forming a blunt distal end.[9] In principle all five surface exposed proteins are genetically modifiable, with p3, p8, and p9 being the most solvent exposed. The filamentous phage can be successively exposed to a target substrate and enriched for high affinity sequences for the desired protein in a process known as phage display or biopanning.[10] Rationally designed sequences may also be achieved via site directed mutagenesis and gene insertions.

M13 E3/4 bacteriophage. Predictive design led to a tetraglutamate fusion to the N-terminus of the p8 capsid protein, providing four carboxylic acid residues to electrostatically

bind cations in solution.[11] This E4 clone offers the versatility of facile binding of metal cations and the tunability of surface charge via pH. The functional carboxylic acid group on glutamate residues has a pK_a of 4.3.[12] Zeta potential testing of the E4 clone revealed an isolelectric point of 4.3.[13] When tyrosine is mutated to mehtionine at the 21st position on the p8 protein, the E3 virus can increase its persistence length by a factor of 5.[14] In this work this clone will be referred to interchangeably as Y21M and as "stiff phage."

Our group used M13 phage display and rational design to great advantage and demonstrated its broad versatility in developing viruses to recognize and mineralize specific crystal structures of semiconductor materials,[8, 15] ordering quantum dots, [16] and synthesize a variety of electrode materials for lithium rechargeable batteries.[11, 17, 18] Further, various viral self assembly techniques were demonstrated using liquid crystal ordering with high concentration phage solutions, and 2-dimensional assembly on polymer thin films.[13, 19, 20] Self-assembly of inorganic materials and of viral nanowires using wet-bench chemistry at ambient conditions with environmentally benign materials provides significant benefits for battery electrodes. The bacteriophage's high aspect ratio of approximately 130 offers a high surface area to volume ratio for mineralized nanowires creating small ion diffusion distances and high packing densities.

1.3 Biotemplating for Energy Devices

Biotemplating has been demonstrated as an effective means of ordering materials at the nanoscale. A wide array of biological templates has been used to direct the assembly of numerous metal, metal oxide and semiconducting materials. This approach provides a low-cost method when compared to traditional manufacturing techniques. On the other hand, there has been only limited demonstration of 3-dimensional ordering of biotemplates. DNA origami is one

example, but one that relies on numerous custom designed oligonucleotide sequences. A facile 3-dimensional assembly approach using a single biotemplate monomer would greatly advance the field of biotemplating.

M13 bacteriophage based battery devices. The M13 bacteriophage was used to develop a range of electrode materials for lithium rechargeable batteries. Both cathode and anode materials were developed, with synthesis strategies employed to increase conductivity for less conductive active materials. To synthesize Co_3O_4 nanowires for use as battery anodes, the E4 virus was incubated in cobalt chloride solution followed by reduction with $NaBH_4$. The resulting Co_3O_4 nanocrystals yielded a 600mAh/g stable capacity over 20 charge-discharge cycles. To achieve higher rate capacities, the viruses were assembled with a phagemid system where the introduction of a separate plasmid into the *E.coli* host expressed a gold binding p8 protein that assembled with the tetraglutamate fusions. The resulting phage particles presented a small percentage of randomly incorporated gold binding proteins on its coat. The hybrid system nanowires contained approximately 2.5% gold mass and generated significantly higher current densities and a specific capacity 30% higher than the Co_3O_4 nanowires without gold incorporation.

The ability to synthesize inorganic electrode nanowires on M13 phage was then coupled to the ability to order the virus on a layer-by-layer (LbL) polyelectrolyte membrane (PEM) film. Layer-by-layer assembly of two polyions of opposite charge creates ultrathin films, that depending on the choice of polyelectrolyte can serve as a solid polymer electrolyte.[21-23] The alternation of linear polyethylenimine (LPEI) and polyacrylic acid (PAA) yields a superlinear film growth, whereby LPEI polymer interdiffusion between layers creates a progressively thicker positively charged top layer.[13, 17, 20] Positively charged LPEI deposition on a negatively charged

substrate such as a plasma treated silicon wafer followed by rinsing with de-ionized water and subsequent deposition of PAA constitutes one bilayer. The additional deposition of LPEI adds a half layer, with the nomenclature convention of $(LPEI/PAA)_n$, where n is the number of bilayers. Two dimensional phage ordering was initially attempted by depositing virus on 4.5 bilayer films with additional deposition of bilayers. This caused the virus to successively diffuse to the top surface and gain increasing 2D order.[13] Ultimately, it was determined that beyond a critical number of LPEI/PAA biliayers, virus solutions order in a single deposition due to the lateral diffusional mobility of LPEI, which in turn allows for the 2-dimensional ordering of the viral particles. The concentration and pH of both the film polyelectrolytes and the virus solutions significantly influence the degree of ordering.[20] A LPEI and PAA solution pH of 5 facilitates the optimal virus ordering by minimizing particle overlap and clustering. The density of virus deposition on the film is controlled within a pH range of 4.8-5.4. Binding density increases with decreasing pH. pH values below this range result in disordered aggregates, and pH values above the range result in sparse binding.

The PEM film provides an excellent means of controlling the ordering the M13 virus in two dimensions. Using a polydimethylsiloxane (PDMS) stamp with raised 4μm and 8μm circular pads, layer-by-layer films were developed and coated with ordered E4 phage. Synthesis of Co_3O_4 nanowires on the viral film resulted in a single viral layer of electrode material. The PDMS pads, coated with a LPEI/PAA multilayer film and cobalt oxide nanowire layer were then stamped onto platinum electrodes and galvanostatically tested with a lithium counter electrode between 26-255nA. The estimated capacity of each individual stamped electrode was between 625pA and 725pA. The estimate is complicated by the lack of a known mass of electrode

material and a small capacity of platinum at slow discharge rates. Consequently, no specific capacity was determined.

An interesting feature of the nanowire synthesis on the 2D polyelectrolyte bound viral film is the apparent loss of order observed prior to the synthesis to after the cobalt oxide synthesis. It is speculated here that the increased ionic strength of the initial cobalt chloride incubation solution and the progressive mineralization of the viral particles decreases the ionic interaction between the p8 coat proteins and the underlying positive LPEI film layer. The resulting nanowires present the appearance of a convoluted thin mesh rather than linearly aligned metalized wires with planar aligned axes. It is undetermined if the nanowires are physically connected and whether that possible contiguous mesh of nanowires contributed to the rate performance of the electrodes. The nature of a single layer viral film as nanowire templates limits the micro-battery capacity to a relatively fixed z-height, and consequently battery capacity becomes a function of film surface area.

Our group next explored the use of the M13 virus to template lithium iron phosphate cathodes.[18] The low cost of materials and more benign environmental impact make iron phosphate an attractive electrode material.[24] To overcome the high resistivity of this electrode material, two strategies were employed. First, similar to the incorporation of gold particles in cobalt oxide nanowires, silver nanoparticles were first bound to the viral coat with amorphous iron phosphate mineralized over the silver particles and the remainder of the viral p8 coat proteins. Unlike the gold incorporation into cobalt oxide which used a phagemid system for a low percentage random incorporation of gold binding p8 proteins, the E4 virus was used to bind silver nanoparticles and mineralize iron phosphate. Biopanning the E4 virus p3 protein against single wall carbon nanotubes (SWCNT) generated a two-gene phage system that allowed the

creation of a conductive mesh connecting the virus particles. Where electrode active material contacts can dislocate after repeated battery cycling, the carbon nanotubes provide a more robust wiring of the electrode that maintains a stable capacity beyond 50 cycles. The rate performance of the carbon nanotube binding phage significantly improved both low and high discharge rates. A C/10 (theoretical capacity discharged over 10 hours) discharge capacity improved from 143mAh/g for E4 only, to 170mAh/g with carbon nanotube incorporation. At a 3C discharge (theoretical capacity discharged in 20 minutes), carbon nanotube binding improved the electrode capacity to 134mAh/g over the best reported rate for lithium iron phosphate of 80mAh/g.

Continued electrode material develop in our group demonstrates E4's broad versatility to nucleate and mineralize a range of alloys. Ensuring high rate discharge capacity is a continuing challenge for many electrode materials due the disrupted active material particle contacts.[1, 25, 26] Volume expansion and contraction accompanies the intercalation and de-intercalation of lithium into and from the active material. Coating active materials with conductive carbon and rolling the electrode with an organic binder aids in maintaining the electrical pathway between active material particles. However, over repeated cycling, crack development and propagation can lead to the loss of electrical contact between active material particles and conductive carbon and ultimately to electrode pulverization. The high aspect ratio of viral template nanowires provides the benefit of low relative volume expansion and high entanglement and consequent electrical contact of nanowires. The factors of microstructure, material composition, grain orientation, and electrode/electrolyte interactions significantly impact the assembly of thin films in general,[27] and microbatteries in particular.

1.4 Multi-Functional Materials Vision

As battery powered devices continue on a miniaturization pathway, current battery systems will be unable to provide power due to two limiting factors: 1) available area and volume for battery incorporation, and 2) the added mass from the battery system may be on the order of the mass of the objective device, which would significantly impact those miniaturized systems that require power for movement. As seen in the case of 2-dimensional phage based micro electrodes, the area of the electrode is a design constraint on battery capacity. For devices that require power for movement, the ancillary materials in macroscopically assembled batteries, such as casing, current collectors, separator, conductive carbon, and organic binder add inert mass that then also require power for movement. Essentially the mass specific energy and power densities of complete battery systems are lowered due to the ancillary packaging components.

A materials approach that might address the issues of limiting device architecture and battery mass specific performance parameters would be the development of a 3-dimensionally structured electrode that serves both as a redox-active and mechanical support material. Such a dual functional electro-mechanical material could be used to both construct and power a device. In general such an envisioned material would have the following characteristics: a 3-dimensional porous conductive structure that provides the electrical conductivity of a current collector and the mechanical strength of metal foam; tunable porosity to accommodate electrode volumetric changes and electrolyte mass transport requirements; and a tunable framework element diameter to adjust electrical conductivity and mechanical strength.

This material could then be incorporated into a multi-layer composite battery structure as seen in Figure 1.1. This idealized structure eliminates the need for and mass of planar current collectors and the external casing is reduced to a thin polymer environmental barrier. The

battery assembly could then be laminated to the device structure in order to supplement existing device mechanical properties or reduce/eliminate device structure mass.

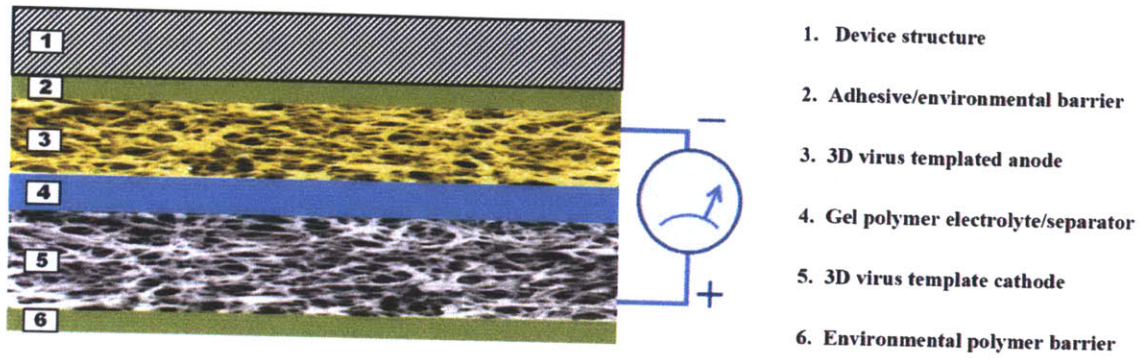

Figure 1.1. Conformal bio-templated battery composite battery. Dual functional electro-mechanical batteries are expected to provide both a power source and mechanical structure for powered devices where additional battery mass would otherwise decrease performance parameters such as maximum speed, range, and thrust-weight ratios. A composite battery is depicted laminated to the structural frame of a powered device with numbered layers identified to the right.

The concept of initially supplementing or reducing objective device mass to the eventual replacement of device structural mass with a dual functional electro-mechanical material is hypothesized with aerial drones shown in Figure 1.2. Initial material development would lead to a wing battery laminate supplementing the resident power supply. As the mechanical strength development of the battery laminate improves the airfoil structure can be reduced such that the overall mechanical properties of the composite battery/airfoil meet the initial design specifications.

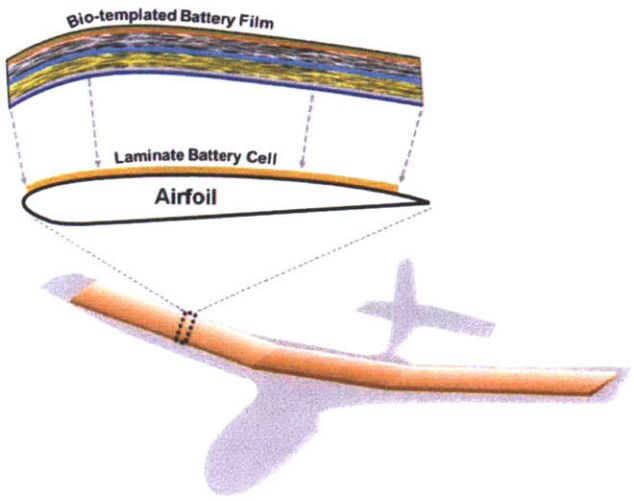

Figure 1.2. Integrated bio-templated battery composite battery. Dual functional electro-mechanical batteries are expected to provide both a power source and mechanical structure to powered devices where additional battery mass would otherwise decrease performance parameters such as maximum speed, range, and thrust-weight ratios.

The 3-dimensional dual functional material architecture can be envisioned in a broad array of other applications ranging from fuel cells to catalysis to photovoltaics. The ability to assemble porous structures on the nanoscale that provides both an electrochemical/electroactive function simultaneous with a mechanical support would be tremendously beneficial. ***This multi-functional material provides the starting hypothesis and engineering objective of this thesis work, that a 3-dimensional nanoporous material can be biotemplated in order to provide electrochemical and mechanical properties for energy storage and device applications***. The eventual scale-up of this effort is envisioned to be amenable to roll-to-roll processing as shown in Figure 1.3.

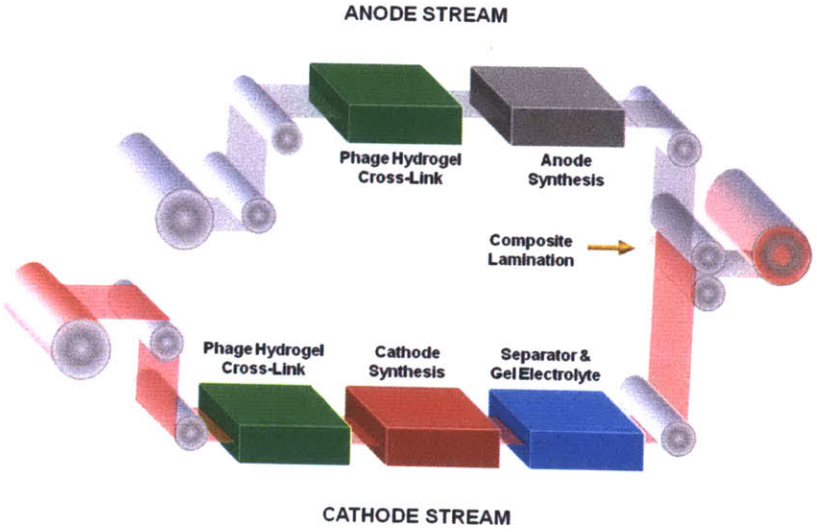

Figure 1.3. Roll-to-roll processing of multifunctional electrode materials. Separate processing streams are shown for anode and cathode materials. Both processing streams are laminated into a composite integrated battery material.

1.5 Structure of the Dissertation

The primary purpose of this work is to further expand the toolkit available to create nano-structured materials for energy and micro-device applications. This purpose is explored using the M13 bacteriophage as a biological template building block. The building blocks are assembled into 3-dimensional structures that are used as templates to synthesize inorganic current collectors and battery electrode materials. This approach establishes a synthetic route to assemble a wide array of devices for applications that include electrical energy storage, catalysis, photovoltaics, electrochromics, and more.

Chapter 2: 3-Dimensional Phage-Templated Current Collectors. This chapter describes the synthesis of stochastically assembled bacteriophage hydrogels. The hydrogels are formed using a chemical cross-linking agent to covalently cross-link the viruses into a 3-dimensional

hydrogel structure. The hydrogel then serves as a template to form inorganic copper and nickel nanowire networks that serve as 3-dimensional current collector electrodes. The electrodes are characterized morphologically with scanning and transmission electron microscopy (SEM, TEM), compositionally with energy dispersive x-ray spectroscopy and x-ray diffraction (XRD), and electrochemically with cyclic voltammetry (CV), and with four point probe for conductivity and resistivity.

Chapter 3: 3-Dimensional Phage-Templated Copper-Tin Nanowire Networks for Lithium Rechargeable Batteries. Copper 3-dimensional nano-networks are used as the electro-mechanical structure to synthesize redox active electrodes for lithium rechargeable batteries. Tin anodes are synthesized via a galvanic displacement reaction from copper nanowire networks to form a core shell structure. The inner copper core is surrounded by a layer of Cu_6Sn_5. The bronze shell is then surrounded by a layer of pure tin. Both Cu_6Sn_5 and Sn provide electroactive anode material with the large volume changes during cycling accommodated within the porous 3-dimensional scaffold.

Chapter 4: Electro-Mechanical Properties of Phage-Templated 3-Dimensional Scaffolds. The mechanical properties of the materials involved in the sysnthesis of dual functional electromechanical materials are explored using atomic force microscopy indententation and nano-indentation. The elastic moduli of phage hydrogels and aerogels, and copper and nickel nanowire networks are characterized.

Chapter 5: Future Work: Device Applications for 3-Dimensional Phage-Templated Scaffolds. Nobel metal 3-dimensional nanowire synthesis is described for possible catalytic

applications. Thermal annealing effects on copper nanowires are demonstrated. A dried phage polyelectrolyte film method is demonstrated using virus hydrogels.

1.6 References

1. Tarascon, J.M. & Armand, M. Issues and challenges facing rechargeable lithium batteries. *Nature* **414**, 359-367 (2001).
2. Pushparaj, V.L. et al. Flexible energy storage devices based on nanocomposite paper. *Proceedings of the National Academy of Sciences of the United States of America* **104**, 13574-13577 (2007).
3. Patil, A. et al. Issue and challenges facing rechargeable thin film lithium batteries. *Materials Research Bulletin* **43**, 1913-1942 (2008).
4. Cheah, S.K. et al. Self-Supported Three-Dimensional Nanoelectrodes for Microbattery Applications. *Nano Letters* **9**, 3230-3233 (2009).
5. Hart, R.W., White, H.S., Dunn, B. & Rolison, D.R. 3-D Microbatteries. *Electrochemistry Communications* **5**, 120-123 (2003).
6. Seeman, N.C. & Belcher, A.M. Emulating biology: Building nanostructures from the bottom up. *Proceedings of the National Academy of Sciences of the United States of America* **99**, 6451-6455 (2002).
7. Belcher, A.M. et al. Control of crystal phase switching and orientation by soluble mollusc-shell proteins. *Nature* **381**, 56-58 (1996).
8. Mao, C.B. et al. Virus-based toolkit for the directed synthesis of magnetic and semiconducting nanowires. *Science* **303**, 213-217 (2004).
9. Babas, C., et al. Pahge Display, A Lobaroatory Manual (Cold Spring Harbor Press, Cold Spring Harbor, NY).
10. Flynn, C.E., Lee, S.W., Peelle, B.R. & Belcher, A.M. Viruses as vehicles for growth, organization and assembly of materials. *Acta Materialia* **51**, 5867-5880 (2003).
11. Nam, K.T. et al. Virus-enabled synthesis and assembly of nanowires for lithium ion battery electrodes. *Science* **312**, 885-888 (2006).
12. Stryer, L. Biochemistry, Edn. 4th. (W.H. Freeman, New York; 1995).
13. Yoo, P.J. et al. Spontaneous assembly of viruses on multilayered polymer surfaces. *Nature Materials* **5**, 234-240 (2006).
14. Blanco, P., Kriegs, H., Lettinga, M.P., Holmqvist, P. & Wiegand, S. Thermal Diffusion of a Stiff Rod-Like Mutant Y21M fd-Virus. *Biomacromolecules* **12**, 1602-1609 (2011).
15. Whaley, S.R., English, D.S., Hu, E.L., Barbara, P.F. & Belcher, A.M. Selection of peptides with semiconductor binding specificity for directed nanocrystal assembly. *Nature* **405**, 665-668 (2000).
16. Mao, C.B. et al. Viral assembly of oriented quantum dot nanowires. *Proceedings of the National Academy of Sciences of the United States of America* **100**, 6946-6951 (2003).
17. Nam, K.T. et al. Stamped microbattery electrodes based on self-assembled M13 viruses. *Proceedings of the National Academy of Sciences of the United States of America* **105**, 17227-17231 (2008).
18. Lee, Y.J. et al. Fabricating Genetically Engineered High-Power Lithium-Ion Batteries Using Multiple Virus Genes. *Science* **324**, 1051-1055 (2009).
19. Lee, S.W., Wood, B.M. & Belcher, A.M. Chiral smectic C structures of virus-based films. *Langmuir* **19**, 1592-1598 (2003).
20. Yoo, P.J. et al. Controlling surface mobility in interdiflusing polyelectrolyte multilayers. *Acs Nano* **2**, 561-571 (2008).

21. DeLongchamp, D.M., Kastantin, M. & Hammond, P.T. High-contrast electrochromism from layer-by-layer polymer films. *Chemistry of Materials* **15**, 1575-1586 (2003).
22. Lowman, G.M., Tokuhisa, H., Lutkenhaus, J.L. & Hammond, P.T. Novel solid-state polymer electrolyte consisting of a porous layer-by-layer polyelectrolyte thin film and oligoethylene glycol. *Langmuir* **20**, 9791-9795 (2004).
23. DeLongchamp, D.M. & Hammond, P.T. Fast ion conduction in layer-by-layer polymer films. *Chemistry of Materials* **15**, 1165-1173 (2003).
24. Wang, X., Yang, X.H., Zheng, H.G., Jin, H.Y. & Zhang, Z. Synthesis and electrochemical performance of amorphous hydrated iron phosphate nanoparticles. *Journal of Crystal Growth* **274**, 214-217 (2005).
25. Arico, A.S., Bruce, P., Scrosati, B., Tarascon, J.M. & Van Schalkwijk, W. Nanostructured materials for advanced energy conversion and storage devices. *Nature Materials* **4**, 366-377 (2005).
26. Bruce, P.G., Scrosati, B. & Tarascon, J.M. Nanomaterials for rechargeable lithium batteries. *Angewandte Chemie-International Edition* **47**, 2930-2946 (2008).
27. Mui, S.C. et al. Microstructure effects on the electrochemical kinetics of vanadium pentoxide thin-film cathodes. *Journal of the Electrochemical Society* **153**, A1372-A1377 (2006).

CHAPTER 2

3-Dimensional Phage-Templated Current Collectors

2.1 Introduction

Numerous energy related fields have developed nanostrucutured materials to improve objective device performance. Photovoltaics, fuel cells, electro-optical, and lithium rechargeable batteries are just a few.[1-4] There have been numerous efforts to create 3-dimensional porous nano-architectures to improve the performance of these devices.[5-10] While many interesting structures have been synthesized, scale-up of the materials would be prohibitively expensive in some cases. Further, assembling nanomaterials into practical devices can pose challenges in terms of packaging and integration. For some applications such as lithium rechargeable batteries, the nano-structured materials require additional conductive additives and organic binders.

For electrical storage applications in particular, there is a constantly increasing demand for lightweight power sources and electrode architectures that eliminate the need for conductive and organic additives. The elimination of ancillary electrode mass will increase specific energy and power densities. The increased demand for lightweight power is coupled with increasing device miniaturization. As the scale of devices decreases, current energy supply and storage technologies add mass on the same scale as the device itself. Given these challenges and demands, a dual functional electro-mechanical material that serves as both a device structural material and a power source would dramatically improve device integration and range for powered movement.

For such an electro-mechanical material, an idealized material might begin with an orthogonal 3-dimensional matrix as shown in Figure 2.1. The idealized architecture would possess a number of desirable design features. These include the ability to adjust the basic structural element diameter, porosity, and overall structural thickness. Further optimization

might also include a hierarchical material porosity to optimize the transport properties of material through the scaffold. Finally, the scaffold would function as a free standing film increasing device integration options.

To address the demand for lightweight power with a long-term objective of a dual functional electro-mechanical material, bio-templating offers the means to create novel 3-dimensional nano-architectures. In particular, the M13 virus has proven a versatile biotemplate for a wide range of metal, metal oxide, and semiconducting materials.[11-14] The virus has also served as a structural unit to assemble fibers and liquid crystal films.[15, 16] If the requirement for an orthogonal orientation of structural elements is relaxed in Figure 2.1, then one might envision a stochastically assembled matrix with mean distribution values of element diameter, porosity and scaffold thickness. Such a stochastic assembly approach using the M13 virus as the basic structural element is envisioned in Figure 2.2. The general approach would be to assemble the virus into a 3-dimensional biotemplate, mineralize the template to a 3-dimensional conductive scaffold, and then further functionalize the conductive scaffold for a particular application.

In this work, the M13 is assembled into a 3-dimensional biotemplate using glutaraldehyde to covalently cross-link virus particles into hydrogels. The resulting hydrogels are mineralized to conductive copper and nickel nanowire scaffolds using electroless deposition. Control of nanowire diameter, scaffold porosity, and film thickness is demonstrated. The nanowire scaffolds are also found to be highly conductive and can be synthesized as free-standing films. These novel 3-dimensional nanowire networks are envisioned to serve as a tunable, scalable and general design architecture across the many material applications for nano-porous materials.

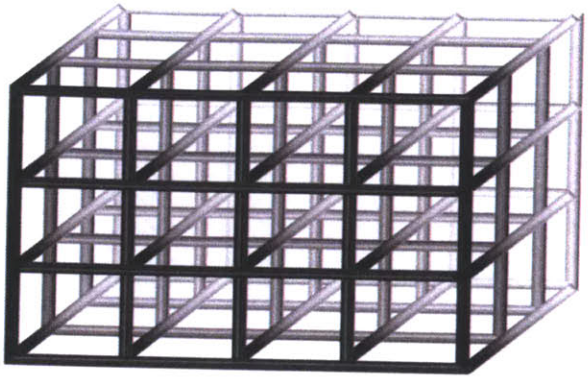

Figure 2.1. Idealized 3-dimensional lattice. An idealized 3-dimensional lattice is shown as a conceptual start point for developing bacteriophage 3-dimensional architectures. The ideal structure has tunable element diameters, porosity, and thickness.

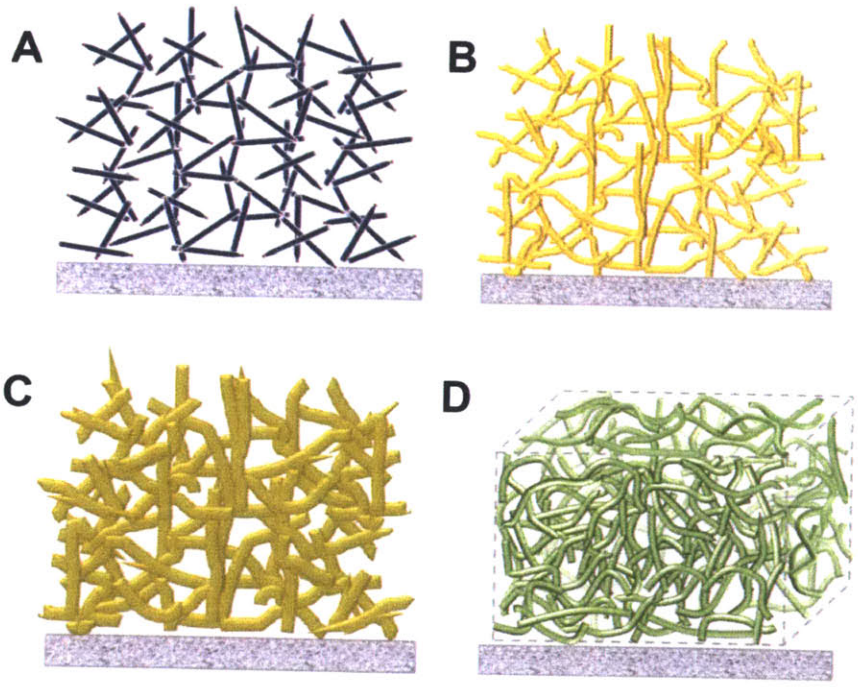

Figure 2.2. Stochastic virus assembly into 3-dimensional architecture. A) The idealized 3-dimensional lattice structure in Figure 2.1 is relaxed to accommodate the non-orthogonal element orientations of a virus solution. The virus solution is cross-linked into a stochastically ordered hydrogel. B) The virus hydrogel is mineralized into a 3-dimensional conductive meteal nanowire scaffold. C) The metal nanowire scaffold is functionalized to the desired active material. D) Representative 3-dimensional virus-based volume element.

2.2 Experimental

M13 Phage. The M13 bacteriophage E3 and Y21M clones were amplified using the ER2738 *E.coli* strain and purified using standard polyethylene glycol (PEG) precipitation protocols. Collected phage stocks were stored in 1 x phosphate buffered saline (1xPBS). Phage were quantified using a Nanodrop 1000 UV/VIS spectrophotometer. The Nanodrop nucleic acids function was used to determine absorbance at 269nm and 320nm. Absorbance values were used in the equation below to determine phage concentration in virions per milliliter (virions/ml). The numerator includes the difference between the peak DNA absorbance at 269nm and the absorbance of aromatic protein residues at 320nm multiplied by the extinction coefficient of $6x10^{16}$. The denominator is the number of base pairs in the E3 clone.

$$[\text{phage}] = \frac{(A_{269}-A_{320})\cdot 6x10^{16}}{7220}$$

The pVIII coat protein on E3 and Y21M are identical. The E3 clone has an EEED protein fusion sequence on the N-terminus of pVIII. Note that there are four carboxylic acid functional groups at the p8 N-terminus with three glutamates and one aspartate. The E3 clone derived from the E4 clone with an EEEE protein fusion, where a mutation resulted in a change from a glutamate to an aspartate residue. The Y21M clone substitutes methionine for tyrosine at the 21st amino acid residue on the pVIII coat protein.[17] The amino acid residue substitution is on the interior of the phage capsid and increases its persistence length,[18] but does not alter the binding properties of exterior coat protein.

Hydrogel Formation. Stock 50% Glutaraldehyde Solution (Sigma Aldrich, CAS# 111-30-8) was placed in a reservoir. The specific gravity of the glutaraldehyde solution is 1.106. Virus

solutions (either E3 or Y21M) in 1xPBS were pipetted onto a substrate. The loading factor for test samples was 10μl on an approximately $1cm^2$ substrate. Substrates tested included untreated silicon wafers, indium tin oxide (ITO), copper foil, aluminum foil, glass, fluorine-doped tin oxide (FTO), and steel. Substrates with phage solution were inverted and placed onto the glutaraldehyde solution surface. Mechanical support was used for substrates that did not remain on the top of the glutaraldehyde solution. The phage solution was allowed to remain in contact with the glutaraldehyde solution 30min. Cross-linked phage solutions were removed from the glutaraldehyde solution and transferred to 1L 1xPBS for 12-24h to remove excess glutaraldehyde from the resulting hydrogel.

An alternative method was used to form thicker hydrogels by creating well assemblies. A well reservoir was assembled from 4mm or 8mm holes punched in 1mm, 2mm, or 3mm thick rubber. The resulting rubber masks were heat molded onto glass, ITO coated polyethylene terephthalate (PET), or silicon wafer substrates via 100μm thick heat moldable Solaronix Meltonix 1170-100 films. The substrate/heat moldable film/rubber mask were placed on a heat plate at 120°C and held in placed with a Teflon block for one minute. The resulting wells can be filled with varying volumes of phage solution and inverted and placed in contact with a 50% stock glutaraldehyde solution. Mechanical support for the well assemblies was required to maintain the phage-glutaraldehyde liquid-liquid interface at the surface of the glutaraldehyde. Phage solution contact with glutaraldehyde proceeded for 2h for well assemblies. Wells with the resulting hydrogels were placed in 1xPBS for 24h to remove excess glutaraldehyde. The resulting hydrogels maintained the dimensions of the original well assembly. Figure 2.3 depicts predicted hydrogel thickness as a function of initial phage volumes for 4mm and 8mm well assemblies up to a thickness of 3mm.

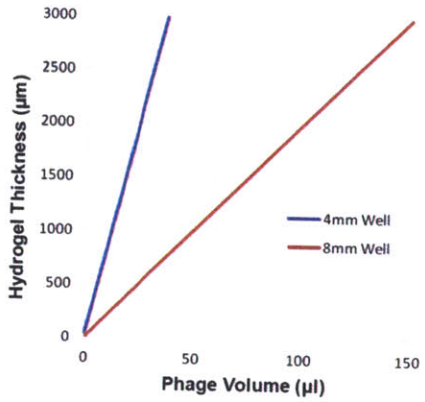

Figure 2.3. Hydrogel formation using well assemblies. Predicted hydrogel thickness is plotted as a function of initial phage volume for 4mm and 8mm circular well assemblies.

Palladium Sensitization. Virus hydrogels were sensitized with palladium solutions to effect electrostatic binding of palladium ion complexes with virus coat proteins. Two different palladium salts were used to prepare sensitizing solutions. Sodium tetrachloropalladate (II) trihydrate (Strem, CAS# 13820-53-6) was prepared at a concentration of 10mM with an assumed predominant ionic palladium species of $[PdCl_4]^-$. Tetraaminepalladium (II) chloride monohydrate (Sigma Aldrich, CAS# 13933-31-8) was prepared at a concentration of 10mM with an assumed predominant ionic palladium species of $[Pd(NH_3)_4]^{2+}$.

Copper Electroless Deposition. Copper electroless deposition solution consisted of: 0.032M $CuSO_4 \cdot 5H_2O$ (Mallinckrodt Chemicals, CAS# 4844-02); 0.040M ethylenediamino tetraacetic acid, disodium, dehydrate (EDTA) (Mallinckrodt Chemicals, CAS# 6381-92-6); 0.1M 3-(N-morpholino) propanesulfonic acid (MOPS) (Sigma Life Science, CAS# 1132-61-2); 0.067M dimethyl amine borane (DMAB) (Aldrich, CAS# 74-94-2). The final ELD solution pH was adjusted to 7.

Nickel Electroless Deposition. Nickel chloride electroless deposition solution consisted of 0.1M $NiCl_2$ (Sigma, CAS # 339350), 0.15M $Na_2B_4O_7$ (Sigma, CAS # 1330-43-4), 0.25M glycine (Sigma, CAS # 56-40-6), and 0.5M dimethyl amine borane (DMAB) (Aldrich, CAS# 74-94-2). Nickel sulfate electroless deposition solution consisted of: 0.032M $NiSO_4 \cdot 6H_2O$ (Aldrich, CAS# 10101-97-0); 0.064M lactic acid; 0.1M 3-(N-morpholino) propanesulfonic acid (MOPS) (Sigma Life Science, CAS# 1132-61-2); 0.067M dimethyl amine borane (DMAB) (Aldrich, CAS# 74-94-2). The final ELD solution pH was adjusted to 7.

Scanning Electron Microscope/Focused Ion Beam. A FEI Company Helios 600i Nanolab Dual Beam SEM/FIB was used for high resolution imaging and for cross-sectional etching samples. The FEI XL-30 ESEM (Environmental Scanning Electron Microscope) was used for general purpose imaging.

Energy Dispersive X-Ray Spectroscopy. EDS was performed using the FEI Company Helios 600i Nanolab Dual Beam SEM/FIB. Samples were placed at a working distance of 10.5mm and a an accelerating voltage of 10kV was used. Spectra were collected and initially analyzed for peak identification and mass composition using INCA software. Spectra files were then exported as text files and plotted using Microsoft Excel.

X-Ray Diffractometry. X-ray diffraction (XRD) analysis was conducted on a PANalytical X'Pert Pro X-ray diffractometer with Cu K_α radiation (λ =1.54060Å), a 2Theta-Omega scan axis, and a scan step size of 80.0100s. A 1° offset was used for copper and nickel film samples on

single crystalline silicon wafers to minimize silicon (100) peaks. Sample irradiation lengths varied between 0.4 and 0.6cm.

Profilometry. A Veeco DEKTAK 150 Profilometer was used to determine sample thicknesses. A razor blade was used to cut a "Z" at multiple locations along a profile path to assist in leveling the profile during analysis. A step height calibrated 2.5μm stylus was drawn over the sample with a 2.0-3.0mg force setting at an approximately 200μm/s scan rate. Average step heights were determined by calculating the difference between average profile height values of the substrate and top of the film surface. Surface roughness, R_q, values were determined over length scales of greater than 1000μm.

Four-Point Probe Conductivity. A Keithley 4200-SCS Semiconductor Characterization System was used as a four-point probe to determine resistivity and conductivity of film samples in conjunction with film thicknesses determined from profilometery. The probe head consisted of four tungsten carbide probes 62.5mil (1.5875mm) apart for a total width of 4.7625mm between the outer probes. Current, I, sweeps of 0.1-100mV with 20 steps were sourced between the outer probes. The voltage difference, V_{diff}, was measured between the high impedance middle probes. Resistance was calculated as $R = V_{diff} / I$. Resistance was verified to obey a linear, ohmic relationship. Sheet resistance was calculated as $R_{sq} = 4.53 \cdot R$. Using film thickness, t, determined with profilometry, film sample resistivity, ρ, was calculated as:

$$\rho = \frac{\pi}{\ln 2} \frac{V_{diff}}{I} \cdot t$$

Mercury Porosimetry. The Micromeritics Autopore IV mercury porosimeter was used to determine the pore size distribution of copper and nickel films. Film samples were delaminated from substrates with a razor blade and transferred to the sample chamber. Sample masses greater than 10mg were used, requiring multiple films synthesized under the same reaction conditions. A low pressure profile up to 14psi and high pressure profile up to 10,000psi were used. Using the Autopore IV analysis software, Differential Intrusion vs Pore Size output was used to determine the pore size distribution.

Image Analysis. ImageJ[19] 1.45p software (U. S. National Institutes of Health) was used for pore size analysis of scanning electron microscope focused ion beam cross-section images. SEM images were first optimized for maximum brightness/contrast and then converted to a binary black and white image, segmenting the image into pores and solids. Based on the image contrast of SEM images, void spaces are darker than the nanowires which scatter electrons. Thus, void spaces are converted to black particles during the binary image conversion. Set scale was used to calibrate the image scale to the software scale. The Analyze particles function was used to determine the area fraction, perimeter. The "include holes" option was left unchecked to ensure that nanowire area was not included in the pore space area fraction. A 102 pixel size was used as a particle size cut-off to eliminate noise of non-physical pores. The area fraction value was used as the cross-section porosity. The feret diameter statistic was used as an estimate of pore diameter. Total contour length of pores in the 2-dimensional cross-section was determined by selecting all particles and using the Measure/Perimeter function.

2.3 Results and Discussion

2.3.1. Hydrogel Formation.

To synthesize 3-dimensional metal nanowire scaffolds, the starting hypothesis was that the M13 virus could be cross-linked into a hydrogel and serve as 3-dimensional bio-template. Glutaraldehyde is a commonly used molecule to cross-link proteins. Previous work using the M13 virus to assemble fibers employed glutaraldehyde as the cross-linking agent.[15, 20, 21] Glutaradlehyde is a bifunctional aldehyde on a five carbon chain. The aldehyde functional groups are thought to react reversibly predominantly with lysine amino acids above a pH of 3.[22] The glutaraldehyde-protein reaction is observed to be generally irreversible between pH 7-9. The bifunctional character of the glutaraldehyde molecule facilitates the linkage between two virus particles. Figure 2.4 (A) indicates the exposed lysine residues on a Van der Waals surface image of the bacteriophage. The image was rendered with Protein Database file 2C0X using Jmol software.[23] While the previous work with virus fibers generally involved concentrated virus solutions above $1x10^{16}$pfu/ml, we believed that using lower phage concentrations with glutaraldehyde might result in the formation of hydrogels.[15] A hydrogel with close to 99% percent water might offer a sufficient diffusive pathway for metallization precursors to access the extent of the 3-dimensional bio-template.

A variety of methods were attempted to cross-link virus solutions into hydrogels. These methods include direct mixing of dilute glutaraldehyde with virus solutions across a range of stoichiometric ratios of glutaraldhyde to p8 proteins, virus concentrations, cross-link times, and pH values. One method involved dropcasting a virus solution onto an untreated silicon wafer substrate and placing a dialysis membrane over the top of the phage solution, and then placing glutaraldehyde on top of the membrane. This resulted in hydrogel films that adhered to the

substrate. The top surface of gels prepared with this technique were macroscopically rough. Two reasons were believed to contribute to the gel surface roughness. The first was the possible gel formation within the pores of the dialysis membrane that could cause gel shearing upon removal of the membrane. The second reason was the observation that glutaraldehyde sediments through the membrane pores into the nascent gel. The specific gravity of the 50% glutaraldehyde solutions used is 1.106 which is higher than that of water.

To take advantage of the difference in specific gravities and achieve phage hydrogels with a low roughness top surface, the cross-linking scheme in Figure 2.4 (B) was used. The method described above employing a dialysis membrane is spatially inverted and eliminates the use of a membrane. The phage solution is dropcast onto a substrate, inverted and then placed in contact with a reservoir of 50% glutaraldehyde solution creating a one-dimensional diffusion profile of glutaraldehyde into the phage solution. The virus solution and glutaraldehyde are observed to form distinct liquid-liquid interface owing to the difference in specific gravities. Virus suspensions were prepared in phosphate buffered saline (PBS) solution at pH 7.4. Stock 50% glutaraldehhyde is stored at pH 3. The PBS is believed to buffer the glutaraldhyde diffusing into the virus solution. In addition to dropcasting the virus on a substrate to develop a hydrogel film, it was observed that virus solutions cross-link into the geometry of the solution. As an example, a microfuge tube filled with 0.5ml of glutaraldehyde solution and 100µl of E3 virus at concentration of $1x10^{14}$pfu/ml results in a hydrogel "plug" shown in Figure 2.5 (A). Similarly, 8mm diameter wells were created using 1mm thick rubber adhered to silicon substrates. The rubber wells were filled with virus solution, inverted, and cross-linked on glutaraldehyde. An example of the hydrogel film is shown in Figure 2.5 (B). This technique allows for control over the hydrogel thickness by controlling the geometry of the virus solution

during cross-linking. Using 4mm and 8mm diameter wells with varying thickness, gels of varying thickness were assembled using the linear correlation of thickness to phage volume divided by surface area shown in Figure 2.3 in Section 2.2. Minimal volume changes were observed during 30 minutes of cross-linking time for film gels and up to 2 hours of cross-linking for "plug" gels. Gels were rinsed in phosphate buffer for 24 hours to remove any excess glutaraldehyde.

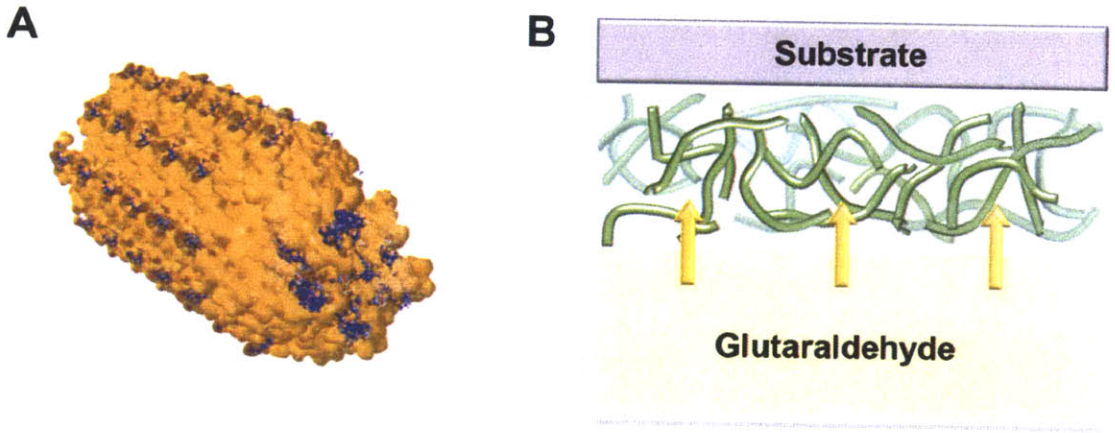

Figure 2.4. Phage cross-linking concept. A) Van der Walls surface image of the M13 virus displaying solvent exposed lysine residues in blue. Image perspective is looking down the axis at an oblique angle from the p3 end of the virus. Image was rendered from PDB file 2C0X using Jmol software. B) Virus solutions in phosphate buffered saline have a specific gravity less than 50% glutaraldehyde creating a liquid-liquid interface. Glutaraldehyde diffuses into the virus solution cross-linking virus particles into a covalently linked hydrogel. Virus hydrogels were found to adhere to silicon, glass, copper, aluminum, indium tin oxide and fluorine-doped tin oxide substrates.

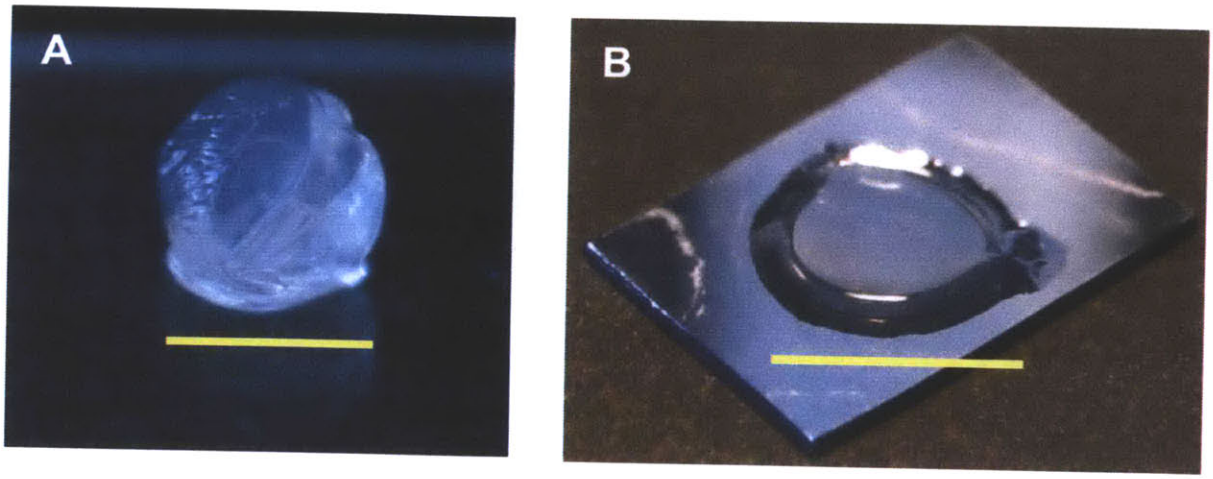

Figure 2.5. M13 virus hydrogels. Hydrogels were formed using the cross-linking concept shown in Figure 2.4. The E3 clone at a concentration of $1x10^{14}$pfu/ml was used to form the gels in A and B. Hydrogels cross-link to the volume dimensions of the cross linked solution. A) Hydrogel formed within a microfuge tube. B) Hydrogel formed within a 1mm deep well. Scale bars are A) 5mm and B) 8mm.

2.3.2. Copper Electroless Deposition.

In order to use the hydrogels to mineralize copper and nickel nannowires from electroless deposition (ELD) solutions, the virus particles need to be sensitized with a catalyst to mediate the reduction of cation precursors that are otherwise stable in the presence of reducing agent within the ELD. Palladium salt solutions are commonly used to sensitize substrates both in commercial plating applications, as well as previously demonstrated copper biotemplating. [24-28] Palladium (II) chloride (Na_2PdCl_4) has been extensively used for bio-templating applications.[25, 29-31] The dominant ionic species of Na_2PdCl_4 in solution is $[PdCl_3(H_20)]^-$ and some groups have hypothesized that negative ions bind to amine groups on biotemplates.[32, 33] Given that the likely mechanism of glutaraldehyde cross-linking creates a covalent bond with lysine residues, a $(NH_3)_4PdCl_2$ palladium solution was used to sensitize the virus hydrogels. The predominant ionic species in solution is expected to be the $[(NH_3)_4Pd]^{2+}$ complex.[34] With four carboxylate

amino acids at the N-terminus of the p8 protein, at neutral pH values, the positively charged palladium complex will electrostatically bind the virus. Virus hydrogels were exposed to 10mM $(NH_3)_4PdCl_2$ for at least 6 hours to allow for diffusion and binding. To prevent solid product precipitation between palladium and phosphate, a buffer exchange from PBS to MOPS at pH 7 was conducted. After palladium exposure, the gels were rinsed in MOPS buffer for at least 12 hours to remove excess catalytic ions.

The palladium sensitized gels were then immersed in a copper electroless deposition solution. In general, electroless deposition solutions consist of a precursor metal ion to be reduced, a reducing agent, a complexing agent to stabilize the metal ion in the presence of the reducing agent, and a buffer to prevent pH variation and ensure that the desired product is plated.[35] Copper electroless deposition was traditionally conducted at high pH values until the development of low pH formulations that were later modified for use with biotemplating systems.[25,28] The copper electroless deposition used in this work was modified from the formulation used by Balci, et al to synthesize copper nanoparticles within the core of the tobacco mosaic virus.[25] The copper electroless deposition solution precursor ion, complexant, reducing agent, and buffer consisted of 0.032M $CuSO_4 \cdot 5H_2O$, 0.040M ethylenediaminetetraacetic acid, disodium, dehydrate (EDTA), 0.1M 3-(N-morpholino) propanesulfonic acid (MOPS buffer), and 0.067M dimethyl amine borane (DMAB). The overall scheme for copper and nickel nanowire syntheses is shown in Figure 2.6 and consists of 1) hydrogel formation, 2) palladium sensitization, and 3) nanowire synthesis in an electroless deposition bath.

Figure 2.7 shows the results of the electroless deposition of copper onto virus hydrogels at multiple length scales. A contiguous network of copper nanowires is seen at each length scale. Figure 2.7 (A) reveals a rough surface morphology on the nanowires and shows the junction

nodes between nanowire elements. Energy dispersive X-ray analysis in Figure 2.9 indicates high purity nanowires with a copper composition consistently above 99%. XRD analysis in Figure 2.10 confirms the copper composition and reveals a minor copper oxide peak. Figure 2.8 is a photo image demonstrating a free standing 3-dimensional nanowire network film. The dimensions of the film are approximately 6mm x 4mm. The free standing films also presented the flexibility to bend, although characterizing the flexural modulus of the material was not part of this initial work.

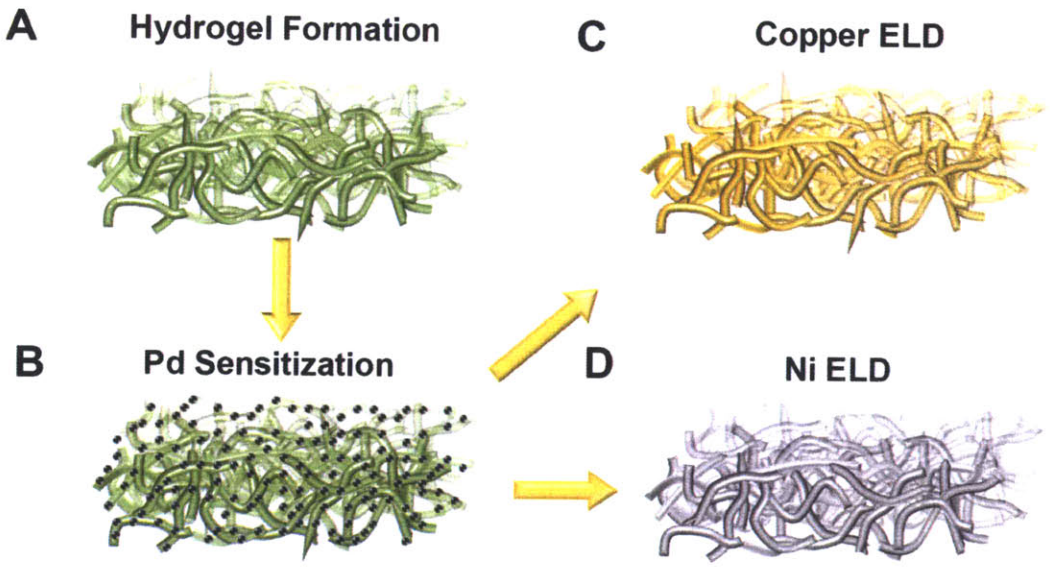

Figure 2.6. 3-dimensional metal scaffold synthesis sequence. A) Hydrogel formation. B) Hydrogel sensitization with palladium ions. C) Immersion of palladium sensitized hydrogel into a copper electroless deposition solution yields a 3-dimensional copper nanowire scaffold. D) Immersion of palladium sensitized hydrogel into a nickel electroless deposition solution yields a 3-dimensional copper nanowire scaffold.

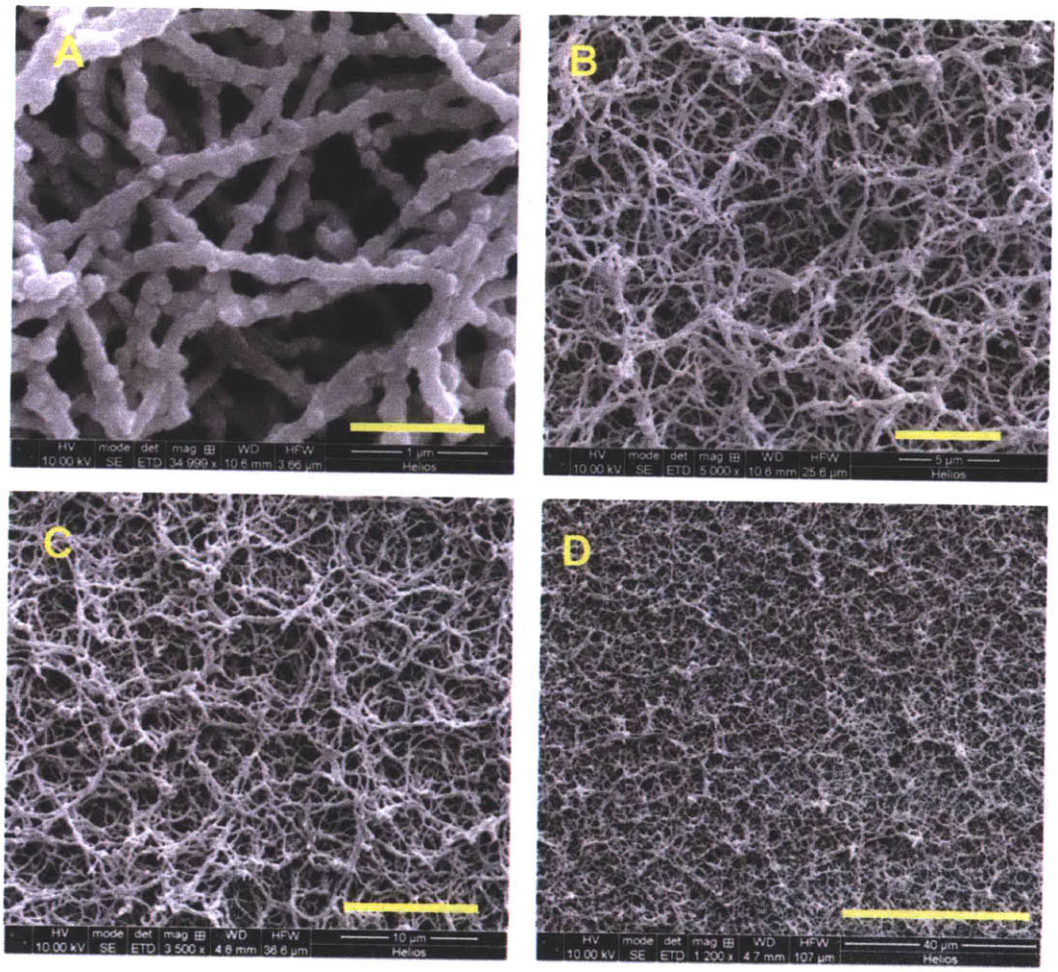

Figure 2.7. Copper nano-networks at multiple length scales. 3-dimensional copper nanowire nanonetworks templated on E3 hydrogels formed from a concentration of $7x10^{13}$pfu/ml. Scale bars are A) 1μm, B) 5μm, C) 10μm, and D) 40μm.

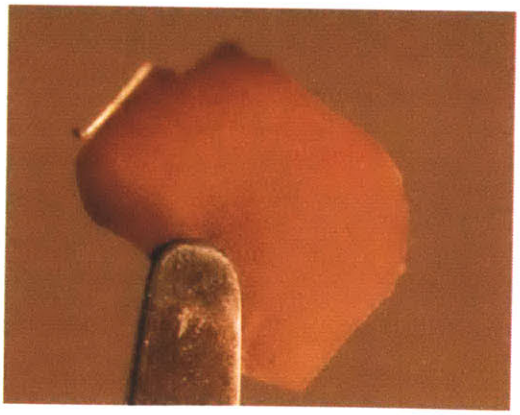

Figure 2.8. Free standing copper nanowire film. Dimensions of the film are approximately 6mm x 4mm.

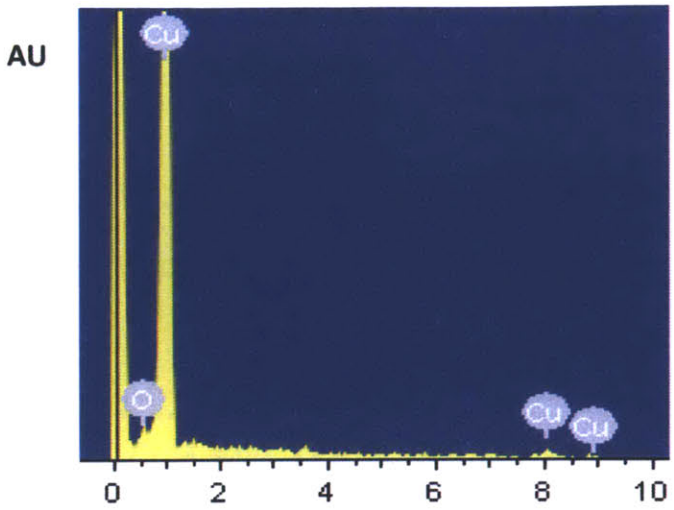

Figure 2.9. Energy dispersive X-ray spectrum for copper nanowire scaffolds. Quantification of the EDS spectrum indicates a Cu:O mass ratio of 99.13:0.87.

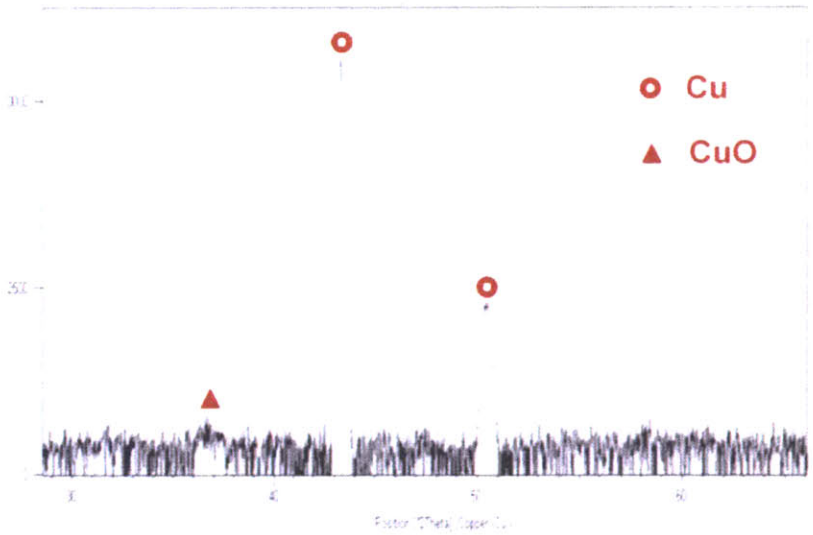

Figure 2.10. X-ray diffractometry spectrum for copper nanowire scaffolds. Copper peaks fit to Cu Powder Diffraction File Reference Number 04-003-1261. CuO peak fit to Reference Number 01-078-0428.

2.3.3. Nickel Electroless Deposition.

After palladium sensitization, virus hydrogels were also immersed in nickel electroless deposition solutions to synthesize 3-dimensional nickel nanowire networks. Developing an electroless deposition solution composition amenable to the virus hydrogels proved challenging. A nickel electroless deposition solution previously used with the tobacco mosaic virus was employed.[26] This bath composition consisted of 0.1M $NiCl_2 \cdot 6H_2O$ as the metal precursor, 0.15M $Na_2B_4O_7$ as the buffer, 0.25M glycine as the metal ion complexant, and 0.5M dimethyl amine borane as the reducing agent. The rapid kinetics of the bath composition caused vigorous bubbling of hydrogen gas throughout the hydrogels and caused film delamination from the silicon substrate and macroscopic holes in the resulting film. Another challenge was observed in SEM images of the resulting nanowires. As seen in Figure 2.11 (A), there were numerous locations where the nanowires appeared to fracture. One hypothesis was that the nickel chloride formulation was the cause of the phenomenon. Nickel chloride deposition baths are known to create deposits with high internal stresses.[36] The reaction times were less than five minutes and if allowed to progress beyond that time point, the top surface of the hydrogel would eventually develop into a solid nickel sheet as seen in the SEM image in Figure 2.11 (C). The other consequence of the short time scale of this ELD composition is the variable nanowire diameter. As seen in Figure 2.11 (C), from the nickel sheet at the top surface, the nanowires decrease in diameter toward the bottom of the film. For the narrow set of conditions of dilute phage concentrations, thin hydrogels, and a 90 second exposure to the nickel chloride solution, well formed nanowires resulted as seen in Figure 2.11 (D). The following list summarizes the results for a wide range of nickel chloride ELD concentrations and phage concentrations tested.

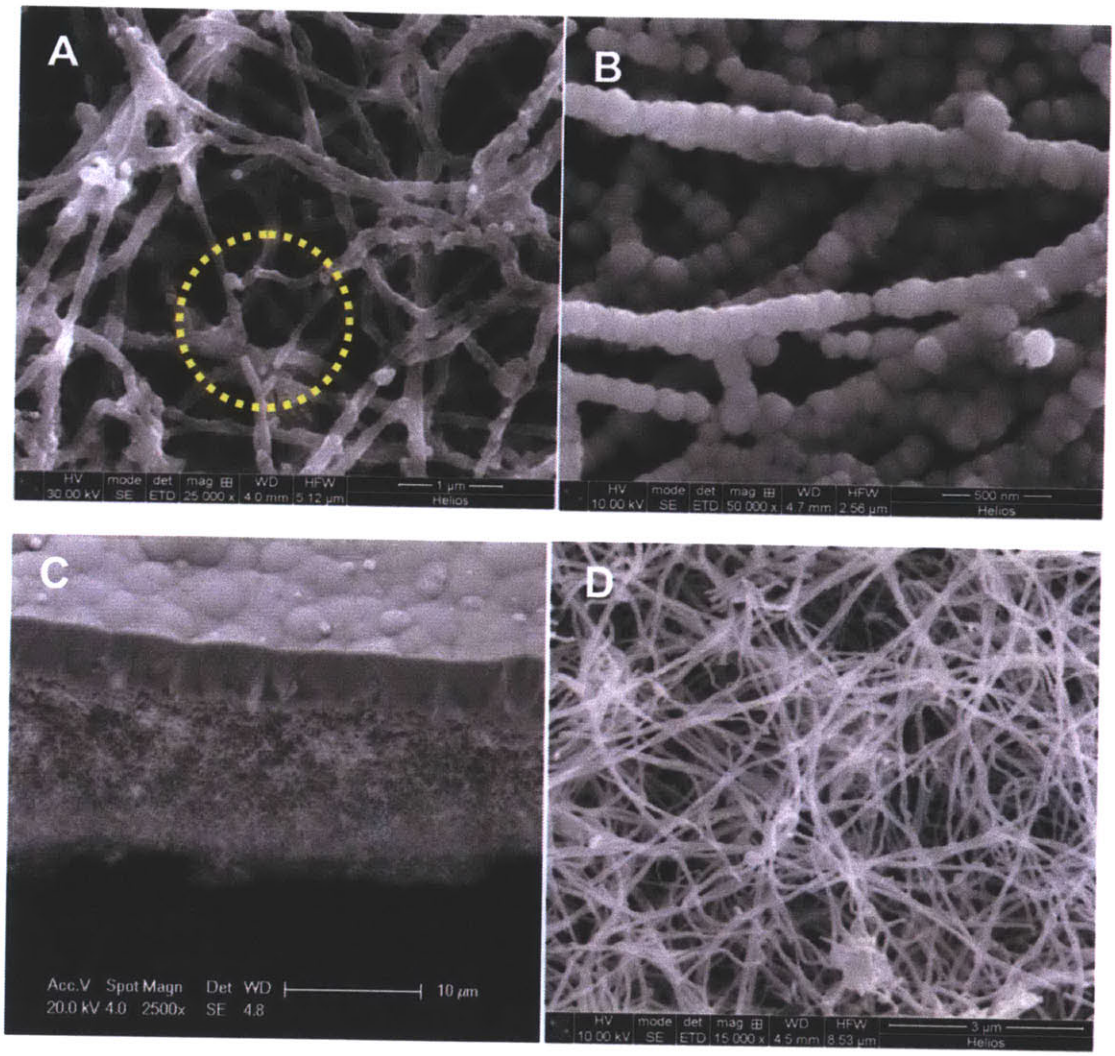

Figure 2.11. Nickel nanowire synthesis challenges. A) Nanowire separation shown in the dashed yellow circle. B) Beaded nanowire morphology resulting from slow electroless deposition kinetics. Nanospherical particles are believed to result from surface energy minimization. C) A nickel nanowire scaffold with rapid kinetics. The top surface of the scaffold is sheeted over blocking further transport of reactants in to the film. Variable nanowire diameters are seen, with diameters decreasing into the depth of the film. D) Nickel nanowires reduced on the Y21M clone for 90s in a nickel chloride deposition solution.

Reduction too fast	→	**top surface sheets**
Gel too dense	→	**top surface sheets; requires slow kinetics**
Reduction too slow	→	**Ostwald ripening**
Gel too porous	→	**poor substrate adhesion**

An example of a slow nickel nanowire reduction with a 3mM nickel sulfate ELD spanning 10 hours is shown in Figure 2.11 (B). The beaded nanowire morphology likely results from an Ostwald ripening like process, minimizing the surface energy of nanoparticles through coalescence of small nanoparticles into larger ones as they develop.[37]

In order to avoid the consequences of high tension nanowires and rapid reduction kinetics, a nickel deposition bath was developed using nickel sulfate and lower reactant concentrations. The nickel sulfate bath consisted of 0.032M $NiSO_4 \cdot 6H_2O$, 0.064M lactic acid, 0.1M 3-(N-morpholino) propanesulfonic acid (MOPS buffer), and 0.067M dimethyl amine borane (DMAB). The bath pH was adjusted to pH 7 and reduction times ranging from 10-120 minutes were tested. Hydrogels with both the E3 and Y21M clones were mineralized. The nickel nanowire scaffold shown in Figure 2.12 was synthesized from an E3 gel with a phage concentration of $7x10^{13}$pfu/ml and immersed in the nickel sulfate reduction bath for 90 minutes. The nickel sulfate bath was found to avoid many of the synthesis problems encountered with the nickel chloride bath. EDS compositional analyses consistently resulted in nickel purity over 98% with a small percentage of oxide as seen in Figure 2.13. The XRD spectrum in Figure 2.14 shows the two primary nickel peaks. No nickel oxide was detected in any nickel nanowire XRD scan.

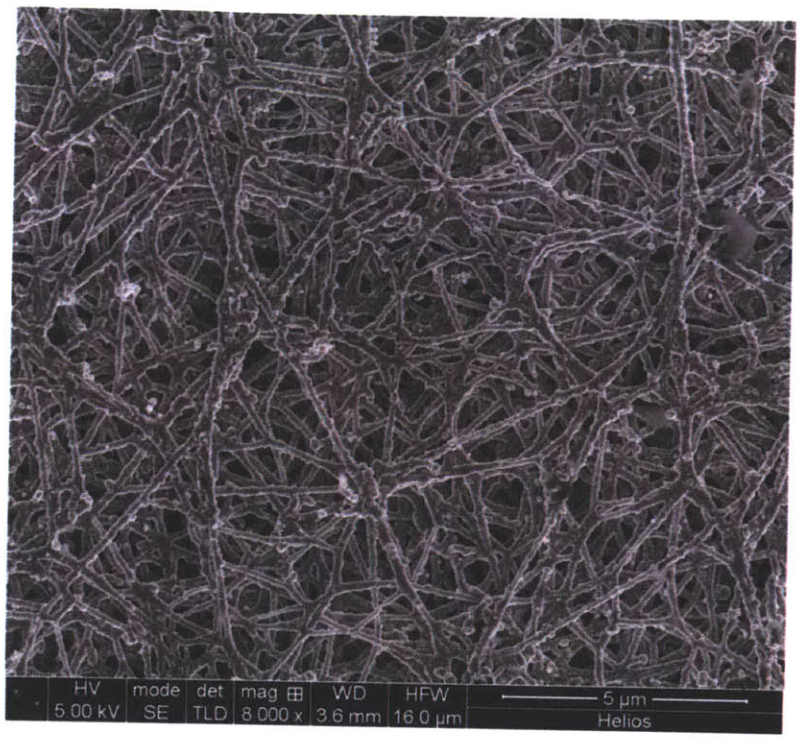

Figure 2.12. Nickel nanowire 3-dimensional scaffold. Nickel nanowires synthesized on an E3 gel with a phage concentration of $7x10^{13}$pfu/ml and immersed in the nickel sulfate reduction bath for 90 minutes.

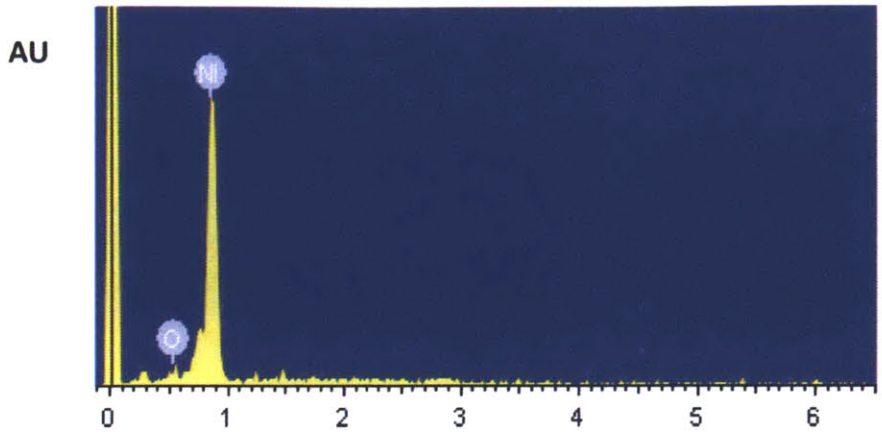

Figure 2.13. Energy dispersive X-ray spectrum for nickel nanowire scaffolds. Quantification of the EDS spectrum indicates a Ni:O mass ratio of 98.66:1.34.

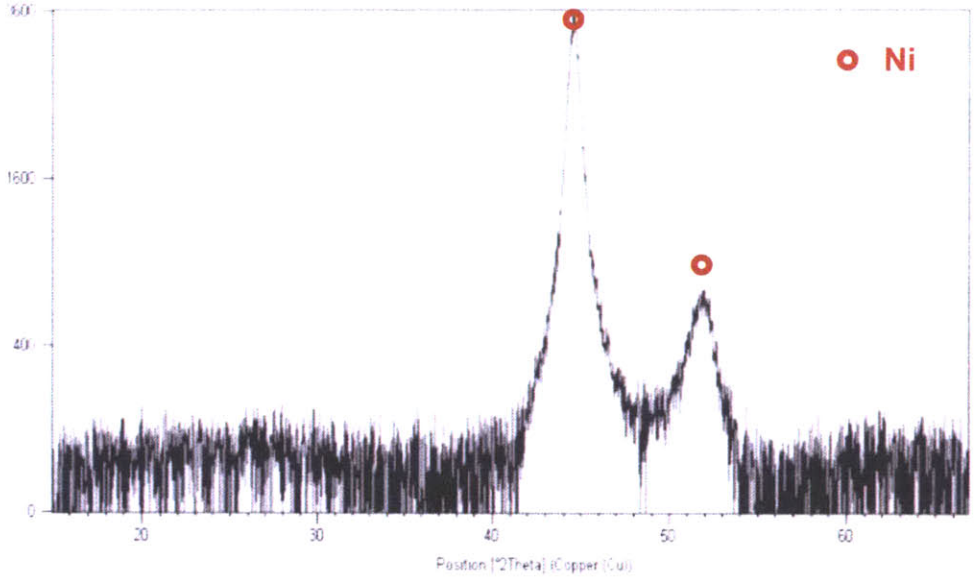

Figure 2.14. X-ray diffractometry spectrum for nickel nanowire scaffolds. Nickel peaks fit to Ni Powder Diffraction File Reference Number 04-002-1862.

2.3.4 Nanowire Diameter Control.

Once the copper and nickel electroless deposition solutions were determined, control over nanowire diameter was tested by varying the exposure time of the palladium sensitized hydrogels to the respective ELD solutions. As seen in Figure 2.15, copper nanowire reduction times of 5min, 20min, 45min, 1h, 2h, 6h, and 14h were conducted and imaged with SEM. Nanowires at early time points display a beaded appearance with discontinuous nanoparticles. The nanoparticles appear to grow in size beyond 45min. After 2h of reduction time contiguous nanowires appear and increase in diameter through 14h.

Using the nickel sulfate deposition bath, nanowire reduction times of 30min, 45min, 60min and 90min were performed and imaged with SEM as seen in Figure 2.16. Although the overall time course for nickel nanowire synthesis is more rapid than for copper, a similar morphological evolution of nanowires is observed. Small nanoparticles appear to coalesce into larger particles until 60min at which point contiguous nanowires appear and continue to increase in diameter through 120min. Also shown in Figure 2.16 is a nickel nanowire cross-section that reveals a 9nm hole in the center providing evidence of the phage bio-template on which the nanowire was grown.

To develop a nanowire growth curve, SEM images were analyzed to record to the average nanowire diameter at each time point for both the copper and nickel images. Thirty measurements were recorded for each image and 2 to 3 images were used for each time point. The average nanowire diameter and standard deviation as a function of copper and nickel ELD reduction time is plotted on Figure 2.17 and Figure 2.18 respectively. Both growth curves are seen to observe a power law relationship during the initial growth phase and then increase linearly. For copper nanowire growth this transition occurs graphically at 2 hours. This

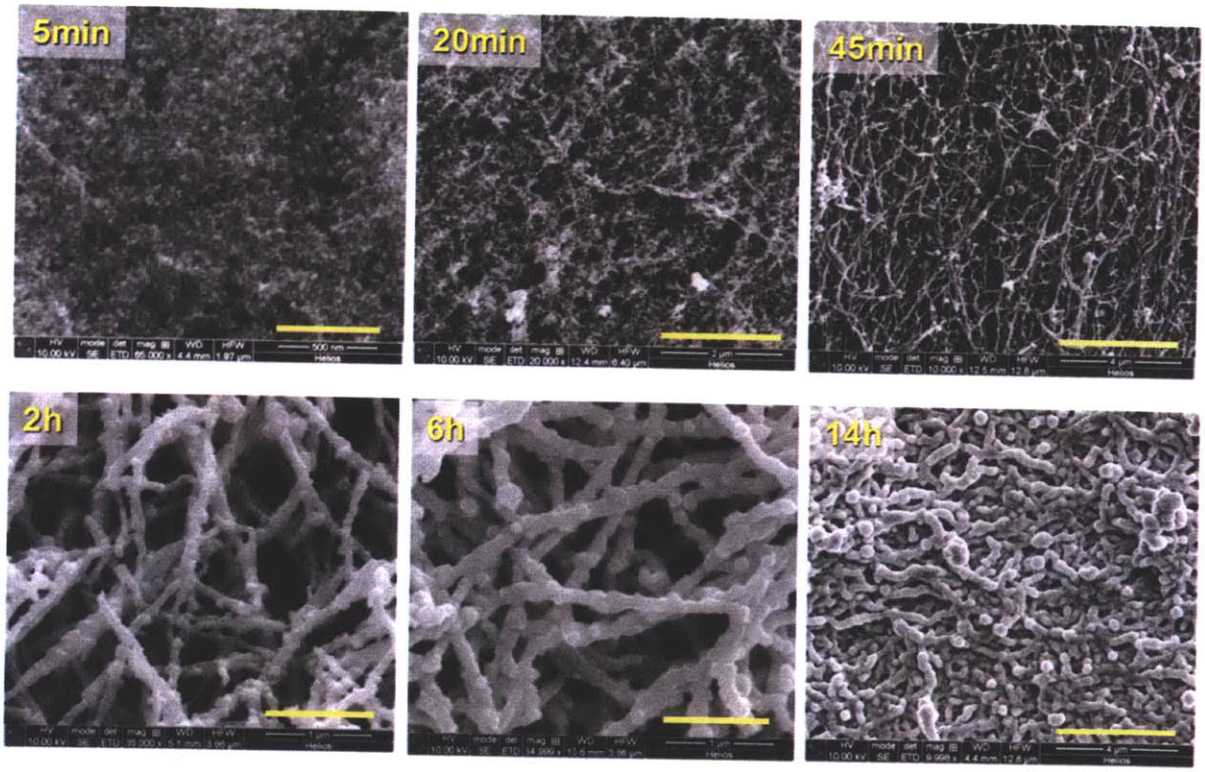

Figure 2.15. Copper nanowire synthesis time course. Copper nanowires synthesized on E3. The morphology changes from nanospherical aggregates at the early time points of 5 and 20 minutes to well formed, contiguous nanowires at 6 hours. Large, overgrown nanowires are observed at 14 hours. Scale bars for each time point are: 5 min, 500nm; 20 min, 2μm; 45 min, 4μm; 2h, 1μm; 6 hours, 1μm; and 14 hours, 4μm.

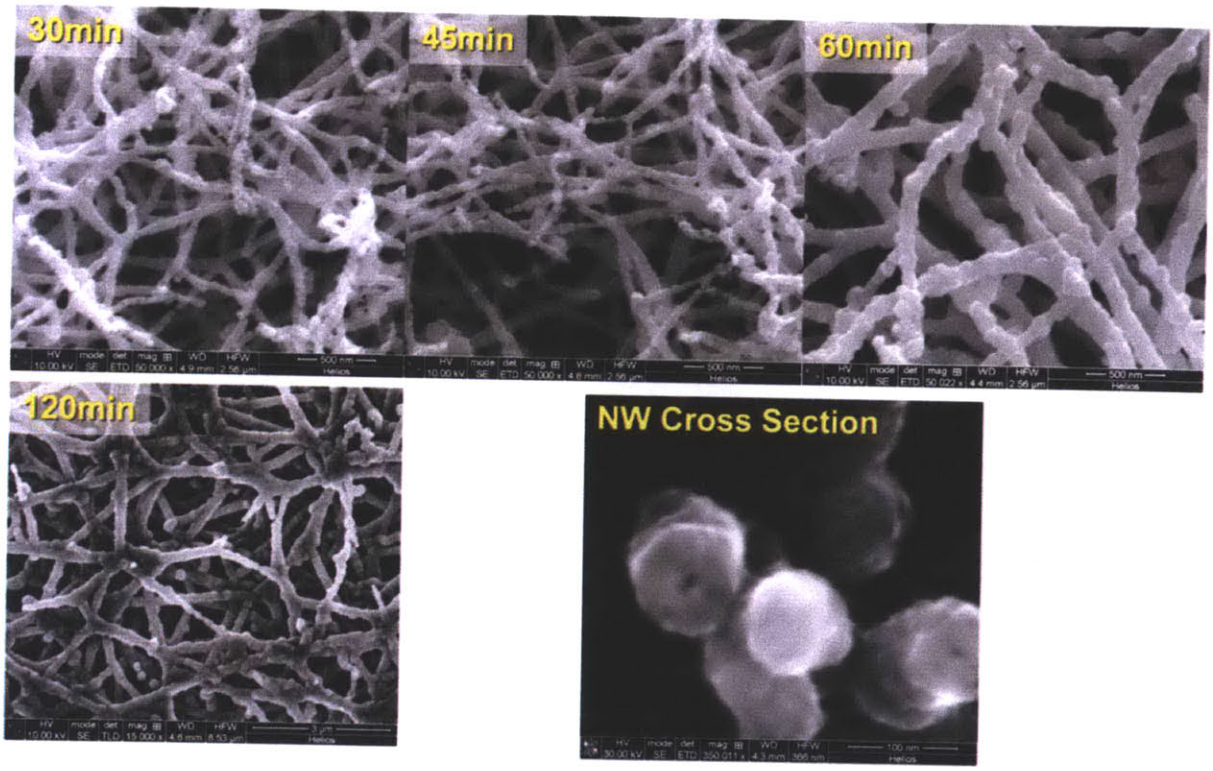

Figure 2.16. Nickel nanowire synthesis time course. Nickel nanowires synthesized on E3. The morphology changes from nanospherical particles along the virus at the early time points of 30 and 45 minutes to well formed, contiguous nanowires at 60 and 120 minutes. The lower right image shows nanowire cross-sections with approximately 9nm holes in the center where the virus template should be. Scale bars for each time point are 500nm except 120min which is 3μm. The scale bar for the NW Cross Section is 100nm.

corresponds to the emergence of contiguous nanowires in the Figure 2.15 SEM images. Similarly for nickel nanowires, there appears to be a transition from a power law relationship to linear growth at 45 minutes. This time corresponds to nearly contiguous nanowires in the Figure 2.16 SEM images, just prior to fully contiguous nanowires are observed at 60min. The power law and linear curve fits are shown for copper and nickel nanowire growth in Figure 2.19 (A) and Figure 2.20 (A) respectively.

The power law portion of the growth curves was analyzed using the Johnson-Mehl-Avrami-Kolmogorov (JMAK) equation, often employed for nucleation and growth processes.[38] The JMAK equation is often presented in the following form.

$$Y = 1 - \exp(-kt^n) \quad (1)$$

Y is the fraction of transformed material, k is the rate parameter, and n is known as the Avrami exponent. Recast in the form,

$$\ln[-\ln(1-Y)] = n\ln(t) + \ln(k) \quad (2)$$

plotting ln[-ln(1-Y)] versus ln(t) should result in a linear plot with a slope of n, the Avrami exponent. Interpretation of the Avrami exponent lends insight into the rate of nucleation and growth of the material transformation.

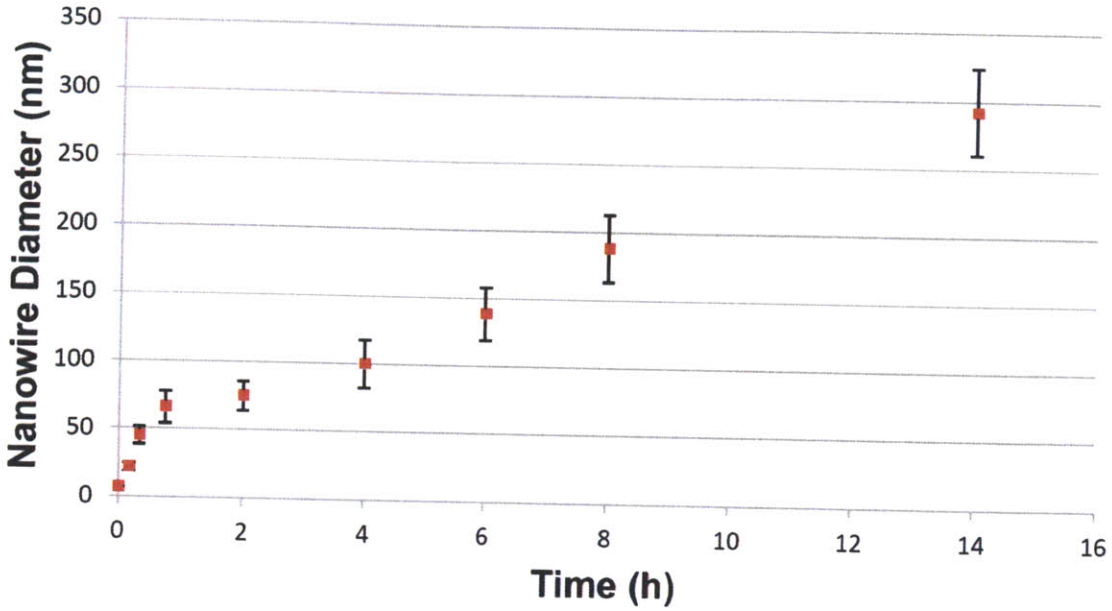

Figure 2.17. Copper nanowire diameter as a function of synthesis time.

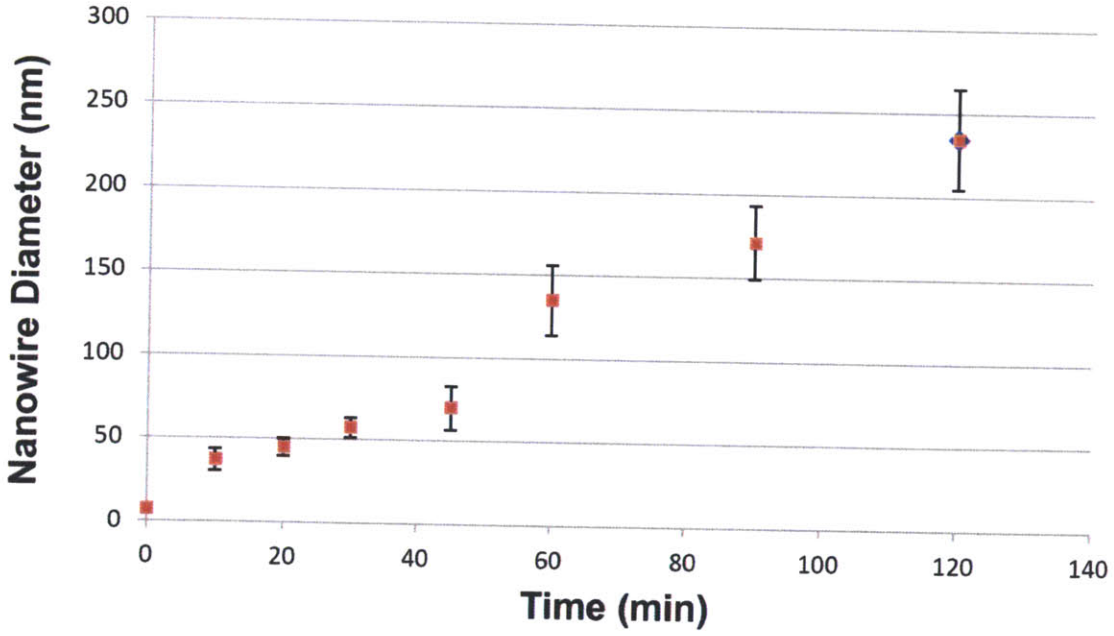

Figure 2.18. Nickel nanowire diameter as a function of time.

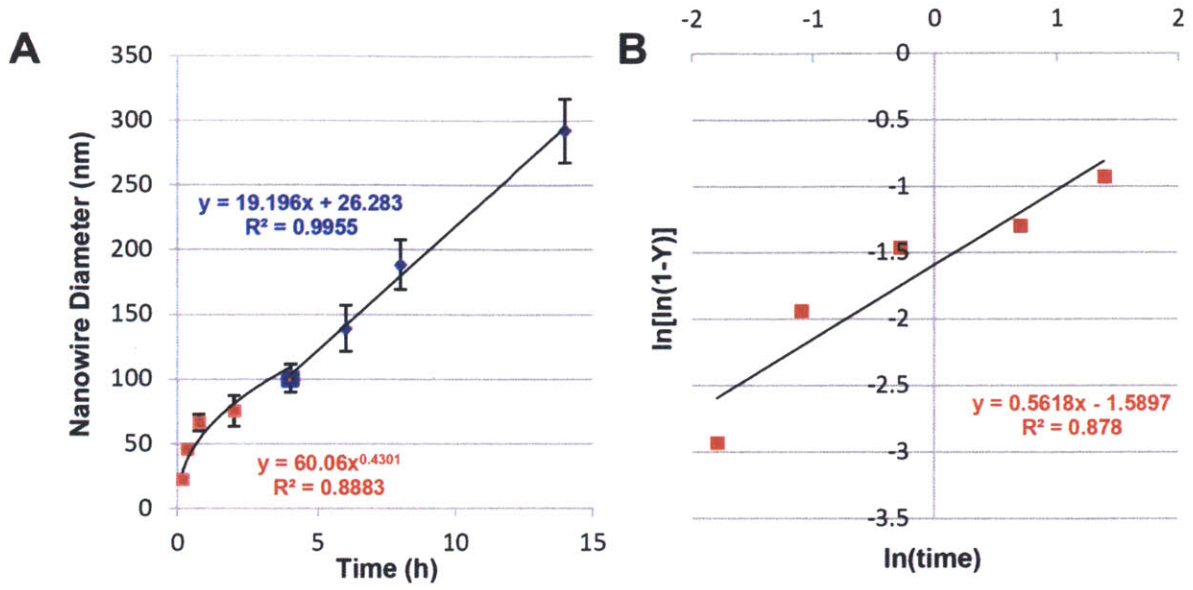

Figure 2.19. Copper nanowire diameter as a function of synthesis time; curve fit. A) Initial power law growth curve fit is shown in red. The linear growth curve fit is shown in blue. B) Plot of ln[ln(1-Y)] vs ln(time). Avrami exponent equals 0.5618.

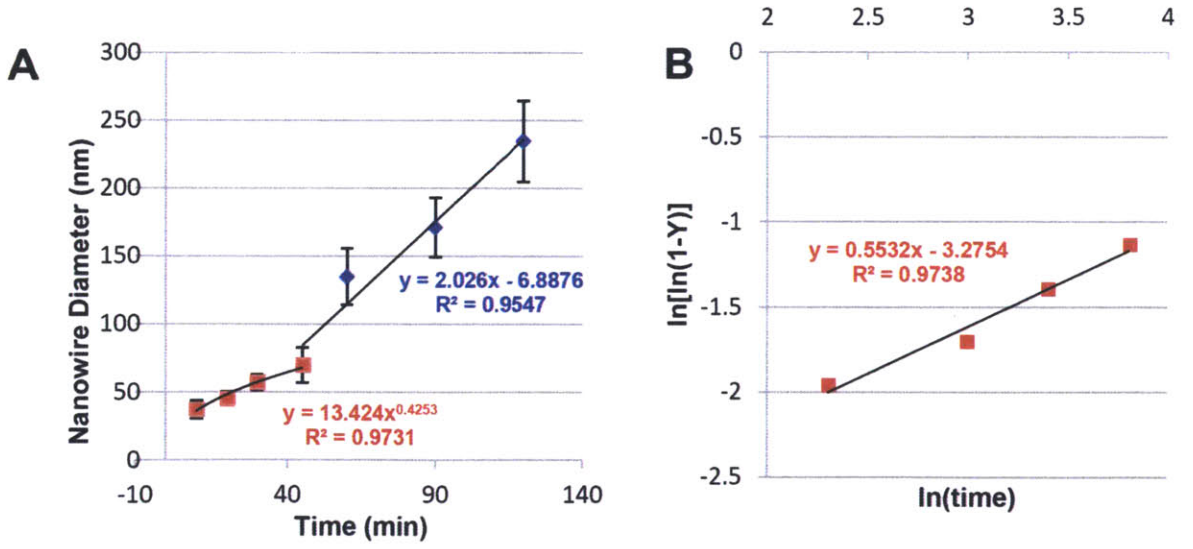

Figure 2.20. Nickel nanowire diameter as a function of time; curve fit. A) Initial power law growth curve fit is shown in red. The linear growth curve fit is shown in blue. B) Plot of ln[ln(1-Y)] vs ln(time). Avrami exponent equals 0.5532.

The initial growth phase for copper and nickel mineralization was plotted in the form of Equation 2 above. The linear plots are presented in Figure 2.19 (B) and Figure 2.20 (B). Full transformation of the material, or Y = 1, was determined as the nanowire diameter of the next higher data point beyond the initial growth phase. The Avrami exponents are 0.5618 and 0.5532 for copper and nickel respectively. These values are just slightly higher than 0.5. The Avrami exponent close to 0.5 suggests a diffusion controlled process, with one-dimensional growth where the nucleation sites are rapidly used up.[39] This interpretation seems consistent with the synthesis method in that all the catalytic palladium sites would be rapid plated over with nickel with no further nucleation. Diffusion controlled growth seems consistent with a precipitation reaction.

2.3.5. Film Thickness Control.

With the ability to control the diameter of the nanowires, control over film thickness was explored next. Intuitively the thicker the starting phage gel is, the thicker the resulting mineralized scaffold should be. Given the high water content of hydrogels, upwards of 99%, a contraction of film thickness due to water loss and capillary forces is expected similar to that observed with sol-gels.[40] The nanowire scaffold film thicknesses were measured using profilometery for range of phage concentrations of $1x10^{13}$ to $1x10^{14}$pfu/ml and the metal reduction times investigated in Section 2.2.4. An average of 96.4±3.4% thickness reduction occurred from the starting hydrogel to dried copper or nickel film thickness. Copper nanowire films were ion etched using a dual beam scanning electron microscope/focused ion beam (SEM/FIB) to image the cross-sectional film thickness. Figure 2.21 demonstrates the ability to

control a nine-fold scaling over the thickness of a copper nanowire films synthesized on E3 at a concentration of $7x10^{13}$pfu/ml with a 6 hour electroless copper deposition. By controlling the surface area covered by a given volume of virus solution, gels with a desired thickness can be formed, such that when they dry, the expected water loss and thickness decrease results in a nanowire scaffold of desired thickness. Copper nanowire films 64μm thick

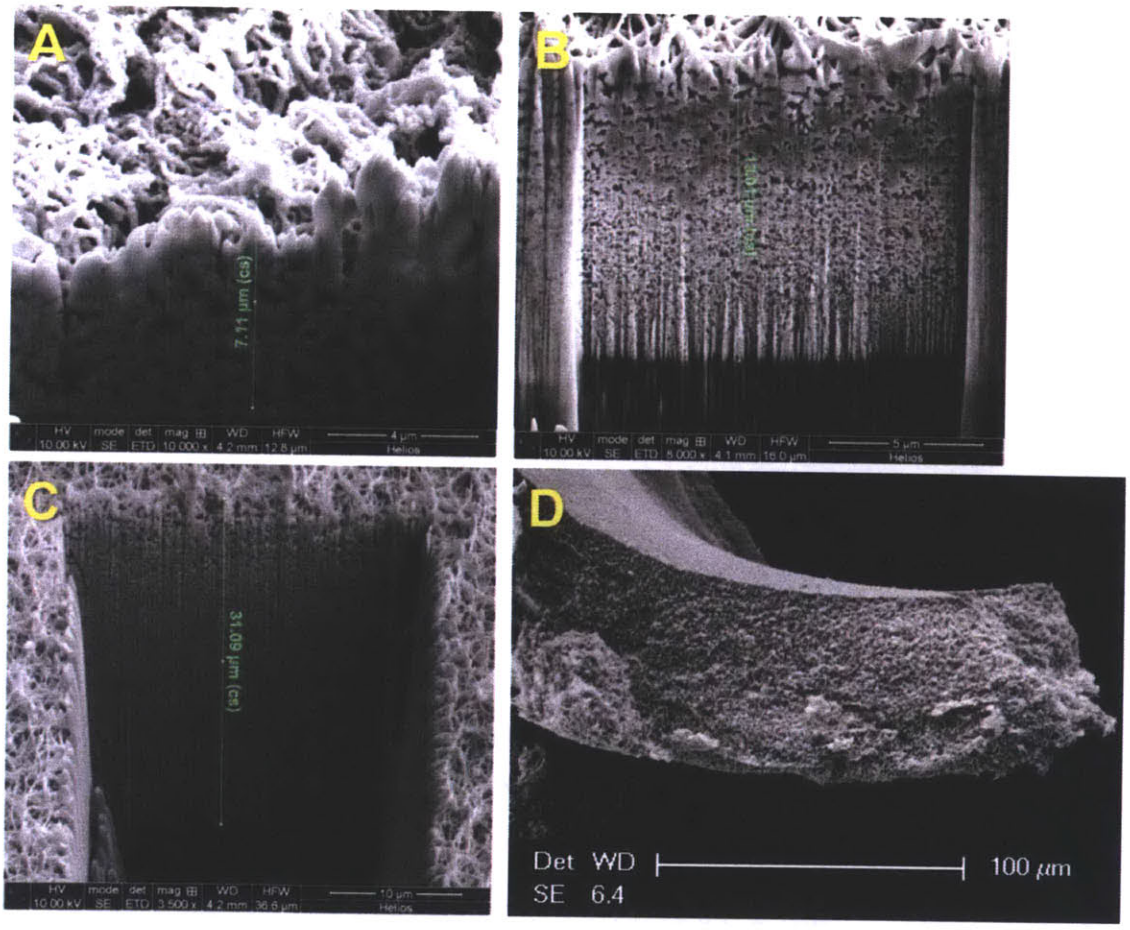

Figure 2.21. Copper nanowire scaffold thickness scaling. SEM images were obtained using a focused ion beam (FIB) etch to determine film thickness. Green measurement lines are corrected for the 52° stage tilt. A) Film thickness is 7μm. B) Film thickness is 13μm. C) Film thickness is 31μm. D) Film thickness is 64μm. Copper film in D) was mechanically fractured and imaged with an ESEM.

2.3..6 Porosity Control

With the ability to control nanowire diameter and film thickness, the next parameter explored for tunability was porosity. Given the dynamic processes and parameters involved during the nanowire network synthesis, to include initial phage concentration, phage clone, hydrogel cross-linking time, nanowire diameter, and method of drying, the resulting porosity is likely a convolution of these factors. Two parameters were analyzed as possible methods to control scaffold porosity. The first was the phage clone. Of the two virus clones used in this study, E3 and Y21M, both have identical solvent exposed proteins on the viral capsid. The Y21M clone, however, has a mutation from tyrosine to methionine at the 21st residue on the p8 coat protein. This site specific mutation gives the Y21M clone a persistence length of 9.9±0.7μm compared to 2.8±0.7μm for wild type M13.[18] The longer persistence length of the Y21M was hypothesized to result in longer element lengths in hydrogel formation, and consequently result in increased inorganic scaffold porosity when compared to the E3 bio-template. The second method used in an attempt to control porosity was the use of freeze drying. Once the metal nanowire films were synthesized and rinsed, the still hydrated films were subject to a freeze drying process. The expectation was that the capillary forces created during film drying could be avoided, preserving a higher porosity in the film. A fixed phage concentration of $7x10^{13}$pfu/ml was used for both E3 and Y21M clones in both copper and nickel deposition baths.

Three methods were used to analyze the nanowire network film porosities. 1) Gravimetric analysis was performed by dividing the film mass by the film volume determined from profilometry. A fractional comparison of the gravimetric density is made with bulk metal and accounting for the volume of the biotemplate to determine the film porosity. 2) SEM/FIB cross-section images were used to analyze film porosity using ImageJ software. For each full film

thickness cross section shown in Figure 2.22, a series of more detailed images were taken with a horizontal full width (HFW) of 5.12μm. The detailed cross section images were adjusted to maximize contrast, thresholded to identify the cross-section interfacial area, converted to a binary image and then analyzed using the Analyze Particles function on ImageJ. The analysis output indicates a 2-dimensional cross section porosity and surface area. An example of this method is shown in Figure 2.22. 3) Mercury porosimetry was performed as a third technique to determine the porosity of E3 and Y21M copper samples. The intrusion volume was determined from the inflection point on intrusion volume versus pressure curves. The intrusion volume represents the porous void space within the sample. The solid mass of the scaffolds was assumed to have the density of bulk copper, 8.94g/cm^3, or bulk nickel, 8.91g/cm^3. The sample porosity is determined when the sample mass is normalized by the total of intrusion and solid volumes. The differential intrusion volume versus pore size from mercury porosimetry gives a relative distribution of the pore sizes within the scaffolds and is shown in Figure 2.24.

The results of the three methods to determine porosity are shown in Table 2.1. Gravimetrically determined porosities were higher than the porosities determined from image analysis. The gravimetric porosities appear to support the hypothesis that the stiff Y21M phage clone will yield more porous structures. The lower porosity values determined from image analysis may result from the challenge of eliminating nanowires imaged behind the ion beam cross-sectional plane during image processing. Binary conversion of any of background nanowires will have the effect of increasing the appearance of nanowire volume leading to a lower estimate of porosity. Image analysis results indicate the same trend of increased porosity values when the Y21M stiff phage is used. The mercury intrusion porosimeter values are lower

than those for gravimetric and image analysis and indicate the reverse trend in porosity for the phage clone used.

The mercury porosimetry differential intrusion versus pore volume data for the E3 copper films in Figure 2.24 indicates a large number of pores with diameters of 4μm, 180nm, 95nm, 70nm and 45nm and peaks of 800nm, 450nm, 95nm and 20nm for the Y21M clone. These peak distributions generally follow the pore distributions observed in SEM imagery. The discrete versus continuous pore size distribution in Figure 2.24, and lack of peaks between 95nm and 20nm for the Y21M copper films, likely results from instrument negative intrusion values at high pressures where the total intrusion volume for a small sample mass approaches the sample chamber compression. Based on these results, significantly more sample mass would be required to generate more reliable porosity and pore size distribution values from mercury intrusion porosimetry.

Based on the average porosity value of the gravimetric and image analysis, the Y21M stiff phage provides a roughly 10% increase in porosity. The freeze drying method results in an E3 copper film that is over 20% more porous than with ambient temperature drying. The ability to scale the film porosity between 10-20% for a fixed phage concentration and nanowire diameters suggests a broader range of porosity control over a wider range of those parameters. Supporting SEM imagery not presented here also supports this idea. With 3-dimensional phage film porosities of approximately 50% and greater, sufficient void space exists to further functionalize the porous material.

Table 2.1. Nanowire Scaffold % Porosity					
Method	E3 Cu	Y21M Cu	E3 Ni	Y21M Ni	E3 Cu-Freeze
Gravimetric	60.6±1.7	73.2±9.3	49.0±0.4	66.9±8.7	89.3
Image Analysis	48.6	56.3	46.6	52.1	62.1
Mercury Porosimetry	39.8	32.4	NA	NA	NA
Average Gravimetric & Image Analysis	54.6	64.8	47.8	59.5	75.7

Figure 2.22. Grayscale to binary image conversion and analysis. The FIB cross-section is from a copper nanowire network on the Y21M clone. A) The original image contrast is maximized. B) The image is thresholded to identify the cross-section surface area. C) The image is converted to an 8-bit binary image for particle analysis. The nanowires are colored black. Image scale is 5.12μm horizontal full width. This sample section has a determined porosity of 46.6%.

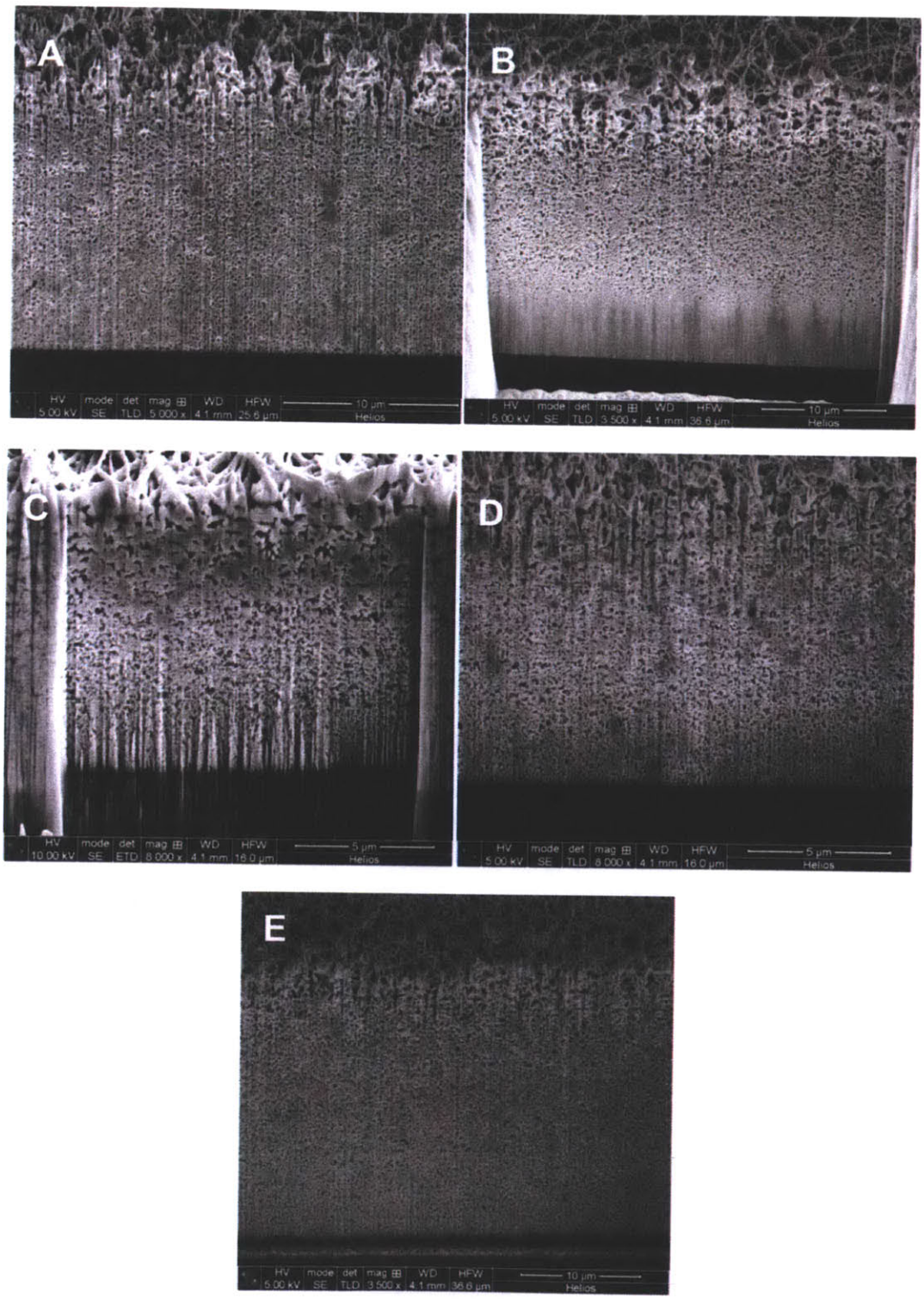

Figure 2.23. Nanowire film FIB cross-sections. A) Copper nanowires on E3. Film thickness is 20.18μm. B) Copper nanowires on Y21M. Film thickness is 29.10μm. C) Nickel nanowires on E3. Film thickness is 13.01μm. D) Nickel nanowires on Y21M. Film thickness is 14.00μm. E) Freeze dried copper nanowires on E3. Film thickness is 31.00μm.

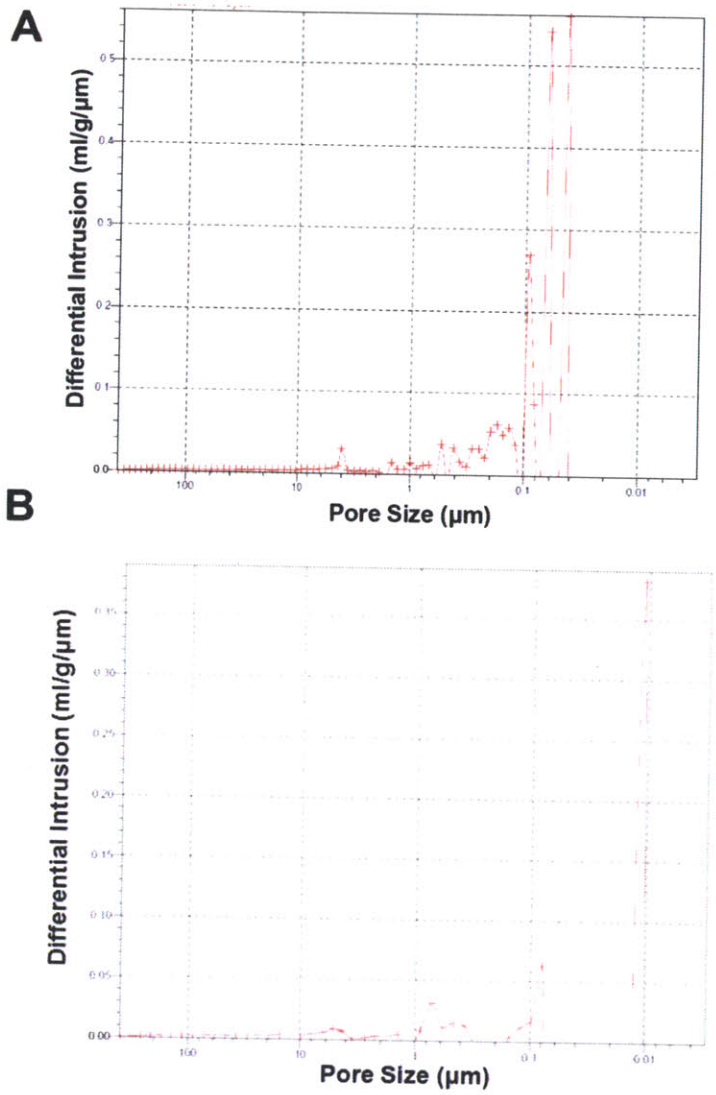

Figure 2.24. Mercury porosimetry differential intrusion versus pore size for E3 and Y21M copper films. A) Differential intrusion for the E3 clone. Data peaks indicate a large number of pores with diameters of 4µm, 180nm, 95nm, 70nm and 45nm. B) Differential intrusion for the Y21M clone. Data peaks indicate a large number of pores with diameters of 800nm, 450nm, 95nm and 20nm.

2.3.7. Nano-Network Conductivity.

With a tunable 3-dimensional nanowire scaffold, the next material parameter investigated was electrical resistivity. Prior to conducting electrical measurements on the nanowire films, a basic model was constructed to estimate expected resistivity values. The Ogston rigid fiber model was used as a starting point to conceptualize the geometry of the 3-dimensional scaffold, or more specifically the pore size. The Ogston model predicts that for a collection of infinitely thin rigid fibers, the average pore size is a function of the rod length and the concentration of rods according to the following equation.[41]

$$D = \frac{1}{\sqrt{4\pi\nu L}} \tag{3}$$

Here ν is the concentration of fibers, L is the length of an individual element and D is the mean pore size. For fibers with finite thickness, the radius may be added to D. In this case, the length of the phage cross-sectional radius of 3.5 nm was added. Equation 3 was used to determine the average pore size over a range of phage concentrations from $1x10^{13}$pfu/ml to $1x10^{14}$pfu/ml for a virus hydrogel. Nanowire radii ranged up to one half of the hydrogel pore diameter. At a nanowire radius one half the pore diameter, it is assumed that the nanowire scaffold has mineralized to a solid mass of copper (neglecting the virus biotemplate which is less than 0.05% mass of a 100nm diameter copper nanowire). Copper nanowires were modeled solid as wires with a bulk resistivity of $1.68x10^{-8}\Omega m$. Resistance of a representative cubic $1\mu m^3$ volume element was determined using the relationship,

$$R = \frac{\rho l}{A} \tag{4}$$

In this case, the available cross sectional area is the ratio of the nanowire diameter to the pore size. The resistance of the volume element model as a function of phage concentration (and thus pore diameter) and nanowire diameter is shown in Figure 2.25. The gray plane is the point

where nanowire diameters are the same length as the pore size, and the volume element approximates solid copper. Based on the cubic $1\mu m^3$ volume element modeled, for any given combination of nanowire diameter and initial phage concentration, the resulting resistance R can be multiplied 10^{-6}m to determine the porous scaffold resistivity in Ωm. Ultimately the resistance and resistivity of the nanowire scale as a factor of the porosity, or cross-sectional area available for electron flow. One interesting aspect of Figure 2.25 is that for the phage concentrations and nanowire diameters used for both copper and nickel nanowire scaffolds, the model predicts that the nanowires will fuse into a solid material, where porous structures were characterized by SEM. This suggests that the hydrogel biotemplate may be more porous than the Ogston model suggests.

The electrical resistivity of the nanowire films on silicon substrates was tested with a four point probe. Although silicon is a semiconductor, it is many orders of magnitude more resistive than the samples. The four tungsten carbide 40.64μm probes were spaced 1.5875mm apart. For each sample, current was swept over current ranges of 100μA to 0.1A. Nickel and copper nanowire films of varying thicknesses and nanowire diameters were tested and the results are shown in Table 2.2 and Table 2.3 respectively.

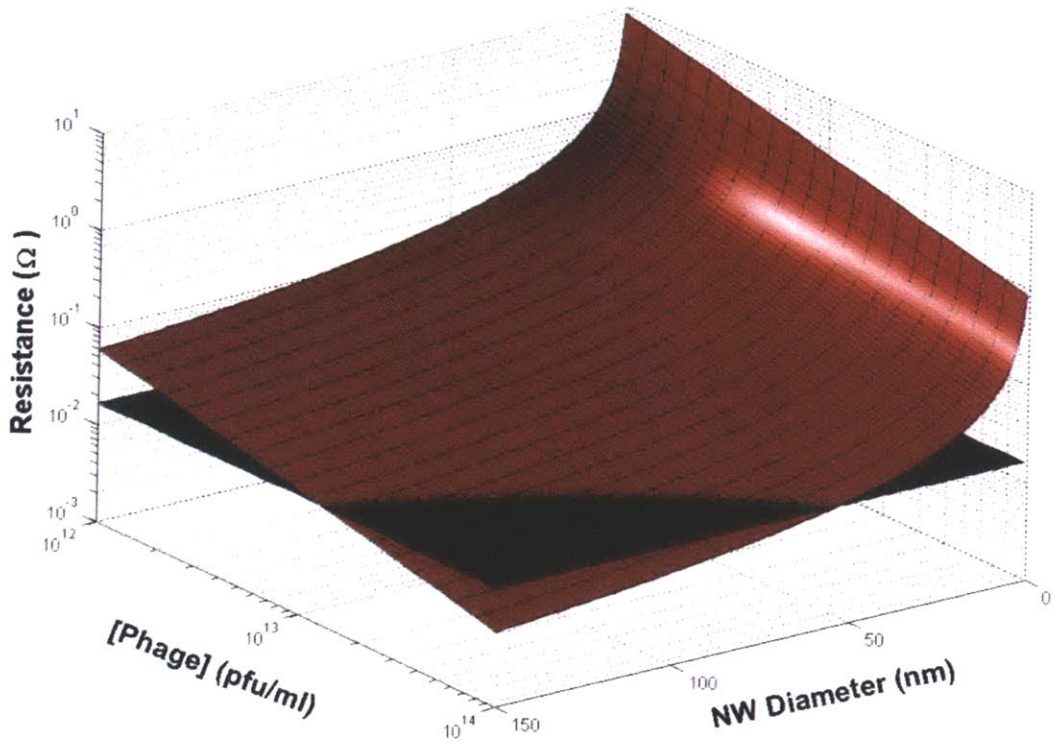

Figure 2.25. Copper nanowire scaffold resistance model. The resistance of a $1\mu m^3$ volume element as a function of hydrogel phage concentration (pfu/ml) and nanowire diameter (nm) is shown on the red surface plot. The gray plane represents the equivalent resistance of solid bulk copper, i.e. when the nanowires occupy the entire volume element. Resistance is calculated based on the cross-sectional area of nanowires in a $1\mu m^3$ cubic element. Volume element porosity is based on the ratio of the nanowire diameter to the Ogston pore size. Resistance decreases with increasing phage concentration and increasing nanowire diameter.

Table 2.2 Copper Scaffold Conductivities.

NW Diameter (nm)	Film Thickness (μm)	R (Ω)	Ω/sq	Measured ρ (Ωm)	Bulk ρ (Ωm)	$\rho_{measured}$ / ρ_{bulk}
115	10.331	0.02359	0.11	1.10E-06	**1.70E-08**	64.96
139	11.8	0.01999	0.09	1.07E-06	**1.70E-08**	62.74
188	20.9	0.01137	0.05	1.07E-06	**1.70E-08**	63.23

Table 2.3 Nickel Scaffold Conductivities.

NW Diameter (nm)	Film Thickness (μm)	R (Ω)	Ω/sq	Measured ρ (Ωm)	Bulk ρ (Ωm)	$\rho_{measured}$ / ρ_{bulk}
69.7	6.7	0.649	2.94	1.97E-05	**6.84E-08**	288.0
112.9	10.3	0.126	0.571	5.88E-06	**6.84E-08**	86.0
137.1	6.1	0.104	0.472	2.87E-06	**6.84E-08**	42.0

For both copper and nanowire films, the measured resistivity values lie within a factor of 42 to 288 of the bulk metal values as shown in the $\rho_{measured} / \rho_{bulk}$ columns of Table 2.2 and Table 2.3, where ρ_{bulk} is $1.70 \times 10^{-8} \Omega m$ for copper and $6.84 \times 10^{-8} \Omega m$ for nickel. As shown in the porosity model, the resistivity values should scale with film porosity, which taken as 50% accounts for only a factor of 2 increase over bulk resistivity. The additional increase in resistivity likely comes from the numerous grain boundaries present between the fused nanoparticles observed in SEM images.

2.4 Conclusions

The 3-dimensional copper and nickel nanowire networks synthesized in this work represent a novel approach to stochastically assemble 3-dimensional bio-templates from 1-dimensional elements. Control was demonstrated over nanowire diameter, film thickness and porosity. The metal networks presented resistivity values to within an order of magnitude of their bulk material counterparts. In addition to the tunable parameters and ability to rapidly transport electrons, the nanowire scaffolds assemble into mechanically robust free standing films. All of these features should facilitate the incorporation of 3-dimensional phase-based films into numerous materials engineering applications. Additionally, the synthesis process is expected to be scalable to large area formats, possibly using roll-to-roll processing.

Further work with the 3-dimensional virus bio-template will include use for electrode materials in lithium rechargeable batteries and mechanical characterization of the 3-dimensional structures to determine their elastic moduli. Demonstrating these features will help lay the groundwork for dual functional electro-mechanical materials.

2.5 References

1. Mor, G.K., Varghese, O.K., Paulose, M., Shankar, K. & Grimes, C.A. A review on highly ordered, vertically oriented TiO2 nanotube arrays: Fabrication, material properties, and solar energy applications. *Solar Energy Materials and Solar Cells* **90**, 2011-2075 (2006).
2. Liu, H.S. et al. A review of anode catalysis in the direct methanol fuel cell. *Journal of Power Sources* **155**, 95-110 (2006).
3. Vidotti, M. & de Torresi, S.I.C. Nanochromics: Old materials, new structures and architectures for high performance devices. *Journal of the Brazilian Chemical Society* **19**, 1248-1257 (2008).
4. Arico, A.S., Bruce, P., Scrosati, B., Tarascon, J.M. & Van Schalkwijk, W. Nanostructured materials for advanced energy conversion and storage devices. *Nature Materials* **4**, 366-377 (2005).
5. Seker, E. et al. The fabrication of low-impedance nanoporous gold multiple-electrode arrays for neural electrophysiology studies. *Nanotechnology* **21** (2010).
6. Li, H.Q. & Misra, A. A dramatic increase in the strength of a nanoporous Pt-Ni alloy induced by annealing. *Scripta Materialia* **63**, 1169-1172 (2010).
7. Gu, Z.Y., Ye, H.K., Bernfeld, A., Livi, K.J.T. & Gracias, D.H. Three-dimensional electrically interconnected nanowire networks formed by diffusion bonding. *Langmuir* **23**, 979-982 (2007).
8. Yuan, M.J. et al. Preparation and enhanced electrochromic property of three-dimensional ordered mesostructured mixed tungsten-titanium oxides. *Chemistry Letters* **33**, 1396-1397 (2004).
9. Hong, B.H., Bae, S.C., Lee, C.W., Jeong, S. & Kim, K.S. Ultrathin single-crystalline silver nanowire arrays formed in an ambient solution phase. *Science* **294**, 348-351 (2001).
10. Romo-Herrera, J.M., Terrones, M., Terrones, H., Dag, S. & Meunier, V. Covalent 2D and 3D networks from 1D nanostructures: Designing new materials. *Nano Letters* **7**, 570-576 (2007).
11. Lee, S.W., Lee, S.K. & Belcher, A.M. Virus-based alignment of inorganic, organic, and biological nanosized materials. *Advanced Materials* **15**, 689-692 (2003).
12. Nam, K.T. et al. Virus enabled synthesis and assembly of nanowires for Lithium ion battery electrode. *Abstracts of Papers of the American Chemical Society* **231**, - (2006).
13. Lee, Y.J. et al. Fabricating Genetically Engineered High-Power Lithium-Ion Batteries Using Multiple Virus Genes. *Science* **324**, 1051-1055 (2009).
14. Ni, J.P., Lee, S.W., White, J.M. & Belcher, A.M. Molecular orientation of a ZnS-nanocrystal-modified M13 virus on a silicon substrate. *Journal of Polymer Science Part B-Polymer Physics* **42**, 629-635 (2004).
15. Chiang, C.Y. et al. Weaving genetically engineered functionality into mechanically robust virus fibers. *Advanced Materials* **19**, 826-+ (2007).
16. Lee, S.W., Wood, B.M. & Belcher, A.M. Chiral smectic C structures of virus-based films. *Langmuir* **19**, 1592-1598 (2003).
17. Tan, W.M. et al. Effects of temperature and Y21M mutation on conformational heterogeneity of the major coat protein (pVIII) of filamentous bacteriophage fd. *Journal of Molecular Biology* **286**, 787-796 (1999).
18. Blanco, P., Kriegs, H., Lettinga, M.P., Holmqvist, P. & Wiegand, S. Thermal Diffusion of a Stiff Rod-Like Mutant Y21M fd-Virus. *Biomacromolecules* **12**, 1602-1609 (2011).
19. Rasband, W.S. ImageJ, U. S. National Institutes of Health, Bethesda, Maryland, USA. (1997-2005).
20. Mao, J.Y., Belcher, A.M. & Van Vliet, K.J. Genetically Engineered Phage Fibers and Coatings for Antibacterial Applications. *Advanced Functional Materials* **20**, 209-214 (2010).
21. Lee, S.W. & Belcher, A.M. Virus-based fabrication of micro- and nanofibers using electrospinning. *Nano Letters* **4**, 387-390 (2004).

22. Migneault, I., Dartiguenave, C., Bertrand, M.J. & Waldron, K.C. Glutaraldehyde: behavior in aqueous solution, reaction with proteins, and application to enzyme crosslinking. *Biotechniques* **37**, 790-+ (2004).
23. http://www.jmol.org/ Jmol: an open-source Java viewer for chemical structures in 3D.
24. Chang, S.Y., Hsu, C.J., Fang, R.H. & Lin, S.J. Electrochemical deposition of nanoscaled palladium catalysts for 65 nm copper metallization. *Journal of the Electrochemical Society* **150**, C603-C607 (2003).
25. Balci, S. et al. Copper nanowires within the central channel of tobacco mosaic virus particles. *Electrochimica Acta* **51**, 6251-6257 (2006).
26. Royston, E., Ghosh, A., Kofinas, P., Harris, M.T. & Culver, J.N. Self-assembly of virus-structured high surface area nanomaterials and their application as battery electrodes. *Langmuir* **24**, 906-912 (2008).
27. Kudo, H. & Fujihira, M. DNA-Templated copper nanowire fabrication by a two-step process involving electroless metallization. *Ieee Transactions on Nanotechnology* **5**, 90-92 (2006).
28. Jagannathan, R. & Krishnan, M. Electroless Plating of Copper at a Low Ph Level. *Ibm Journal of Research and Development* **37**, 117-123 (1993).
29. Lim, J.S. et al. Surface functionalized silica as a toolkit for studying aqueous phase palladium adsorption and mineralization on thiol moiety in the absence of external reducing agents. *Journal of Colloid and Interface Science* **356**, 31-36 (2011).
30. Gu, Q., Cheng, C.D. & Haynie, D.T. Cobalt metallization of DNA: toward magnetic nanowires. *Nanotechnology* **16**, 1358-1363 (2005).
31. Lee, S.Y., Royston, E., Culver, J.N. & Harris, M.T. Improved metal cluster deposition on a genetically engineered tobacco mosaic virus template. *Nanotechnology* **16**, S435-S441 (2005).
32. Tait, C.D., Janecky, D.R. & Rogers, P.S.Z. Speciation of Aqueous Palladium(Ii) Chloride Solutions Using Optical Spectroscopies. *Geochimica Et Cosmochimica Acta* **55**, 1253-1264 (1991).
33. Dujardin, E., Peet, C., Stubbs, G., Culver, J.N. & Mann, S. Organization of Metallic Nanoparticles Using Tobacco Mosaic Virus Templates. *Nano Letters* **3**, 413-417 (2003).
34. Lee, I., Hammond, P.T. & Rubner, M.F. Selective electroless nickel plating of particle arrays on polyelectrolyte multilayers. *Chemistry of Materials* **15**, 4583-4589 (2003).
35. Barker, B.D. Electroless Deposition of Metals. *Surface Technology* **12**, 77-88 (1981).
36. Schlesinger, M. in Modern Electroplating 447-458 (John Wiley & Sons, Inc.
37. Lifshitz, I.M. & Stepanova, G.I. Correlation in Solid Solutions. *Soviet Physics Jetp-Ussr* **6**, 379-386 (1958).
38. Avrami, M. Kinetics of phase change I - General theory. *Journal of Chemical Physics* **7**, 1103-1112 (1939).
39. Hosford, W.F. Materials science:
an intermediate text. (Cambridge University Press, 2007).
40. Hench, L.L. & West, J.K. The Sol-Gel Process. *Chemical Reviews* **90**, 33-72 (1990).
41. Ogston, A.G. The Spaces in a Uniform Random Suspension of Fibres. *Transactions of the Faraday Society* **54**, 1754-1757 (1958).

CHAPTER 3

3-Dimensional Phage-Templated Copper-Tin Nanowire Networks for Lithium Rechargeable Batteries

3.1 Introduction

There is much interest in high capacity anode materials such as tin and silicon for use in lithium rechargeable batteries. With electrical storage capacities roughly a factor of 3-10 times higher than conventional anodes, successful development of such materials would provide a significant increase in electrical storage capability. The primary challenge with tin and silicon as anode materials is the large volumetric expansion that occurs upon lithiation that can exceed 300%.[1] This large volume change during battery cycling results in repeated strain, fatigue, cracking, and ultimately pulverization of the anode material.[1] Numerous strategies have been employed to mitigate the deleterious effects from volume expansion and contraction. Nano-architectures have provided a means to reduce particle size, and thus control the extent of volume expansion.[2] Further, the use of nano-particles within 3-dimensional electrode architectures has enabled stable capacity retention with extended cycling.[3,4]

One of the common electrode architectures studied is that of nano-pillars synthesized on and orthogonal to a current collecting substrate.[3,4] The benefit of such an approach is the significant increase in surface area when compared to a 2-dimensional substrate. The increase in surface area relative to active material volume increases the area for lithium intercalation and de-intercalation. Nano-sized tin or silicon particles bound to conductive metal pillars demonstrated high rate performance for thin film applications.[3] For the use of tin as an electrode material, incorporation into a binary alloy with metals such as copper appears to result in a buffering of mechanical strain due to volume changes, thus increasing cycle life.[2,5,6] The development of the nano-pillar electrode architecture facilitates an envisioned interdigitated 3-dimensional battery cell that minimizes the diffusion pathway of lithium both between electrodes and within the

active material.[7] While inorganic electrochemical methods have dominated the development of 3-dimensional electrodes, bio-templating has been demonstrated as a fabrication method, as well. The tobacco mosaic virus was used to form metalized nano-pillars onto which silicon was applied with chemical vapor deposition.[8, 9]

Another design approach to accommodating electrode material volume change includes synthesizing active electrode material as 3-dimensional metal foams.[10] The metal foam electrode architecture offers significant void volume to accommodate tin volume expansion. Although a 3-dimensional network may not be amenable to an interdigitated integrated cell, it does offer an even greater increase in surface area when compared on a volumetric basis to a pillar architecture. A low-cost method to synthesizing scalable three-dimensional battery electrodes to achieve high power and energy densities would help to advance the field of 3-dimensional electrodes.

As demonstrated in Chapter 2, the M13 bacteriophage can be utilized as a bio-template to synthesize 3-dimensional porous metal nanowire networks. The networks demonstrated the ability to control 1) nanowire diameter, 2) network film thickness and 3) porosity. The 3-dimensional copper nanowire network is attractive in that it provides a starting point to synthesize tin nanowires via a galvanic displacement reaction. In a chemical displacement, also known as immersion plating, a spontaneous exchange occurs between a metal substrate and a more noble cation in solution. The addition of complexing agents can dramatically change the free energy state of the reactants, and can even change the order of displacement.[11] While tin possesses a lower reduction potential than copper and should not facilitate a galvanic displacement, low pH solutions with complexants to stabilize copper ions have long been demonstrated as a means of plating tin on copper substrates.[12-14] Another technique, known as

contact plating, is to place the substrate in contact with a metal with a lower voltage potential to provide a source of reducing electrons.[15] In general, the reaction for copper to tin displacement is,

$$Cu + Sn^{2+} \rightarrow Sn + Cu^{2+} \qquad (1)$$

Using acid to lower the pH, adding a complexing agent, or placing the copper in contact with a lower voltage potential metal, the copper to tin displacement can proceed.[12, 14] Tin electrodeposition and immersion coatings can result not only in a surface layer of tin, but also intermetallic compounds such as Cu_3Sn and Cu_6Sn_5 at the copper-tin interface.[6]

Based on the tin immersion plating process, a starting hypothetical model for the displacement of copper nanowires to tin is shown in Figure 3.1. Starting with virtually pure copper nanowires immersed in a tin plating solution, an initial intermetallic interfacial layer forms shown in brown in Figure 3.1. As immersion time continues the intermetallic layer progresses inward while a pure tin layer forms on the surface. Copper-tin displacement reactions have been observed to achieve coating thicknesses in excess of a micron.[12] For nanowires with diameters less than half a micron, it is expected that given a sufficient amount of plating time the entire nanowire mass is will displace to tin. This is shown on the right-hand side of Figure 3.1.

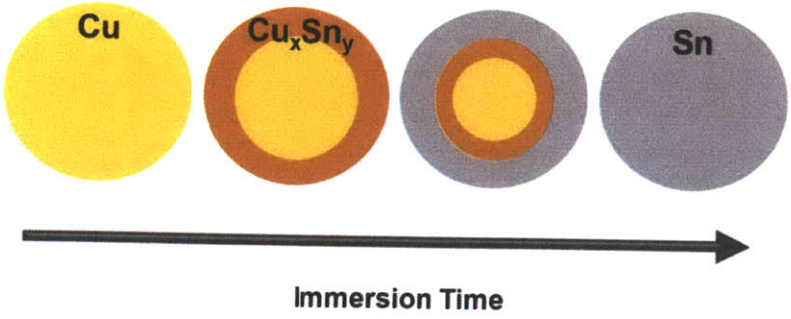

Figure 3.1. Tin immersion plating concept. Copper nanowire cross-sections are depicted with expected compositional changes as a function of time exposure in the tin immersion plating solution. Sequentially in time, from left to right in the figure, copper nanowires (yellow) form a copper tin alloy (Cu_xSn_y) (brown) on the exterior surface. As time progresses, the alloy zone moves inward with tin (gray) forming on the exterior of the nanowire. Finally, if the exposure time is sufficiently long, nanowires are expected to completely convert to tin.

In this work we demonstrate the ability of 3-dimensionsal virus-templated nanowire networks to serve as electrodes for lithium rechargeable batteries without the need for conductive and organic additives. The proof of concept is the synthesis of electrically contiguous copper-tin nanowire networks via displacement reactions for use as anodes in lithium rechargeable batteries. Two tin plating techniques are employed: 1) high pH contact tin immersion plating, and 2) low pH tin immersion plating. Variable time exposure of 3-dimensional copper nanowires to the low pH tin immersion solution is shown to affect the resulting nanowire morphology, material phase composition, and electrode performance. Although one-dimensional SnO nanotubules have been previously synthesized on cotton fibers (ref Zhu, 2010), to the best of the authors knowledge, this is the first report of 3-dimensionally bio-templated tin nanowires and the first report of a three dimensional virus scaffold used as a battery electrode.

3.2 Experimental

Hydrogel Preparation. E3 virus solutions of $7x10^{13}$pfu/ml stored in 1xPBS were pipetted onto single crystalline silicon substrates. The virus loading factor for test samples was 10μl on an approximately $1cm^2$ of substrate. Substrates with phage solution were inverted and placed onto a glutaraldehyde solution (50% Glutaraldehyde, Sigma Aldrich, CAS# 111-30-8). The phage solution remained in contact with the glutaraldehyde solution for 30min. Cross-linked phage solutions were removed from the glutaraldehyde solution and transferred to 1L 1xPBS for 12-24h to remove excess glutaraldehyde from the resulting hydrogel.

3-dimensional copper nanowire synthesis. Phage hydrogels were incubated in 10mM tetraaminepalladium (II) chloride monohydrate (Sigma Aldrich, CAS# 13933-31-8) for 6 hours. Excess palladium solution was removed by placing gels in 1L, 0.1M 3-(N-morpholino) propanesulfonic acid (MOPS) (Sigma Life Science, CAS# 1132-61-2) for 12 hours. The copper electroless deposition solution consisted of: 0.032M $CuSO_4 \cdot 5H_2O$ (Mallinckrodt Chemicals, CAS# 4844-02); 0.040M ethylenediamino tetraacetic acid, disodium, dehydrate (EDTA) (Mallinckrodt Chemicals, CAS# 6381-92-6); 0.1M 3-(N-morpholino) propanesulfonic acid (MOPS); 0.067M dimethyl amine borane (DMAB) (Aldrich, CAS# 74-94-2). Palladium sensitized gels were placed in the copper electroless deposition solution for 6 hours and then rinsed for 1 hour in deionized water. The resulting copper films were initially blown dry with nitrogen gas and then allowed to dry at room temperature.

Contact immersion plating. 0.02M tin (II) chloride dihydrate (Alfa Aesar, CAS # 10025-69-1) and 0.12M ethylenediamino tetraacetic acid, disodium, dehydrate (EDTA) (Mallinckrodt

Chemicals, CAS# 6381-92-6) were dissolved in 0.1M sodium hydroxide. Copper nanowire films were wetted with the tin solution. Commercial aluminum foil was placed in contact with the wetted copper film for 2-3 minutes. The copper-tin film was rinsed in deionized water for 30 minutes and then dried at room temperature.

Tin immersion plating. Tin immersion solutions consisted of: 0.129M tin (II) methansulfonate, 50% (Aldrich, CAS # 53408-94-9) ; 0.756M sodium hypophosphite monohydrate (Sigma-Aldrich, CAS # 10039-56-2) ; 1.05M thiourea (GE Healthcare, 62-56-6); and 0.789M methane sulfonic acid (Sigma-Aldrich, CAS # 75-75-2). Dry copper nanowire films were immersed in 10ml of the tin plating solution for 5, 10, 15, 30, and 45 minutes. Films were then placed in deionized water for 1 hour to quench the plating process and then dried with nitrogen gas. Additional samples were prepared using the same tin immersion solution, but samples were placed on a VWR mini-shaker at 140rpm for 5min during the plating process and then quenched and dried as above.

Scanning Electron Microscope/Focused Ion Beam. A FEI Company Helios 600i Nanolab Dual Beam SEM/FIB was used for high resolution imaging and for cross-sectional etching samples. The FEI XL-30 ESEM (Environmental Scanning Electron Microscope) was used for general purpose imaging.

Energy Dispersive X-Ray Spectroscopy. EDS was performed using the FEI Company Helios 600i Nanolab Dual Beam SEM/FIB. Samples were placed at a working distance of 10.5mm and an accelerating voltage of 10kV was used. Spectra were collected and initially analyzed for peak

identification and mass composition using INCA software. Spectra files were then exported as text files and plotted using Microsoft Excel.

X-Ray Diffractometry. X-ray diffraction (XRD) analysis was conducted on a PANalytical X'Pert Pro X-ray diffractometer with Cu K_α radiation (λ =1.54060Å), a 2Theta-Omega scan axis, and a scan step size of 80.0100s. A 1° offset was used for copper film samples in single crystalline silicon wafers to minimize silicon (100) peaks. Sample irradiation lengths varied between 0.4 and 0.6mm. Spectra were analyzed using X'Pert High Score Plus software.

Galvanostatic cell testing. Copper-tin electrodes were dried in a vacuum chamber for 6h before transfer to an argon glove box. Test cells were assembled using lithium foil as the counter electrode in a coin cell. 1M $LiPF_6$ in ethylene carbonate: dimethyl carbonate (EC: DMC, 1:1 ratio) (Ferro Corporation) was used as the electrolyte with Celgard 3501 polypropylene separators. Cells were galvanostatically tested using a Solatron Analytical 1470E potentiostat. Currents are reported using the C-rate convention C/n, where C is the capacity per gram of electrode active material corresponding to the theoretical capacity, and n is the number of hours for charge or discharge. The mass of active material was determined from averaged compositional energy dispersive X-ray analysis. Resulting cell capacities are normalized to both the active material mass with units of mAh/g, and normalized to the electrode area with units of mAh/cm^2. Electrode area was calculated from optical photographs using the Analyze Particles function in ImageJ software.[16]

3.3 Results and Discussion

3.3.1. 3-Dimensional Copper Nanowire Networks.

The starting point for the synthesis of bio-templated tin nanowires, is the M13 bacteriophage. The 880nm long, 6-7nm diameter virus particle provides a high aspect ratio building block with a high surface area to volume ratio. The E3 clone, with four carboxylic acid residues on the N-terminus of the 2,700 p8 coat proteins offers a pH tunable charge density on the virus surface.[17] At pH values higher than the virus isoelectric point of approximately pH 4.3 the negative charge density can be increased on the phage surface.[18] As described in Chapter 3, E3 virus solutions stored in phosphate buffered saline at a concentration of $5x10^{13}$pfu/ml were dropcast onto untreated silicon wafers. The silicon wafers with virus solution were inverted and placed onto a solution of 50% glutaraldehyde to facilitate cross-linking of the virus particles into a hydrogel film.

After rinsing away excess glutaraldehyde, the gels were exposed to 10mM tetraamine palladium chloride, $(NH_3)_4PdCl_2$, in order to sensitize the bio-template with catalytic sites for subsequent copper reduction. It is believed that the complex ion $[(NH3)_4Pd]^{2+}$ electrostatically binds the deprotonated carboxylic residues on the virus capsid p8 protein at near neutral pH values. After excess palladium solution is dialyzed out of the virus hydrogels, the gels were immersed in a copper electroless deposition solution (ELD) consisting of 0.032M $CuSO_4 \cdot 5H_2O$, 0.040M ethylenediamino tetraacetic acid, disodium, dehydrate (EDTA), 0.1M 3-(N-morpholino) propanesulfonic acid (MOPS buffer), and 0.067M dimethyl amine borane (DMAB). After 6 hours exposure to the ELD solution, the resulting copper films were rinsed in deionized water and dried with nitrogen gas.

Scanning electron microscope images of the 3-dimensional copper films are shown in Figure 3.2. The interconnected nanowires form a contiguous porous scaffold. A focused ion beam cross-sectional etch shown in Figure 3.2 (B) reveals the scaffold porosity from the top surface of the film down to the silicon substrate. The copper nanowire films used for subsequent tin displacement reactions were approximately 20μm thick. The nanowire diameters were approximately 145nm as determined from image analysis and the copper nanowire growth curves developed in Chapter 2.

The 3-dimensional copper nanowire scaffolds were then used as the substrate for tin displacement reactions. Two methods were demonstrated to achieve a 3-dimensional tin nanowire networks: 1) contact immersion tin plating, and 2) low pH immersion tin plating. The low pH immersion plating method was varied for immersion time to examine the effect on nanowire morphology, material composition, and electrode performance.

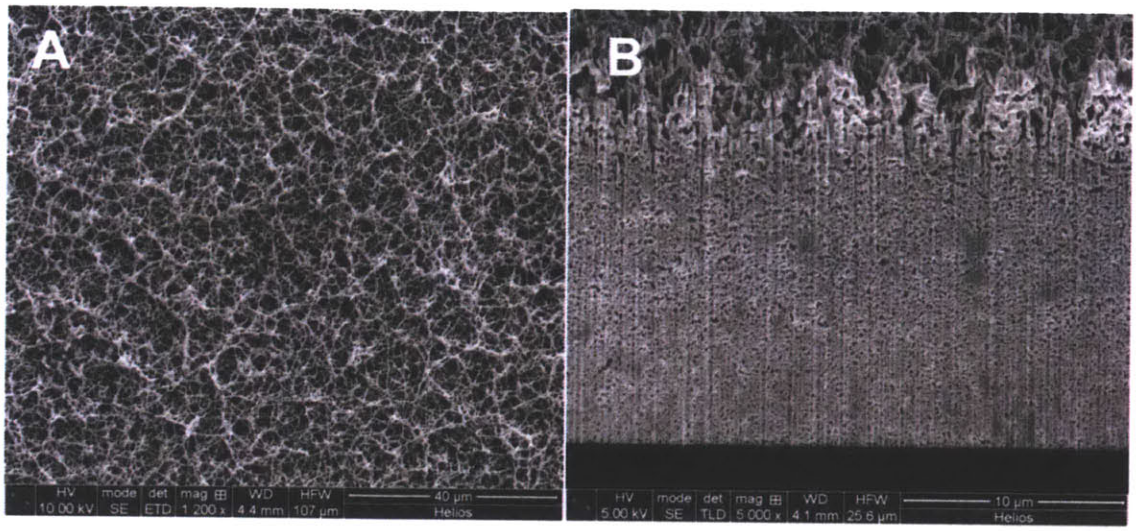

Figure 3.2. Scanning electron microscope images of 3-dimensional copper nanowire network films. A) Top-down view of a copper nanowire network. The image reveals a contiguous network of copper nanowires approximately 145nm in diameter. B) Focused ion beam cross-section etch of 3-dimensional copper networks. The image shows the interconnected void structure from the top of the film down to the silicon substrate at the bottom of the image. Film thickness is approximately 19μm. Scale bars are shown in the image margins.

3.3.2. Contact immersion plating.

To initially explore the possibility of galvanically displacing copper nanowires to tin, tin(II) chloride was dissolved in 0.1M sodium hydroxide for a final concentration of 0.02M $SnCl_2$. Ethylenediamino tetraacetic acid (EDTA) was added to the immersion solution to a final concentration of 0.12M as a complexing agent to chelate copper ions as they dissolve from the nanowire surface. With the use of a contact metal with a lower reduction potential than copper, the complexing agent enables the displacement reaction of copper to tin to proceed in a thermodynamically favored direction by lowering the free energy state of copper ions. When the copper nanowire films were wetted with the tin chloride/EDTA immersion solution, no reaction was observed to proceed. A strip of commercial aluminum foil was placed over the surface area of the wetted copper nanowire film for 2-3 minutes. Upon removal of the aluminum foil,

nanowire films were observed to delaminate from the silicon substrates. After the time period of aluminum foil contact, the film color changed from copper to exclusively a dull silver color on both the top and bottom surface of the nanowire film. The films were then rinsed in deionized water and then allowed to dry at ambient temperature. The films were free-standing and able to bend under the force of tweezers.

Initial material characterization was performed using a scanning electron microscope. The contiguous nanowire morphology seen in the initial copper nanowire films shown in Figure 3.2 was observed after the contact immersion process as seen in Figure 3.3 (A). The porous nanowire structure and inter-nanowire contacts remained intact. Energy dispersive X-ray (EDX) mapping of the nanowire film is shown in Figure 3.3 (B-F). The composite EDX map in Figure 3.3 (B) indicates areas of relatively higher concentration tin shown in yellow boxes. The evidence of uneven material composition from the contact immersion process is cause to examine other tin immersion techniques, as will be done in the next section. Figure 3.3 (F) indicates a small relative amount of aluminum evenly dispersed throughout the nanowire film. The presence of aluminum is confirmed by the EDS spectrum in Figure 3.3 (G). Composition analysis from EDS spectrum indicates a mass ratio of Cu:Sn:O:Al:Pd of 64.1:10.8:20.5:4.0:0.9.

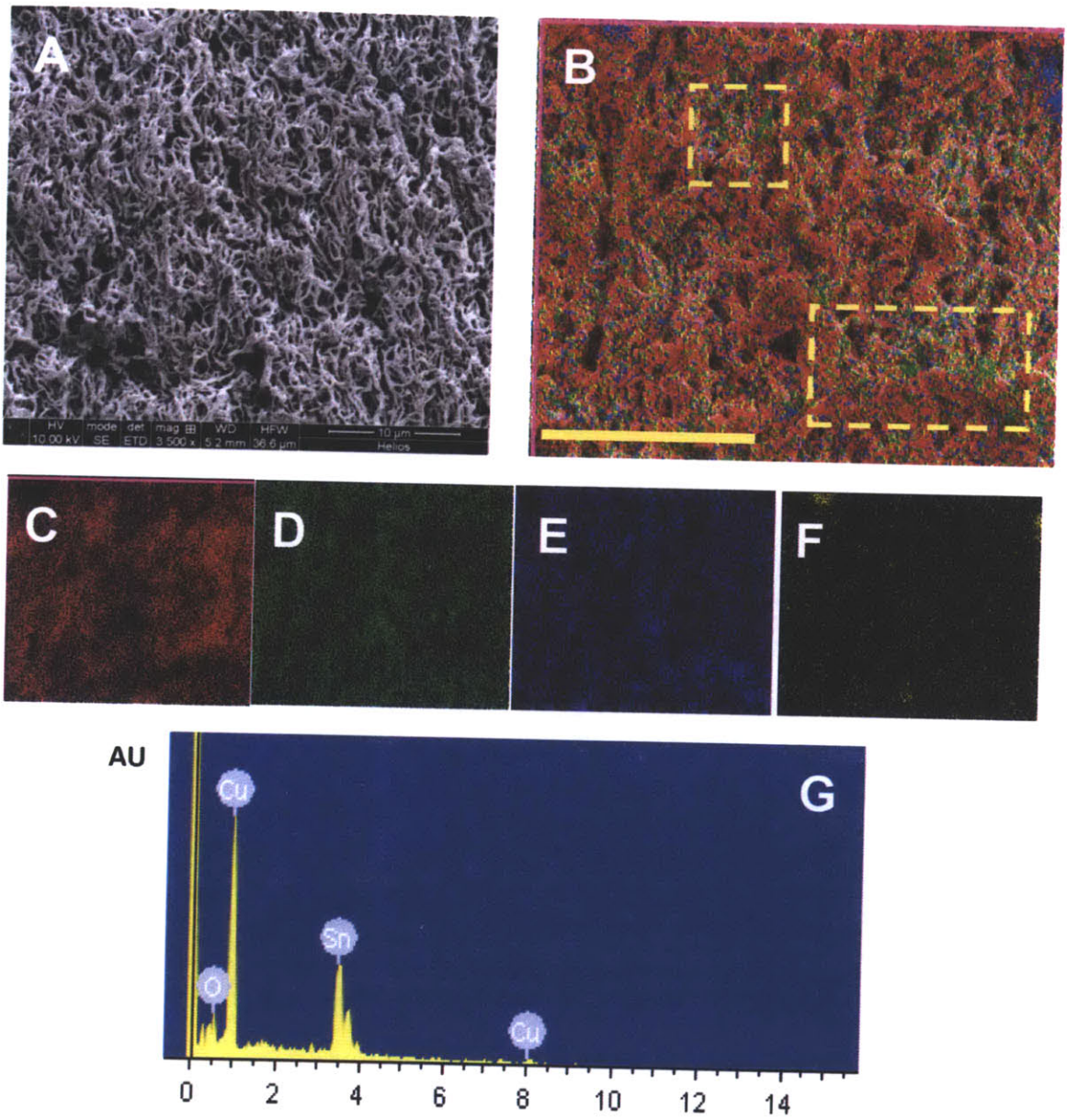

Figure 3.3. Energy dispersive X-ray spectroscopy map of tin contact immersion nanowires. A) SEM image of the mapped area. B) EDS map showing the distribution of Cu, Sn, O, and Al. Yellow dashed boxes shown regions of relative high tin concentration. Yellow scale bar is 7μm. C) Copper distribution (red). D) Tin distribution (green). E) Oxygen distribution (blue). F) Aluminum distribution (yellow). G) EDS spectrum. Composition analysis from EDS spectrum indicates a mass ratio of Cu:Sn:O:Al:Pd of 64.1:10.8:20.5:4.0:0.9.

With the confirmation of tin in the nanowire films, the electrodes were packaged under argon into coin cell assemblies using lithium foil as the counter electrode and 1M $LiPF_6$ in

ethylene carbonate: dimethyl carbonate (EC: DMC, 1:1 ratio) as the electrolyte. The EDS mass composition was used to approximate the mass of tin in the electrode. Although tin has a theoretical capacity of 994mAh/g, the high oxygen content in the EDS spectrum indicates the possibility of SnO_2 as a plating product. SnO_2 has a theoretical capacity of 781mAh/g.[4] Therefore, theoretical capacity estimate of 800mAh/g was used to calculate the various charge and discharge C-rates. C-rate is defined as the current C/n where the theoretical capacity of the electrode is discharged in n hours. Cells were galvanostatically tested between 0.01V and 2V.

The commonly accepted mechanism for the lithiation of tin is shown in equation 1.[1]

$$Sn + xLi^+ + xe^- \leftrightarrows xLiSn, \quad 0 \leq x \leq 4.4 \qquad (2)$$

This reaction is associated with a plateau of approximately 0.4 V on discharge curves.[19] When copper is alloyed with tin for the electrode material Cu_6Sn_5, the discharge mechanism is thought to proceed via two sequential steps.[10]

$$Cu_6Sn_5 + 10\ Li^+ \leftrightarrows 5Li_2CuSn + Cu \qquad (3)$$

$$5Li_2CuSn + 12Li^+ \leftrightarrows 5Li4.4Sn + 5Cu \qquad (4)$$

where reaction (3) is associated with a 0.4V plateau and reaction (3) is associated with a plateau less than 0.1V. Delithiation during charging is associated with voltage plateaus of 0.5-0.6V and 0.8V.[10]

The galvanostaic charge-discharge profiles for the contact immersion battery are shown in Figure 3.4. Figure 3.4 and subsequent charge-discharge plots show capacity as a function of mass (mAh/g) on the top horizontal axis, and as a function of electrode surface area (mAh/cm^2) on the bottom horizontal axis. The first cycle discharge shows little evidence of a voltage plateau. However, the first cycle charge indicates the two characteristic plateaus of Cu_6Sn_5 at 0.6V and 0.8V. Cycles 2 and 20 charge and discharge profiles indicate the characteristic voltage

plateaus of Cu_6Sn_5. By the 40th cycle, the 0.4V discharge plateau is not evident in Figure 3.4 and the corresponding 0.8V charge plateau is very small. The loss of capacity from the first to the second cycle is significant, but comparable to other reported copper-tin 3-dimensional electrode systems.[3] Some groups have ascribed the initial capacity loss of tin electrodes to electrolyte decomposition, where the by-products coat the tin particles and prevent subsequent access by lithium.[3, 20]

Figure 3.5 shows the electrode capacity normalized to area as a function of cycle number and C-Rate. Figure 3.5 (A) shows the initial capacity loss during the C/15 and C/10 rates for cycles 1-7. The initial Cycles 15-22 show good capacity retention for the C/5 rate. Extended cycling at C/10 for cycles 23-160 shows a gradual decline in capacity. Reasons generally attributed to copper-tin electrode capacity loss include structural degradation of the electrode, the inability of copper to be re-alloyed with tin, formation of lithium oxides from copper and tin oxides present in the electrode, and the formation of a solid electrolyte interphase.[10] While the electrolyte decomposition likely accounts for the initial capacity loss, a combination of other factors might cause the gradual capacity fade. In future studies, a scanning electron and EDS mapping analysis may provide insight into the contributing factors.

To analyze the battery capacity as a function of discharge rate, a cycling regime of a C/10, C/5, C/2 and 1C was performed after the first 160 cycles. As seen in Figure 3.6, the capacity decreases to 27.5% from the C/10 to 1C discharge rate. This decrease in capacity at higher discharge rates is larger than desired. One possible cause is the lack of a homogeneous plating product as seen in the EDX map in Figure 3.3. A multi-phase material with numerous grain boundaries is expected to increase the electrical resistivity and consequently decrease

electrode high rate performance. To explore the possibility of achieving a higher quality copper-tin electrode, a non-contact tin immersion plating technique was investigated.

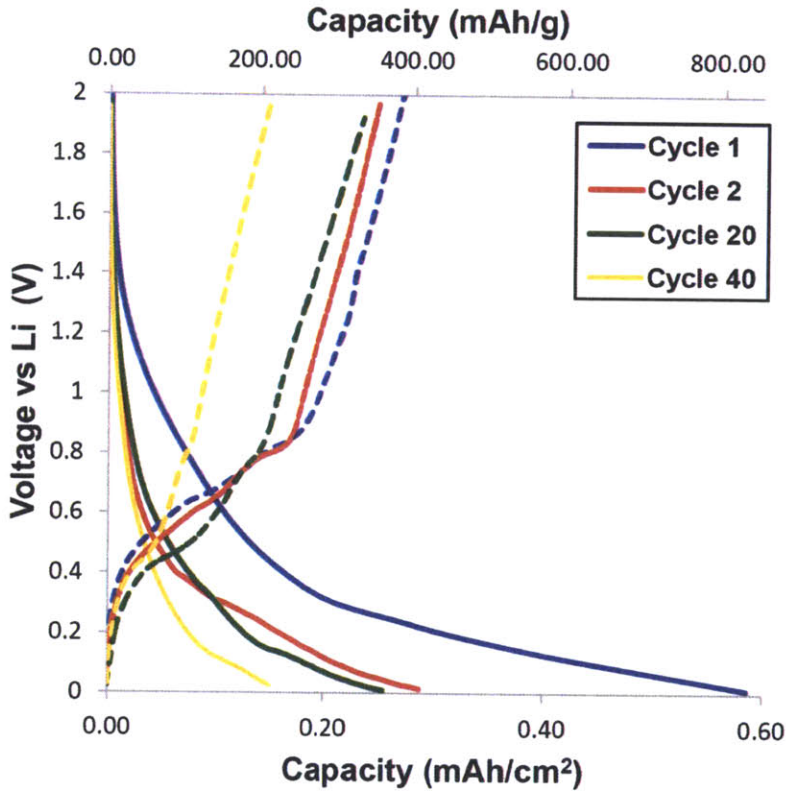

Figure 3.4. Contact immersion copper-tin electrode charge-discharge profiles. Galvanostatic charge and discharge profiles are shown with dashed and solid lines respectively. Cycle 1 is shown in blue, cycle 2 in red, cycle 20 in green and cycle 40 in yellow. Electrode capacity is normalized to mass on the top horizontal scale (mAh/g) and to electrode area on the bottom scale (mAh/cm^2). A large capacity loss is observed after the first discharge with a more gradual capacity loss after the second cycle. A current of 8.5μA was used.

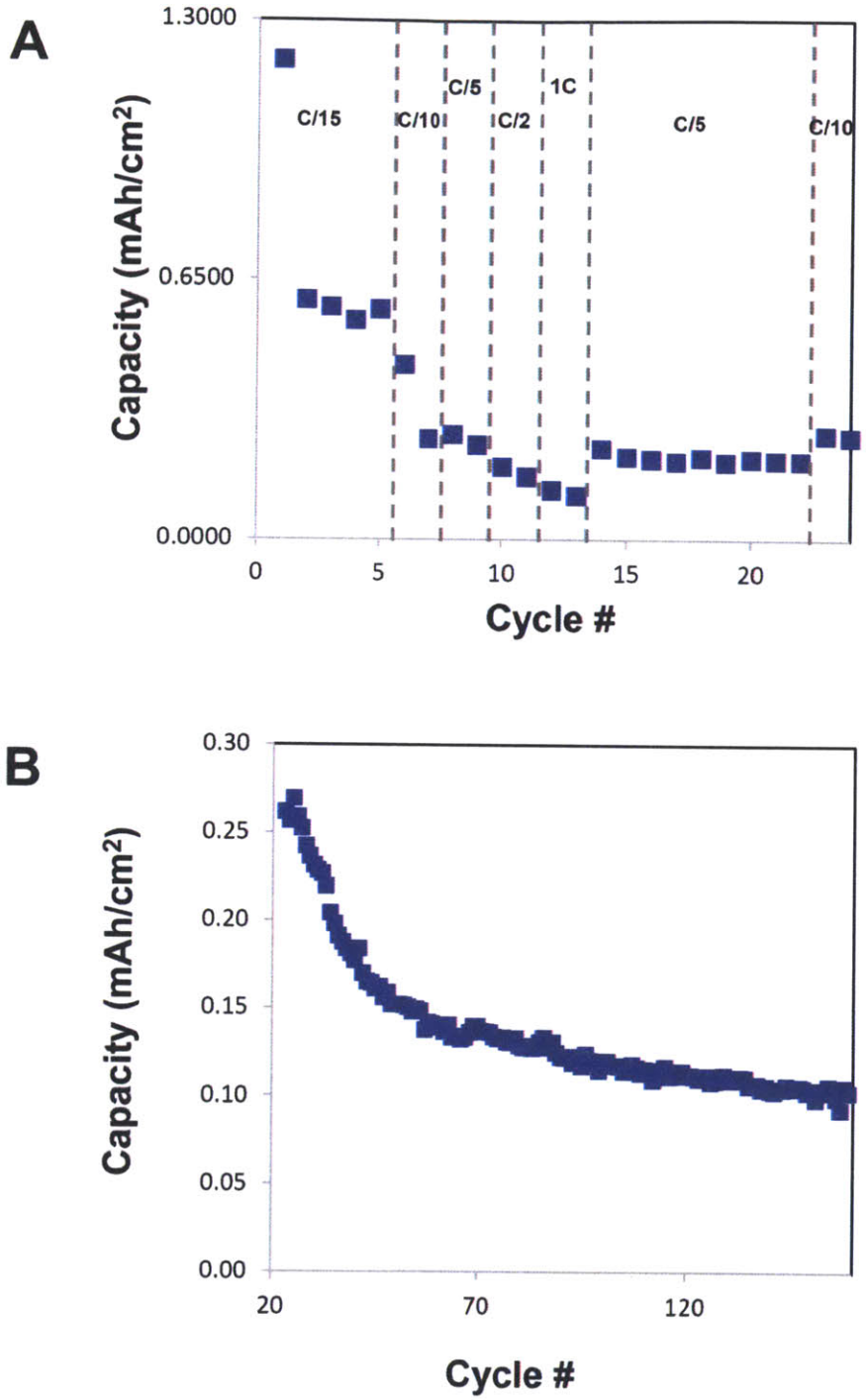

Figure 3.5. Contact immersion copper-tin electrode capacity as a function of cycle number. Capacity values are normalized to electrode surface area (mAh/cm^2). A) Capacity for cycles 1-24 at the C-rates indicated on the plot. A significant capacity loss is observed after the first cycle. B) Capacity for cycles 23 through 160 at a current of 8.5μA.

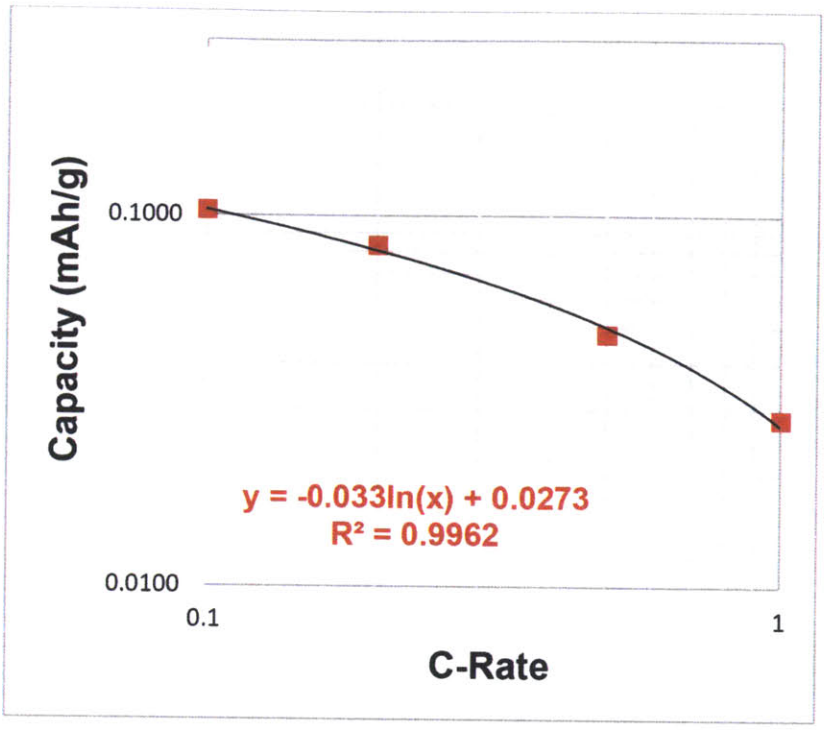

Figure 3.6. Contact immersion plating copper-tin electrode capacity as a function of C-rate. At cycle 160, C/10, C/5, C/2, and 1C charge/discharge cycles were conducted. Capacities normalized to area (mAh/cm^2) are plotted as function of C-rate. A logarithmic fit of capacity versus C-rate is shown. Electrodes maintain 27.5% capacity when increasing the current rate from C/10 to 1C.

3.3.3 Low pH tin immersion plating.

A low pH tin immersion solution was modified from work by Zhao, et al in order to gain better control over the copper-tin nanowires than was seen in the contact immersion method.[14] The tin immersion solution consists of 0.129M tin (II) methansulfonate, 0.756M sodium hypophosphite monohydrate, 1.05M thiourea (Tu), and 0.789M methane sulfonic acid. The expected mechanism is the dissolution of copper and the deposition of tin. The complexation of the resulting copper ions with thiourea to form $[CuTu_4]^+$ makes the displacement reaction thermodynamically favorable. The immersion solution contains hypophosphite, a reducing agent. However, previous studies have included hypophosphite as a bath stabilizing agent and

was not believed to serve as a reducing agent in electroless deposition.[12,21] Zhao, et al hypothesize that once the Cu_6Sn_5 alloy forms on the surface, hypophosphite begins to reduce stannous ions on the plating surface. This mechanism might produce the multi-phase structure hypothesized in Figure 3.1.

Copper nanowire films used for the low pH immersion solution were synthesized using the same method as for the contact immersion study in Section 3.3.1. Copper films were exposed for 5, 10, 15, 30, and 45 minutes in a static tin immersion solution. The plating reaction was quenched by transferring samples to deionized water. Once the excess plating solution was rinsed out of the films, samples were blown dry with nitrogen gas and allowed to complete drying at ambient temperature. For 5 and 10 minutes of immersion, samples presented a pale copper-silver color. At the longer times of 30 and 45minutes of immersion the samples appeared completed converted to silver color.

Sample morphology and material composition was examined using a scanning electron microscope. The nanowire morphologies of samples at 0, 15, 30 and 45 minutes are shown in Figure 3.7. Before immersion, copper nanowires are contiguous with a slightly rough surface. After 15 minutes in the low pH tin immersion solution, nanowires appear to increase the surface roughness and discontinuities are seen in some nanowires. This may be due to dissolution of copper with uneven plating of tin in its place. After 45 minutes of exposure, the nanowire morphology completely changed from distinct nanowires to a porous aggregation of nanoparticles. Energy dispersive X-ray spectra were acquired to determine the relative mass of copper, tin and oxygen. The mass composition of the samples is shown in Table 3.1. The relative mass of copper is observed to decrease from nearly 100% to 0% by 45 minutes of exposure in the tin immersion solution. Correspondingly, tin composition increases from 0% to

over 80% in the same time. Interestingly there is no copper remaining after 45 minutes in the immersion solution and carbon is detected in the EDS spectrum, possibly due to the exposed phage template within the nanowire cores. The oxide content is also seen to increase with time to nearly 10% by 45 mintues.

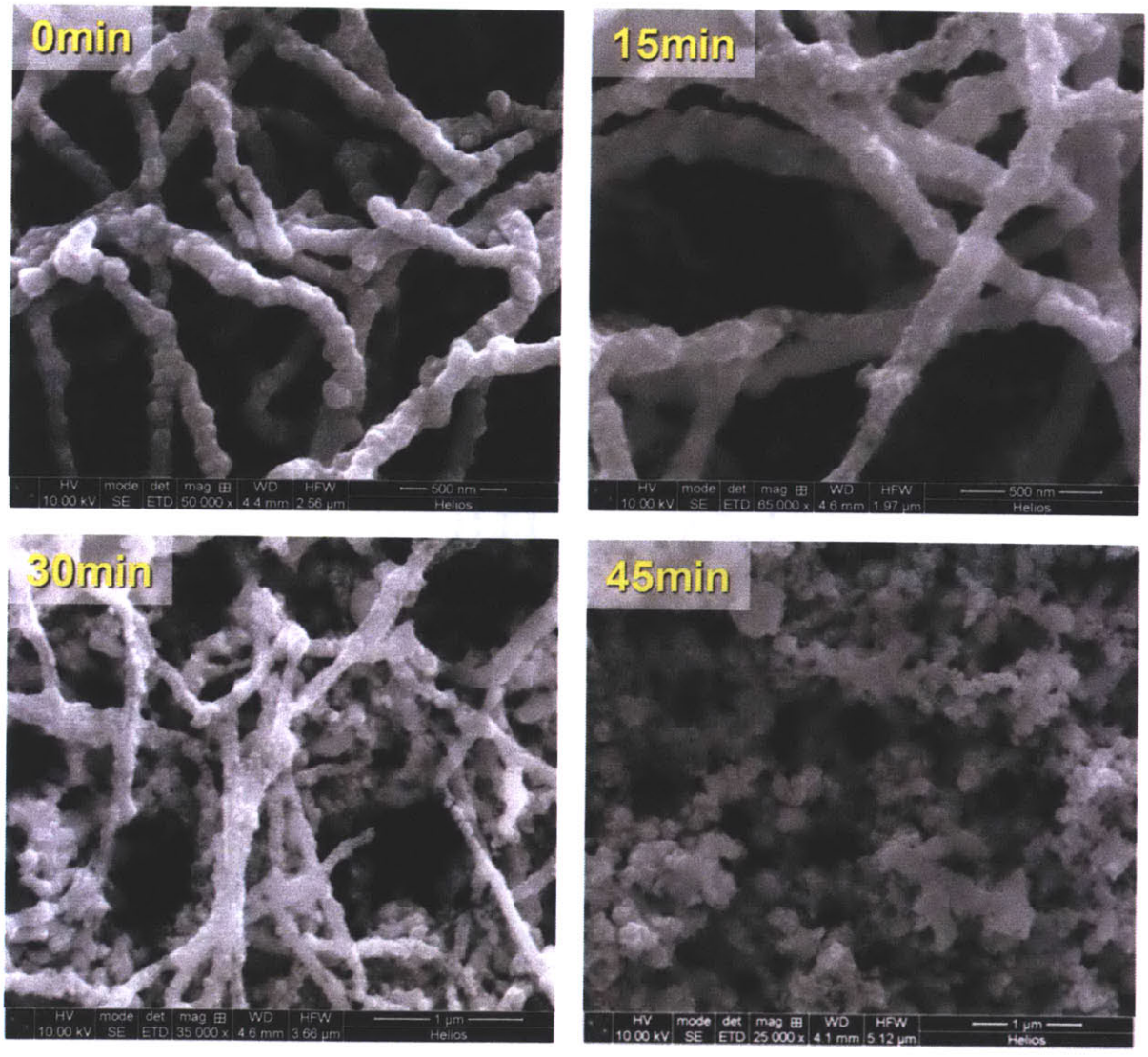

Figure 3.7. Electron microscope images of copper-tin nanowires. Copper nanowires were imaged as a function of time exposure to the tin immersion solution at time points of 0, 15, 30 and 45 minutes. Copper nanowires progress from contiguous nanowire structures to aggregated, porous nanoparticles.

Table 3.1 Mass composition of low pH immersion samples determined by EDS

Immersion Time (min)	Cu (%)	Sn (%)	O (%)	C (%)
0	99.13	0	0.87	0
5	91.87	2.81	2.31	0
10	81.51	12.13	5.81	0
15	58.12	33.56	7.85	0
30	7.386	87.28	5.33	0
45	0	84.87	8.90	3.12

To determine the material phase composition of the resulting nanowires, X-ray diffractometry was performed. The XRD spectra are presented in Figure 3.8 with the time sequence progressing from the top to the bottom of the figure. The symbols used and Powder Diffraction File (PDF) reference cards matched to the peaks designated in Figure 3.8 are shown in Table 3.2. The sequence of XRD spectra indicate a progression from nearly pure copper at time = 0 to a predominantly Cu_6Sn_5 and Sn mixed phase material by 45 minutes. The disappearance of copper over time is most evident in the reduction of the 50.5° copper peak. The evolution of pure tin is seen in the peaks at 62.6° and 63.9° which are clearly present by 30 minutes. Mixed alloy $Cu_{6.25}Sn_5$ and Cu_6Sn_5 peaks are emerge at the 5 minute time point. The Cu_6Sn_5 peaks at 35.0° and 56.5°, which do not overlap any other peaks, increase until 15 minutes and then decrease in peak height as time continues to 45 minutes. During the same time frame the convoluted pure tin and copper-tin alloy peaks increase. Copper oxide peaks resolve to a more narrow peak width at 36.5° by 15 minutes and then disappear by 45 minutes. The time evolution of XRD spectra suggests a progression of material phase composition shown on the right margin of Figure 3.1.

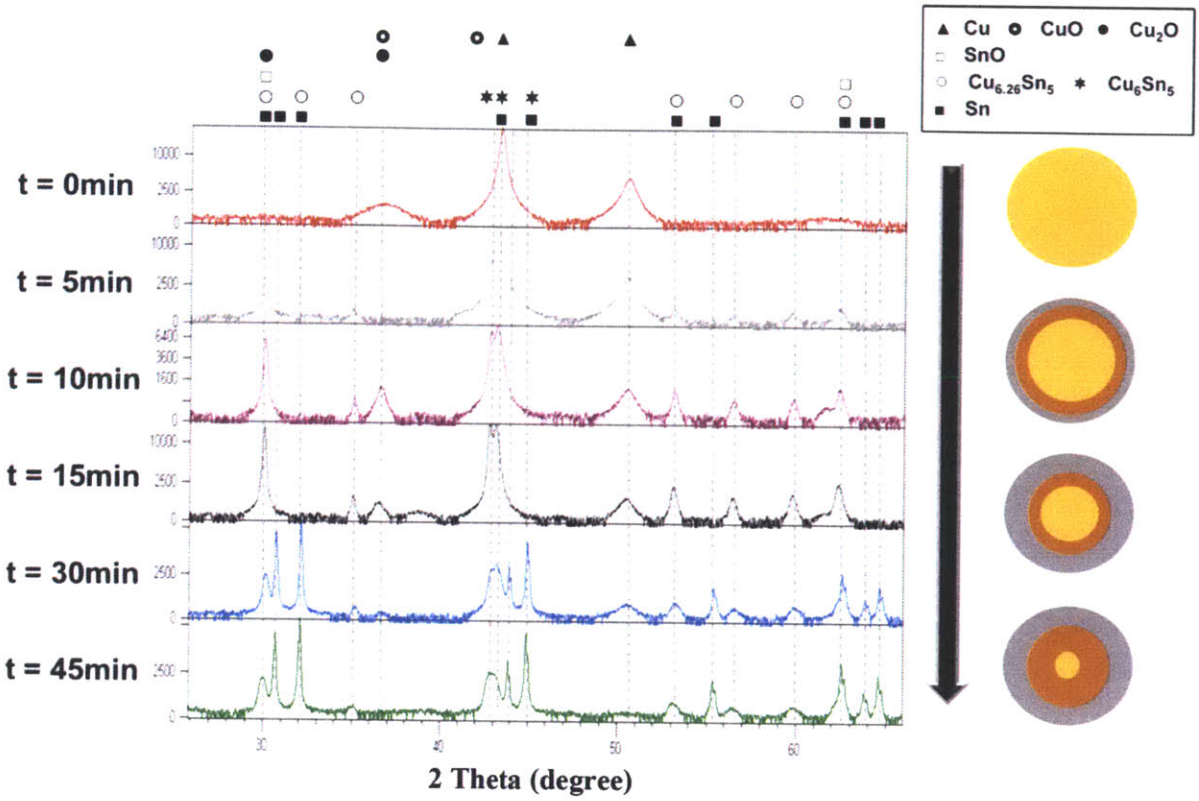

Figure 3.8. XRD spectra of copper-tin immersion plating electrodes. XRD spectra from 25° to 65° are shown as a function of tin immersion time. The 3-dimensional copper electrodes at time = 0 are shown in the top spectrum (red). Peak labels are identified in the upper right legend and correspond to dashed lines down the spectra to identify changes over time. Copper peaks are observed to decrease with immersion time, while Sn and $Cu_{6.26}Sn_5/Cu_6Sn_5$ increase with time. Copper oxides resolve to more narrow peaks by t=10min and then diminish by t = 45 min. Tin oxide peaks increase over time. The nanowire cross-sections to the right show a hypothetical spatial distribution of phases with the progression of time.

Table 3.2 XRD Reference Card Numbers

Phase	Reference Card	Symbol in Figure 3.8
Cu	04-014-0265	▲
Sn	04-006-2820	■
Cu_6Sn_5	00-045-1488	✱
$Cu_{6.25}Sn_5$	00-047-1575	○
Cu_2O	04-012-6327	●
CuO	01-078-0428	⊙
SnO	04-008-7671	□

To determine the effect of material composition and nanowire morphology on electrode performance, copper nanowire films exposed to the low pH tin immersion solution for 10, 15, and 30 minutes were assembled into coin cells using the same configuration as for the contact immersion battery in Section 3.3.1. Active material mass was determined from the EDS spectra in Table 3.1 and C/10 rates determined using a theoretical capacity of 800mAh/g. Cells were cycled at the C/10 rate and the discharge profiles for the 10, 15 and 30 minute samples were plotted for cycles 1, 2, 20, and 40 as shown in Figure 3.9. To better resolve the voltage plateaus of the Figure 3.9 profiles, the change in capacity per change in voltage, dQ/dV is plotted versus voltage versus lithium in Figure 3.10. All samples experience a significant capacity reduction after the first cycle, likely attributable to electrolyte decomposition as previously discussed.

The charging profiles in Figure 3.9 all indicate the characteristic 0.6V and 0.8V plateaus for Cu_6Sn_5. These plateaus are also revealed in the dQ/dV plot in Figure 3.10. The discharge plateaus and dQ/dV plots also indicate the characteristic voltage plateaus of Cu_6Sn_5, however, the 0.4V plateau becomes less distinct as cycling progresses. When considering the other mechanisms that result in copper-tin anode capacity fade, this suggests the possible isolation of copper with increasing cycles. Isolated regions of copper would be unable to re-alloy with tin during discharge, resulting in tin that remains lithiated. This effect would manifest itself with an incrementally decreased capacity with each cycle.

The capacity normalized to electrode surface area is plotted versus cycle number in Figure 3.11. The 10 minute sample is seen to have a stable capacity through 65 cycles. The 15min sample maintains a higher capacity than the other samples to 20 cycles and then rapidly deceases with further cycling. The 30 minute sample shows a steady capacity fade until battery failure at the 23rd cycle. Electrode capacity as a function of C-Rate was determined with a

C/10, C/5, C/2, and 1C cycle implemented after capacity stabilization. This was performed after 65 cycles for the 10 minute sample and after 35 cycles for the 15 minute sample. The rate performance was not performed for the 30 minute sample. The capacity versus C-rate performance is shown in Figure 3.12. Both cells maintain approximately 30% of the C/10 capacity when the rate increases to 1C.

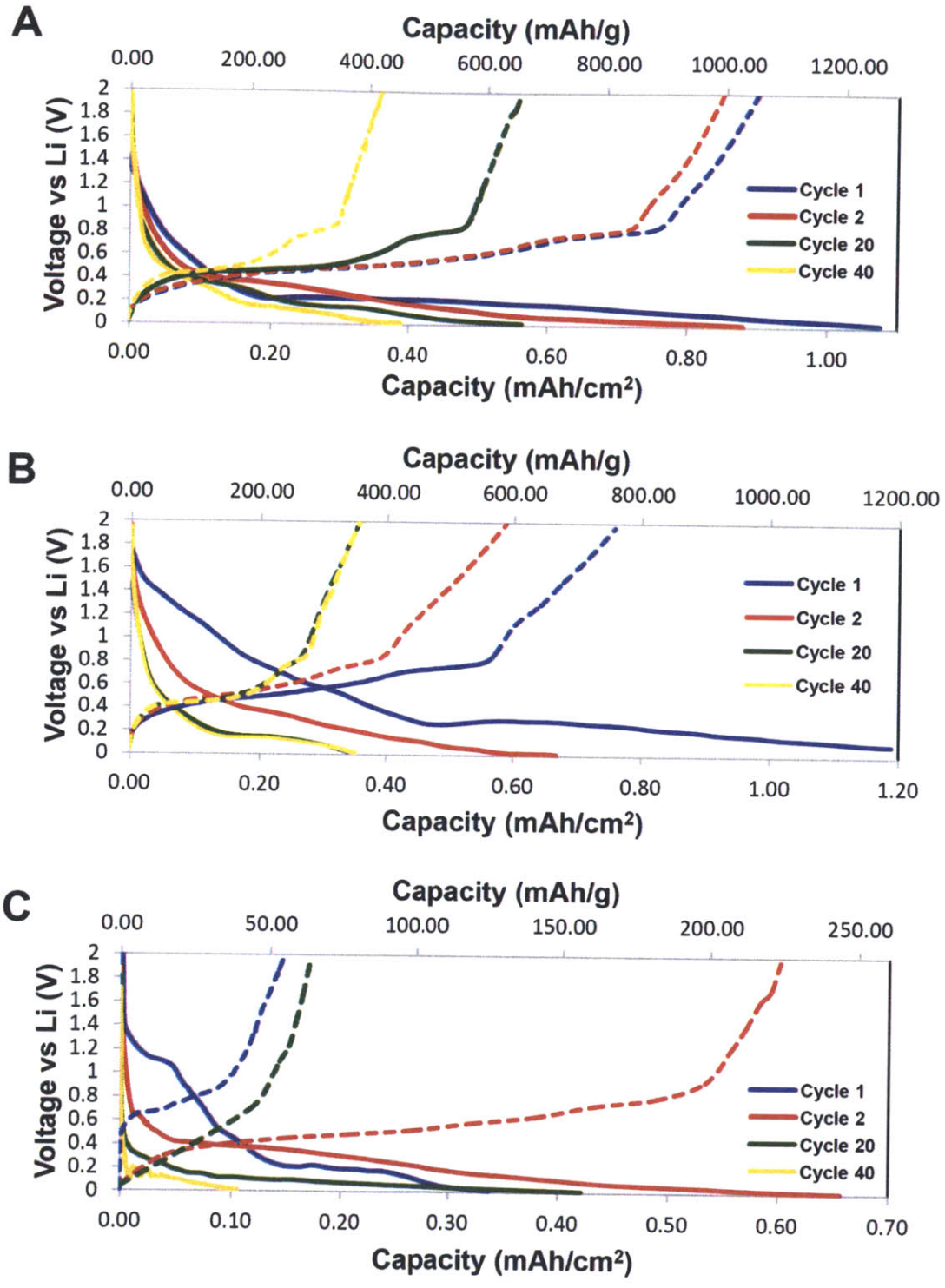

Figure 3.9. Tin immersion copper-tin electrode galvanostatic charge-discharge profiles. Tin immersion solution times are A) 10 minutes, B) 15 minutes, and C) 30minutes. Cycle numbers are indicated by color: cycle 1 – blue, cycle 2 – red, cycle 20 – green, and cycle 40 – green. C/10 current rates were used for all profiles with the exception of C) cycle 1 which was run at C/5.

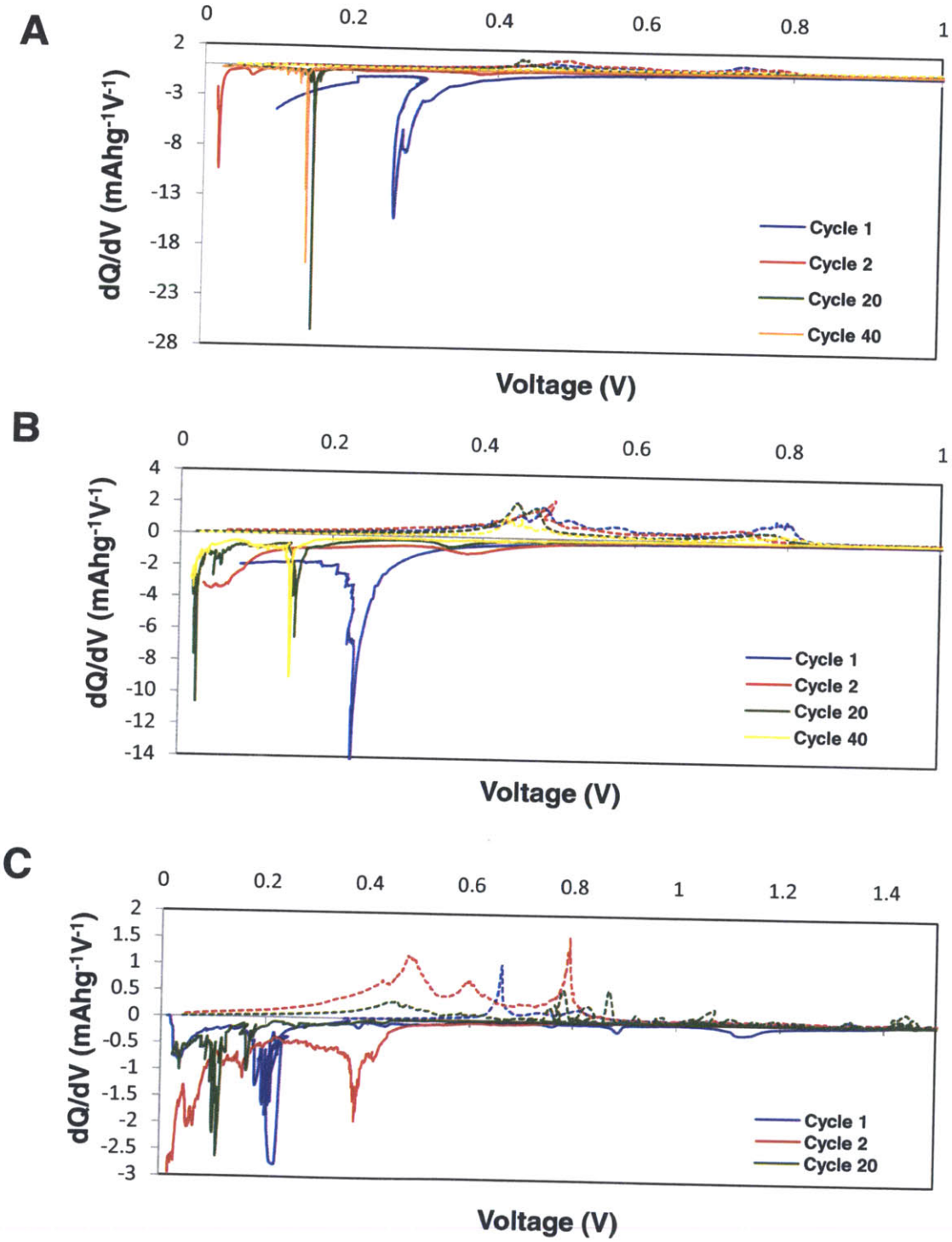

Figure 3.10. Tin immersion copper-tin electrodes, dV/dQ versus Voltage. Tin immersion solution times are A) 10 minutes, B) 15 minutes, and C) 30minutes. Cycle numbers are indicated by color: cycle 1 – blue, cycle 2 – red, cycle 20 – green, and cycle 40 – green. C/10 current rates were used for all profiles with the exception of C) cycle 1 which was run at C/5.

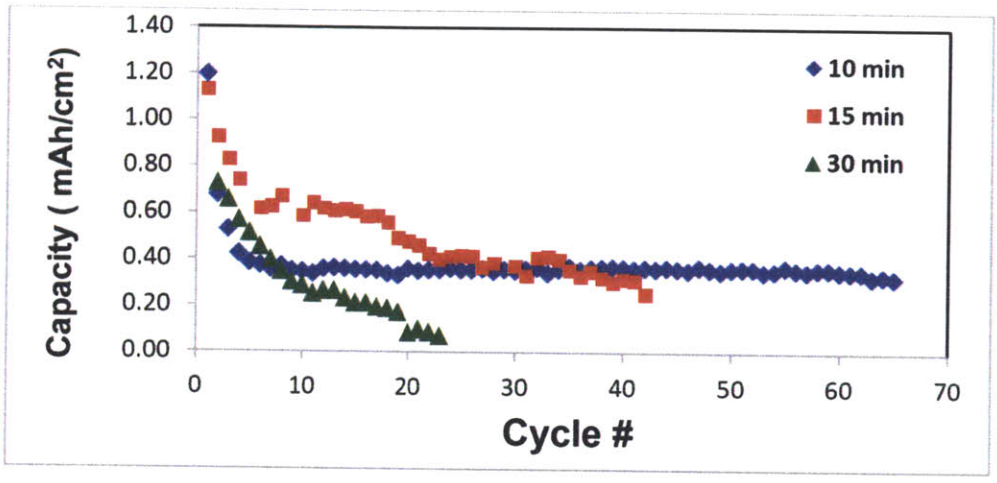

Figure 3.11. Tin immersion electrode Capacities versus Cycle #. Electrode capacities normalized to area (mAh/cm^2) are plotted as a function of cycle # for C/10 charge-discharge rates. Immersion times in tin plating solution are 10 minutes (blue), 15 minutes (red) and 30 minutes (green). After initial capacity loss, the 10 minute immersion time electrode exhibits stable capacity out to 65 cycles. The 15 minute immersion time electrode exhibits the highest capacity for 30 cycles and then declines. The 30 minute immersion time electrode decreases in capacity and then fails to function beyond 23 cycles.

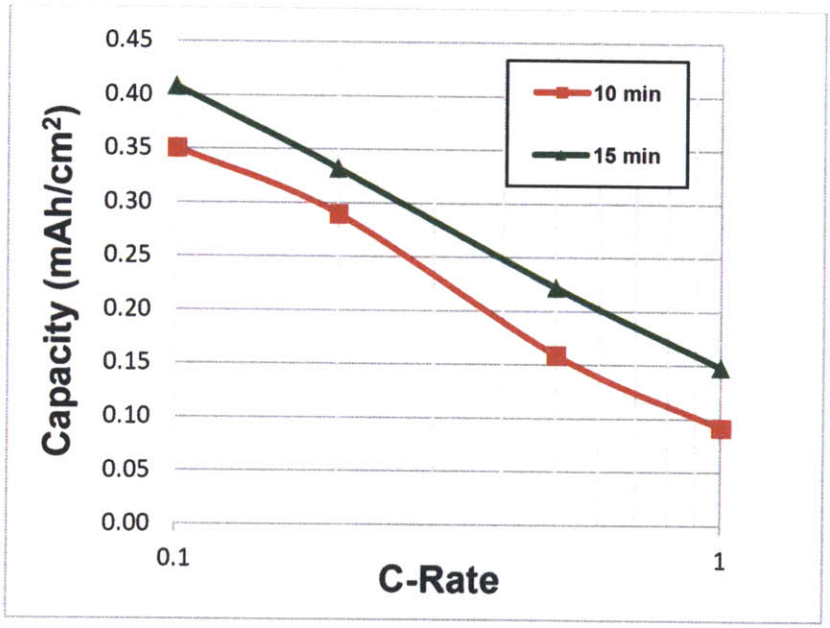

Figure 3.12. Capacity versus C-Rate for tin immersion electrodes. The 10 (red) and 15 (green) minute low pH tin immersion samples were tested for capacity as a function of C/10, C/5, C/2 and 1C discharge rates.

When considering post immersion treatment nanowire morphology seen in Figure 3.7, the more stable performance of the 10 minute sample seems attributable to less structural compromise of the nanowires at shorter exposure times. In an attempt to minimize structural compromise and at the same time maximize the mass of copper to displacement, nanowire films were exposed to the low pH tin immersion solution with constant stirring at 140rpm for 5 minutes. Whereas the static immersion for 5 minutes resulted in a faint color change to the copper film, 5 minutes of exposure with stirring resulted in a complete conversion to silver-tin color. The 5 minute sample with stirring was examined with a scanning electron microscope and an energy dispersive X-ray map acquired. The morphology of the nanowires is shown in Figure 3.13. The original copper nanowire structure appears to be preserved. Also seen are areas of high contrast electron density of nanoparticles decorating the original structure. These nanowire surface nanoparticles have not been previously observed in any pure copper nanowire synthesis and are believed to directly result from the tin immersion exposure.

The EDS map and spectrum of the 5 minute with stirring sample are shown in Figure 3.14. The Cu:Sn mass ratio was determined to be 62.5:37.5. Oxygen was not observed in the EDS spectrum. The 37.5% tin mass composition is comparable to the 15 minute immersion exposure without stirring. The EDS map reveals a fairly even distribution of both copper and tin, with the EDS Sn map in Figure 3.14 (C) indicating a slight tin concentration that corresponds to the nanoparticles observed in the SEM image in Figure 3.13.

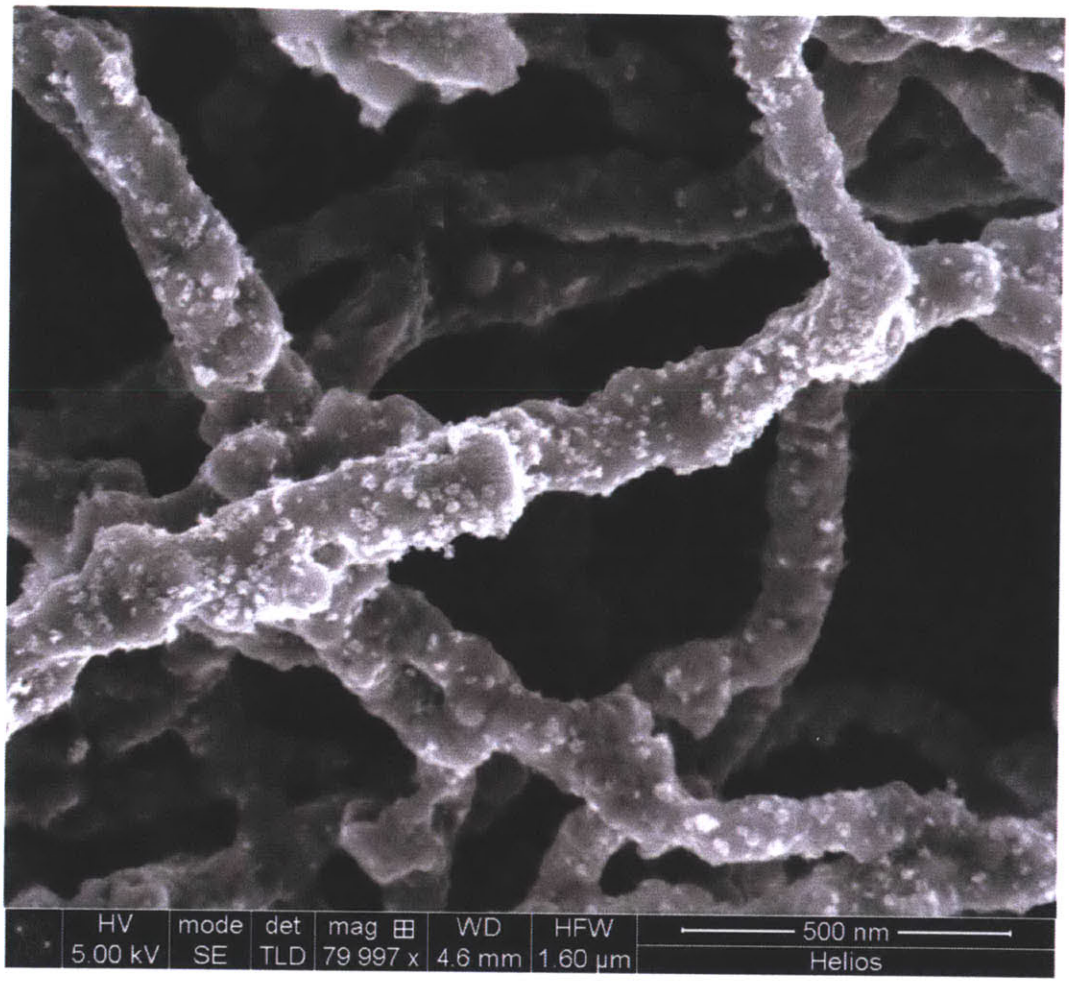

Figure 3.13. SEM image of low pH, 5 minute immersion sample with stirring. The low time immersion exposure time with stirring appears to preserve the structural integrity of the original copper nanowires. High contrast secondary electron density is seen in nanoparticles that decorate the nanowires.

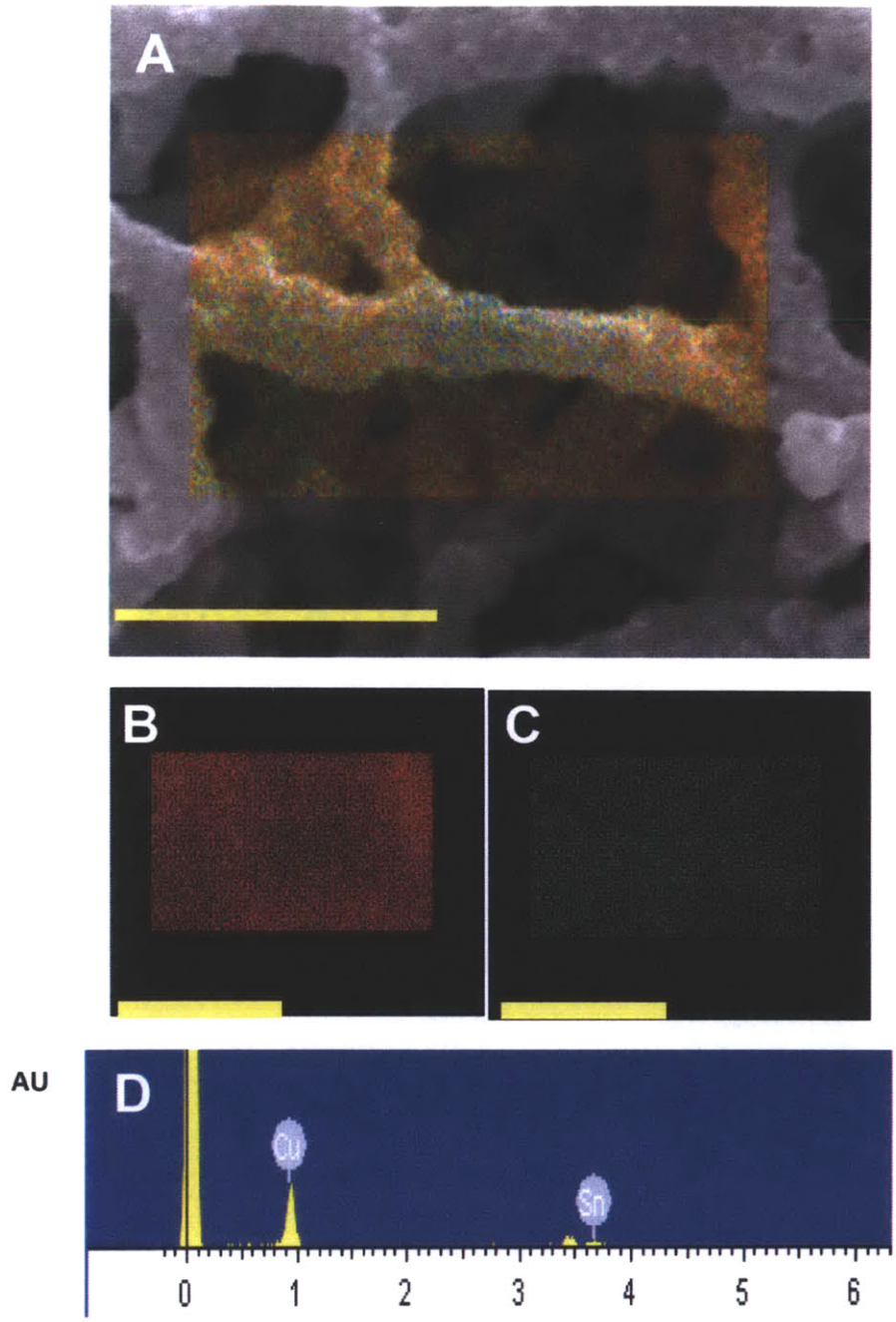

Figure 3.14. Energy dispersive X-ray mapping of 5 minute, low pH immersion sample with stirring. A) EDS composite map. B) EDS copper distribution. C) EDS Sn distribution. D) EDS spectra. Mass ratio Cu:Sn is 62.5:37.5. Scale bars are 7μm.

The 5 minute low pH tin immersion with stirring sample was assembled in a coin cell and tested at a C/10 rate as done for previous samples. The C/10 charge-discharge profiles and corresponding dQ/dV plots for the cycles 1, 2, and 20 are shown in Figure 3.15. The characteristic voltage plateaus for Cu_6Sn_5 are observed as in the case of the non-stirred tin immersion samples. The C/10 capacity versus cycle number shown in Figure 3.16 is similar to the cycling of the 10 minute tin immersion exposure sample seen in Figure 3.11. While a gradual capacity fade is observed in the 10 minute tin exposure and 5 minute stirred samples, with similar resulting copper-tin mass ratios, the five minute stirred sample is able to perform for a greater number of cycles. Capacity as a function of C-rate was determined with C/10, C/5, C/2, and 1C discharges conducted after the 22d cycle. Although the sample maintained better cycling performance compared to the non-stirred 10 minute immersion sample, the 5 minute stirred immersion sample preserves only approximately 10% of the C/10 capacity at the 1C rate. It is undetermined at this time why the biotemplated copper-tin anodes lose a significant capacity at higher discharge rates. Further optimization of the rate performance will add to the impressive capacity per square area and cycling performance of the 3-dimensional virus-templated electrodes.

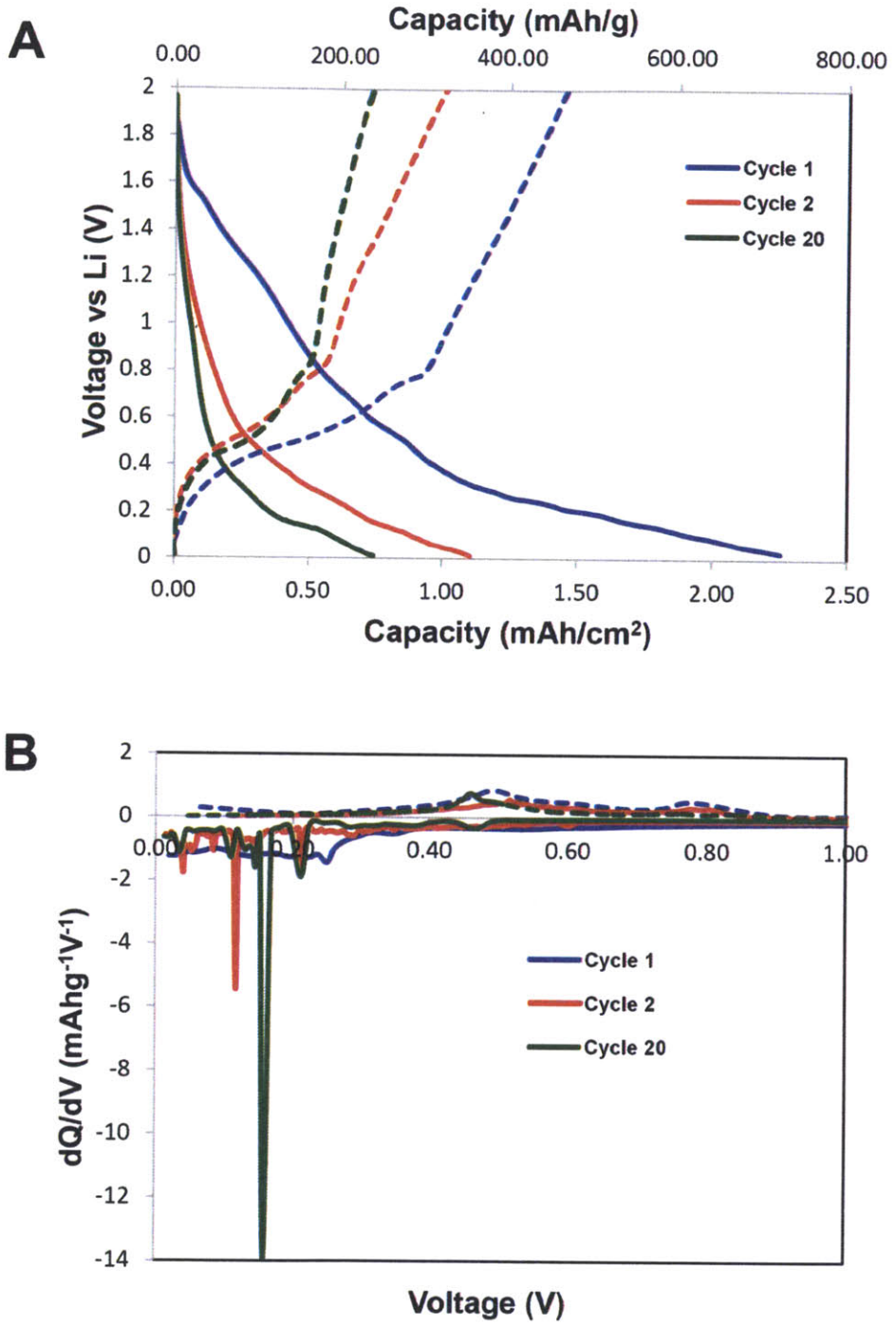

Figure 3.15. Tin immersion plating, 5 minutes with stirring, charge-discharge profiles. A) Charge-discharge profiles at C/10 rate (12μA). Plot colors are: cycle 1 – blue, cycle 2 – red, and cycle 20 – green. B) dQ/dV ($mAhg^{-1}V^{-1}$) versus Voltage (V). Discharge profiles plotted with negative dQ/dV values indicate peaks at approximately 0.2V. Charge profiles plotted with positive dQ/dQ values indicate peaks at approximately 0.4-0.5V and 0.8V.

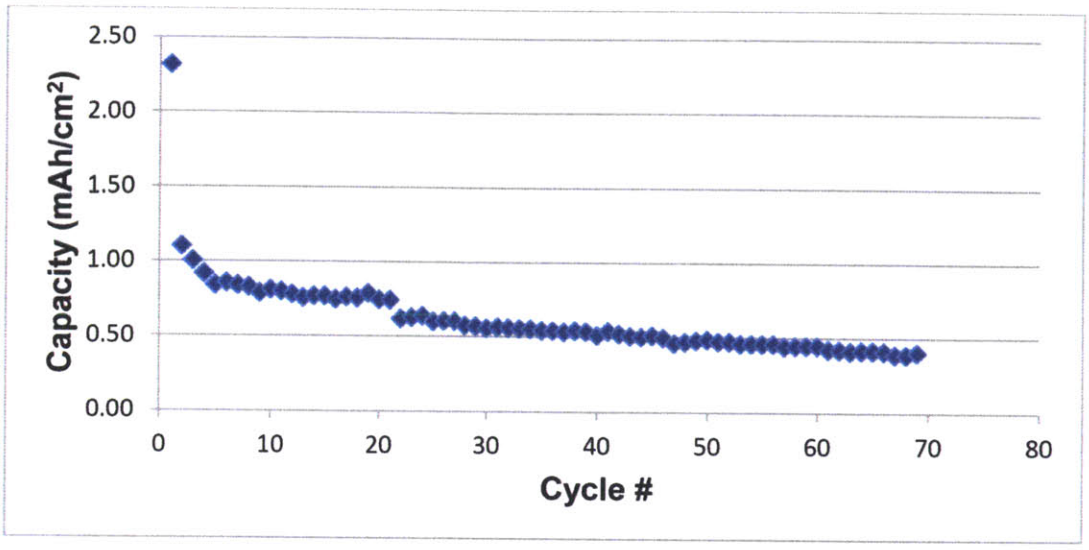

Figure 3.16. C/10 Capacity (mAh/g) versus Cycle # for tin immersion copper-tin electrode, 5 minutes with stirring. The copper-tin electrode exhibits a significant capacity decrease during the first five cycles and then stabilizes at approximately 0.75mAh/cm^2 through cycle 22. A gradual capacity fade is observed through C/10 cycle 70.

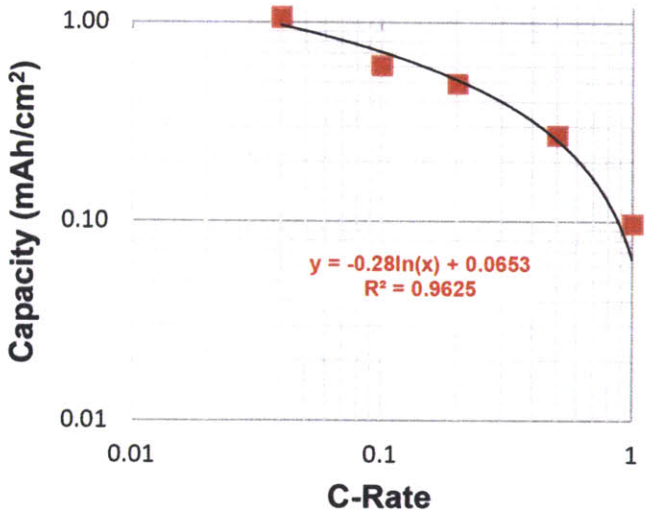

Figure 3.17. Capacity (mAh/g) versus C-rate for tin immersion copper-tin electrode, 5 minutes with stirring. The copper-tin electrode maintains approximately 10% of capacity when the charge rate increases from C/10 to 1C. The logarithmic relationship between capacity and C-rate is shown above.

3.4 Conclusions

Three-dimensional copper nanowire films exposed to tin immersion plating solutions for short periods of time demonstrated stable capacity performance using only solution based chemistry to synthesize redox active material on a virus hydrogel biotemplate. No additional processing steps such a thermal annealing were performed, making this synthesis route an inexpensive means to achieving a high capacity per surface area anode materials. Further, no additional conductive materials or organic binders were used to assemble the electrodes. As synthesized, the copper-tin electrodes are free standing films and represent a significant advance in the direction of light-weight electrode materials.

The low exposure time galvanic displacement of 3-dimensional copper nanowire scaffolds led to a mixed phase copper-tin material and resulted in stable battery capacity approaching 100 cycles. The porous structure of the starting copper nanowire scaffold provides roughly 50% void volume to accommodate the nearly three-fold volumetric expansion of tin during lithium battery discharge. This void volume to volumetric expansion scaling should allow for a tin-based active material thickness that is 1/6 the pore geometry. The open pore network of the 3-dimensional copper films should also allow for a number of other deposition techniques of tin or other battery active materials. These techniques include atomic layer deposition (ALD), chemical vapor deposition (CVD) and electrodeposition. These techniques may provide additional means to greater control over active material thickness and phase composition, while at the same time preserving the structural integrity of the 3-dimensional conductive copper mesh.

3.5 References

1. Winter, M. & Besenhard, J.O. Electrochemical lithiation of tin and tin-based intermetallics and composites. *Electrochimica Acta* **45**, 31-50 (1999).
2. Ren, J.G. et al. Nanometer copper-tin alloy anode material for lithium-ion batteries. *Electrochimica Acta* **52**, 2447-2452 (2007).
3. Bazin, L. et al. High rate capability pure Sn-based nano-architectured electrode assembly for rechargeable lithium batteries. *Journal of Power Sources* **188**, 578-582 (2009).
4. Li, N.C., Martin, C.R. & Scrosati, B. Nanomaterial-based Li-ion battery electrodes. *Journal of Power Sources* **97-8**, 240-243 (2001).
5. Wachtler, M., Besenhard, J.O. & Winter, M. Tin and tin-based intermetallics as new anode materials for lithium-ion cells. *Journal of Power Sources* **94**, 189-193 (2001).
6. Tamura, N. et al. Study on the anode behavior of Sn and Sn-Cu alloy thin-film electrodes. *Journal of Power Sources* **107**, 48-55 (2002).
7. Long, J.W., Dunn, B., Rolison, D.R. & White, H.S. Three-dimensional battery architectures. *Chemical Reviews* **104**, 4463-4492 (2004).
8. Chen, X.L. et al. Virus-Enabled Silicon Anode for Lithium-Ion Batteries. *Acs Nano* **4**, 5366-5372 (2010).
9. Royston, E., Ghosh, A., Kofinas, P., Harris, M.T. & Culver, J.N. Self-assembly of virus-structured high surface area nanomaterials and their application as battery electrodes. *Langmuir* **24**, 906-912 (2008).
10. Shin, H.C. & Liu, M.L. Three-dimensional porous copper-tin alloy electrodes for rechargeable lithium batteries. *Advanced Functional Materials* **15**, 582-586 (2005).
11. Barker, B.D. Electroless Deposition of Metals. *Surface Technology* **12**, 77-88 (1981).
12. Huttunen-Saarivirta, E. Observations on the uniformity of immersion tin coatings on copper. *Surface & Coatings Technology* **160**, 288-294 (2002).
13. Molenaar, A. & Coumans, J.J.C. Autocatalytic Tin Deposition. *Surface Technology* **16**, 265-275 (1982).
14. Zhao, J., Li, N., Cui, G.F. & Zhao, J.W. Study on immersion tin process by electrochemical methods and molecular orbital theory. *Journal of the Electrochemical Society* **153**, C848-C853 (2006).
15. DjokiÄ‡, S.S., Conway, B.E. & White, R.E. in, Vol. 35 51-133 (Springer US, 2002).
16. Rasband, W.S. ImageJ, U. S. National Institutes of Health, Bethesda, Maryland, USA. (1997-2005).
17. Chiang, C.Y. et al. Weaving genetically engineered functionality into mechanically robust virus fibers. *Advanced Materials* **19**, 826-+ (2007).
18. Yoo, P.J. et al. Spontaneous assembly of viruses on multilayered polymer surfaces. *Nature Materials* **5**, 234-240 (2006).
19. Kepler, K.D., Vaughey, J.T. & Thackeray, M.M. Copper-tin anodes for rechargeable lithium batteries: an example of the matrix effect in an intermetallic system. *Journal of Power Sources* **81**, 383-387 (1999).
20. Beattie, S.D., Hatchard, T., Bonakdarpour, A., Hewitt, K.C. & Dahn, J.R. Anomalous, high-voltage irreversible capacity in tin electrodes for lithium batteries. *Journal of the Electrochemical Society* **150**, A701-A705 (2003).

21. Koyano, H., Kato, M. & Uchida, M. Electroless Tin Plating through Disproportionation. *Plating and Surface Finishing* **78**, 68-& (1991).

CHAPTER 4

Mechanical Properties of Phage-Templated 3-Dimensional Scaffolds

4.1 Introduction

The assembly of nanoscale components to create materials with novel binding, catalytic, electronic, optical and mechanical properties has been at the forefront of current materials research. Hydrogels, aerogels and inorganic porous scaffolds are some of the classes of materials that are envisioned to benefit from nanoscale ordering with applications ranging from drug delivery, sensors, electronics, catalysis, and energy absorption. Hydrogels are highly networked polymer organic chains that can possess water content up to 99% (Matzelle, 2008). Aerogels (or xerogels) are the solid form of gels that offer a high surface area and small pore size. Metal pore networks are often created via metal foam synthesis and provide high surface area, electrical conductivity and mechanical strength (Ashby, 2000).

Biomaterials offer a route to synthesizing various classes of porous materials. Hydrogels formed from biopolymers such as DNA and virus particles have been reported. Biotemplating inorganic materials on biological scaffolds offers a means to order materials at the nanoscale onto an organic scaffold (Xu, 2006). The ability of individual protein subunits to nucleate specific materials and crystal structures has been demonstrated for numerous biological templates (Fan, 2009). Specifically, the M13 bacteriophage and tobacco mosaic virus have been used as templates to synthesize a variety of metal and metal oxide material (Peele, 2005).

One of the challenges of the biotemplating approach is to create higher order porous structures with either periodic or stochastic arrangements of a repeating structural element. Some successful examples are DNA tiles using assembled from designed sequences to form Holliday junctions (Lin, 2006). Such periodic DNA 2-dimensional arrays have also been functionalized with gold nanoparticles. The M13 virus has been chemically cross-linked to form phage fibers that subsequently served as a template to nucleate gold nanoparticles. The

mechanical properties of many of these materials will determine the feasibility of incorporating them into real-world applications.

In this work we determine the mechanical properties of a range of bacteriophage based materials to include hydrogels, aerogels, and metal nanowire networks. The stochastic ordering of the M13 bacteriophage via covalent cross-linking into stable hydrogels was demonstrated in Chapters 2 and 3. The hydrogels can subsequently be freeze dried into aerogels or mineralized into copper and nickel metal porous nanowire networks. Further, genetically modified M13 virus can bind single wall carbon nanotubes before gelation to create a composite CNT-biotemplate. Given the novel series of related materials, the purpose of this study is to determine 1) the optimal nanoindentation conditions and analysis model for each sample type, and 2) the elastic modulus of virus-based hydrogels, aerogels and metal nanowire networks to initially characterize the mechanical robustness of these materials for processability and device integration.

4.2 Experimental

4.2.1. Sample Preparation.

Virus clones. The M13 bacteriophage strains used in this work are termed "E3" and "DSPH". The E3 strain has a genetically modified fusion protein on the 2,700 copies of the p8 coat protein that consists of a tetra-carboxylate moiety at the solvent exposed N-terminus. The coat protein charge density can then be controlled via pH (Yoo, 2006). The DSPH strain presents the aromatic proline and histidine amino acids on the terminal p8 fusion creating an affinity for hydrophobic carbon nanotubes.

Glutaraldehyde. Glutaraldheyde is a five carbon chain with aldehyde groups at either end and is a commonly employed protein cross-linking agent (Mignealt, 2004). While the exact mechanism of glutaraldehyde cross-linking remains uncertain, the conventionally accepted idea is that one of the aldehyde groups on glutaraldhyde forms a covalent bond with a lysine residue on one protein target, while the second aldehyde group binds a second protein, effectively cross-linking them. The covalent bonding mechanism is believed to be either an aldol condensation or Michaels – type addition.

Hydrogels. Film hydrogels were prepared with 0.1ml E3 M13 bacteriophage at $1x10^{14}$pfu/ml, buffered in 1x phosphate buffered saline (PBS) on a $1cm^2$ silicon substrate. Substrate sidewalls were formed with parafilm. The silicon-phage assembly was placed upside-down in a stock solution of 50% glutaraldehyde. A phage-glutaraldehyde phase boundary occurs due to the differential specific gravities of the two solutions such that the resulting hydrogel is approximately the same volume as the starting phage solution. After 1.5h of virus cross-linking, the film hydrogel was dialyzed in DI water (18.2Ω) to remove excess glutaraldehyde. The film hydrogel sample was approximately 100μm thick. The DSPH-SWCNT hydrogel was prepared with 0.1ml DSPH M13 bacteriophage at $1x10^{14}$pfu/ml in DI water. DSPH virus was incubated with a 20-fold stoichiometric excess of single wall carbon nanotubes approximately 500nm in length and 0.8nm in diameter in DIW and sodium cholate, 2%(w/w), for 48h. The CNT bound virus was then dialyzed against DI water and cross-linked as above.

Aerogels. DSPH virus at $1x10^{14}$pfu/ml was incubated with a 20-fold excess of single wall carbon nanotubes approximately 500nm in length and 0.8nm in diameter in DIW and sodium

cholate, 2%(w/w), for 48h. The resulting phage suspension was gray in color. 0.1ml of the virus solution was placed in a microfuge tube and 0.1ml of stock 50% glutaraldehyde was pipetted below the virus solution. A distinct phase boundary was observed between the glutaraldehyde and the phage solution with the phage remaining in the top layer based on differences in specific gravity. The cross-linking proceeded for 2h before dialysis with DI water to remove excess glutaraldehyde. The resulting phage-SWCNT aerogel was then supercritically dried to form an aerogel. Some volume decrease was observed. A significant volume decrease (>50%) was observed in previous experiments using critical point drying of the virus hydrogels.

Copper Nanowire Networks. Copper nanowire networks were synthesized by starting with a film bound hydrogel as described above. After dialyzing the gel against DI water, the gel was exposed to 10mM Na_2PdCl_4 (Strem Chemicals, CAS# 13820-53-6) for 2h. Palladium exposure changed the gel color from translucent white to pale brown. The palladium sensitized gel was dialyzed against DI water to remove excess palladium ions. The gel was then exposed to 10mM dimethylamine borane (DMAB) (Alfa Aesar, CAS# 74-94-2) buffered in 25mM 2-(N-morpholino)ethanesulfonic acid (MES) (Research Organics, CAS# 145224-94-8) at pH 7. Reduction of palladium bound the virus gel was evidenced by the gel changing color from pale brown to black. The gel was then immersed in 10ml of a copper electroless deposition (ELD) solution consisting of: 0.032M $CuSO_4 \cdot 5H_2O$ (Mallinckrodt, CAS#4844-02), 0.04M ethylenediaminetetraacetic acid (EDTA) (Mallinckrodt, CAS#6381-92-6), 0.067M DMAB, and 0.1M tris buffered saline (TBS) at pH 7.

Nickel Nanowire "Thick" Film Networks. Nickel nanowire "thick" film networks were prepared as for copper nanowire networks with a change of ELD solutions. The nickel ELD used was: 0.032M $NiSO_4 \cdot 6H_2O$ (Aldrich, CAS#22767-6); 0.04M Glycine (Mallinckrodt, CAS#56-40-6); 0.004M EDTA; 0.067M DMAB; 0.1M MES buffer at pH~7. Films were detached from the underlying substrate with a razor blade and mounted with conductive carbon tape on a SEM stub for cross-sectional imaging. The free standing nickel film was then placed in 0.1ml DI water and dried at 50°C on a silicon chip. The capillary action of drying flattened the nickel film onto the silicon substrate for nanoindentation.

Nickel Nanowire "Thin" Film Networks. Hydrogel films were prepared on silicon substrates with 5µl E3 virus at a concentration of 8.23×10^{13}pfu/ml as described above. Gels were sensitized in 10mM $(NH_3)_4PdCl_2$ (Aldrich, CAS#323438-5G) for 1h and then reduced in 0.1M DMAB, 0.25M MES at pH 6.5 for 1h. The nickel ELD consisted of: 0.0032M NiSO4, 0.002M glycine, 0.002M EDTA, 0.004M MES buffer, 0.0067M DMAB with a pH of 7. Deposition proceeded for 14.5h and 20.5h.

4.2.2. Mechanical Testing.

Atomic Force Microscope Force Spectroscopy. An Asylum Research MFP 3D was used to perform nanoindentation on all samples other than the nickel nanowire thin film networks. A silicon nitride cantilever with a Novascan 20µm borosilicate glass sphere (k_{nom} = ~0.03N/m) was used to indent hydrogel samples. An Asylum AC160TS cantilever, k_{nom} = ~42N/m, tip radius = 9 nm, was used to indent the phage-SWCNT aerogel. A Veeco/Bruker DNISP diamond probe, k = 314N/m, tip radius = 40nm, was used to indent copper and thick nickel samples. Deflection

sensitivities and spring constants of the each indentation probes were calibrated prior to data acquisition.

Instrumented Nanoindentation. Nanoindentation experiments were conducted in ambient conditions using a Hysitron, Inc. Triboindenter. Load-controlled nanoindentations were performed using a 10 μm diamond conical indenter. The maximum loads were set to be 50 and 100 μN and the loading and unloading rate was kept constant, i.e. 10 μN/s. To investigate the time-independent mechanical properties, the unloading rate was varied, i.e., 5, 10, and 20 μN/s. Twenty-five experiments per setting were performed in a square grid arrangement with each indent spaced 60μm apart. The probe tip area function, $A_c(h_c)$, was fitted with a 6^{th} order polynomial using the known properties of fused silica. The frame compliance of the instrument was calibrated separately using the indentation data of fused silica with a Berkovich indentation probe.

4.2.3. Data Analysis.

Oliver-Pharr Analysis. Oliver-Pharr method was first used to approximate the mechanical properties from nanoindentation data (Oliver, 1992). In this methodology, the contact stiffness S is first obtained from the elastic unloading curve:

$$S = \frac{dP}{dh} \tag{1}$$

Then the contact depth h_c was determined using the following formula

$$h_c = h_{max} - h_{sink\text{-}in} \tag{2}$$

where $h_{sink\text{-}in}$ is the amount of sink-in depth, as shown in Figure 4.1. By using Sneddon's force-displacement relationship, we have

$$h_{sink\text{-}in} = \varepsilon \frac{P_{max}}{S} \tag{3}$$

where the geometrical constant ε is 0.75 for the paraboloid of revolution used in this work. The projected contact area is then calculated using h_c and the pre-calibrated area function $A_c(h_c)$ (Figure 4.1). Finally the hardness and indentation modulus can be calculated using the following formulas

$$H = \frac{P_{max}}{A_c h_c} \tag{4}$$

$$E_r = \frac{1}{\beta} \frac{\sqrt{\pi}}{2\sqrt{A_c h_c}} S \tag{5}$$

where β is a correction factor that depends on indenter shape. For axisymmetric indenters, β is 1.

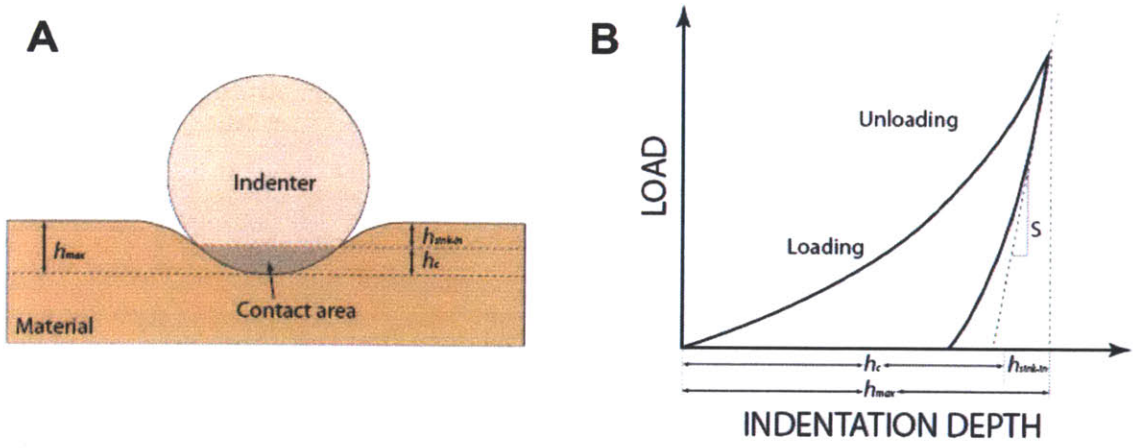

Figure 4.1. Nanoindentation concepts. A) Geometric approximation used to estimate contact area, and B) generalized indentation curve for indentation experiments.

John-Kendall-Roberts Analysis. Several variations of the John-Kendall-Roberts (JKR) method were used to determine the modulus for the aerogel and hydrogel samples. This model generally

modifies the Hertz model with the addition of prefactors that take into account the adhesion between the tip and sample surface. The model relies on the assumption that the probe radius is large compared to the indentation depth, and that the adhesion is sufficiently high between the probe and sample surface.

Figure 4.2 indicates the general force-indentation curve for an adhesive sample. Two similar models for the elastic modulus of adhesive samples were developed by Carillo and Gupta. In these, S is the contact stiffness and is determined in the same manner as the Oliver-Pharr method described above. R is the radius of the probe used, P is the maximum load applied to the sample, ν_s is Poisson's ratio, and F_{po} is the force required to pull the tip off of the sample surface. The equations for the reduced elastic modulus for Carillo and Gupta are shown below.

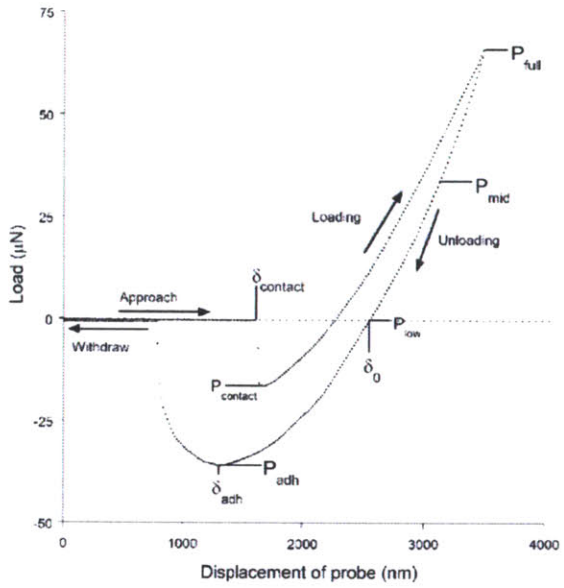

Figure 4.2. General indentation curve for adhesive material (Ebenstein 2011).

$$E_s^{JKR} = \sqrt{\frac{S^3(1-\nu_s^2)^2}{6R}\left[\frac{1}{P + 2F_{po}^{JKR} + 2F_{po}^{JKR}\sqrt{\left(\frac{P}{F_{po}^{JKR}} + 1\right)}}\right]} \quad (6)$$

(Carillo, 2005)

$$E_{JKR} = \sqrt{\frac{S^3(1-\nu^2)^2}{6R}} \cdot \left[\left(\frac{2}{3\sqrt{1+\frac{P}{F_{po}}}} + 1 \right)^3 \frac{1}{P + 2F_{po} + 2F_{po}\sqrt{\left(1+\frac{P}{F_{po}}\right)}} \right] \tag{7}$$

(Gupta, 2006)

Ebenstein compared various fitting models to account for adhesion. The first model is a two point fit using δ_o and δ_{adh} determined from the force-indentation plot in Figure 4.2. Using these two values in the Equation (8) below for the Ebenstein 2-point model, the reduced modulus is determined. This less rigorous approach was then compared with an adhesion curve fit that involves determining the pull-off force, P_{adh}, and then fitting the range of data from P_{adh} to $-P_{adh}$ to Equation (9), the Ebenstein mid-fit model, for the reduced modulus. The fitted values are $\delta_{contact}$, a_o, and P_{adh} allowing the calculation of the reduced modulus as $E_r = -3RP_{adh}/a_o^3$. Results with PDMS indicate that the 2-point and mid-fit models do not statistically differ in the determination of the reduced modulus (Ebenstein, 2011). JKR based E_r calculations in this work will compare the Carillo, Gupta, Ebenstein 2-point, and Ebenstein mid-fit models.

$$E_r = \frac{-3P_{adh}}{\sqrt{R}} \left[\frac{3(\delta_0 - \delta_{adh})}{1 + 4^{-2/3}} \right]^{-3/2} \tag{8}$$

(Ebenstein, 2011)

$$\delta - \delta_{contact} = \frac{a_0^2}{R} \left(\frac{1 + \sqrt{1 - P/P_{adh}}}{2} \right)^{\frac{1}{3}} - \frac{2}{3}\frac{a_0^2}{R} \left(\frac{1 + \sqrt{1 - P/P_{adh}}}{2} \right)^{\frac{1}{3}} \tag{9}$$

(Ebenstein, 2011)

Data Analysis. AFM data was initially tilt corrected and zeroed within the Asylum-Igor workspace. Contact stiffness and force indentation model fits were performed in Matlab (MathWorks, Natick, MA).

4.3 Results and Discussion

4.3.1. Hydrogels.

Characteristic indentations for the E3 and DSPH-SWCNT hydrogels are shown in the Figure 4.3 below. The saw tooth pattern seen in the Figure 4.3 (B) retraction curve for E3 hydrogels is similar in form to the unfolding of proteins in single molecule tension tests. This saw tooth pattern was observed in all E3 hydrogel force-indentation curves and suggests that the hydrogel adhered to the 20μm borosilicate glass sphere successively detached gel domain regions of various sizes and adhesive forces. The DSPH-SWCNT gel characteristic force-indentation plot, on the other hand, depicts a more distinct pull-off force compared to the E3 hydrogels. This pull-off force of the DSPH-SWCNT sample increased with successive indentations on the same location as seen in Figure 4.4. This increase in pull-off force may be due to increasing CNT and phage debris adhesion onto the borosilicate spherical probe.

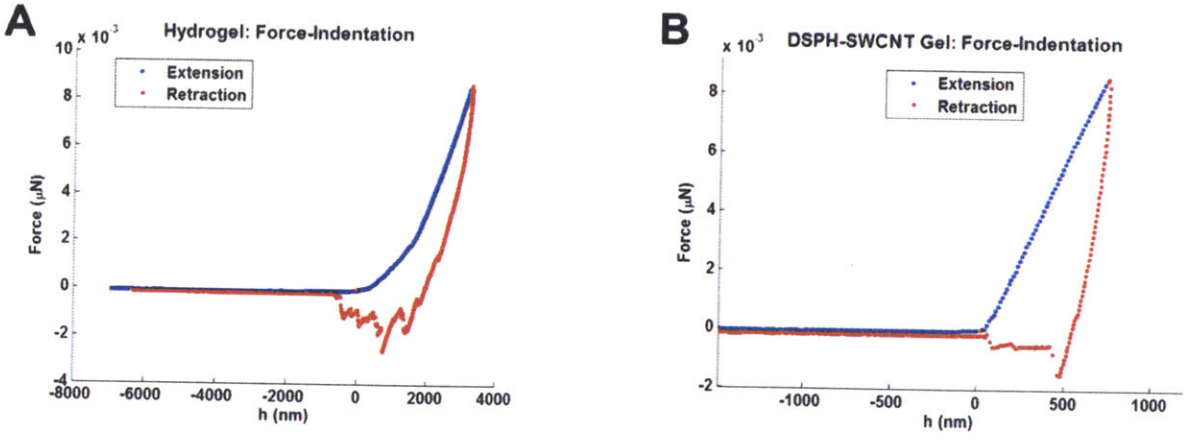

Figure 4.3. Representative hydrogel indentation curves. A) Representative E3 hydrogel Force-Indentation curve. B) Representative DSPH-SWCNT hydrogel Force-Indentation curve.

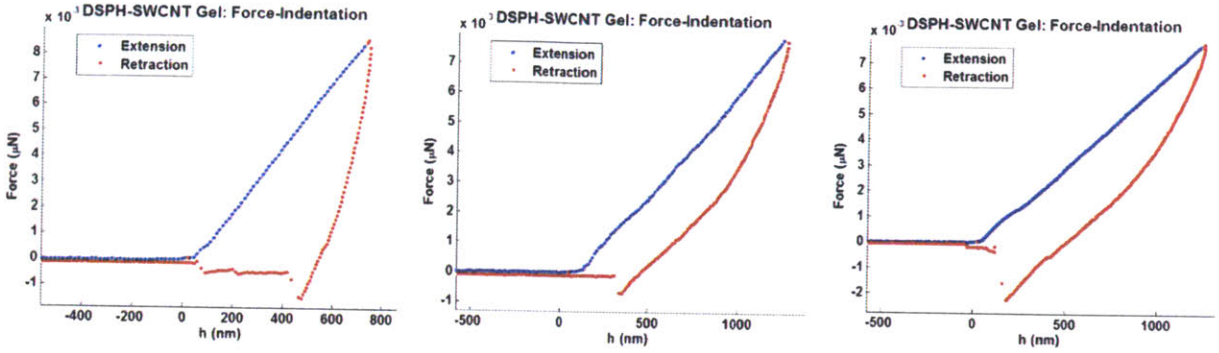

Figure 4.4. Sequential indentations on the DSPH-SWCNT hydrogel at the same location. From left to right the first, second, and tenth sequential indentations. The pull-off force nearly doubles over the course of indentations.

The indentation modulus was calculated for all of the hydrogel experiments using the JKR method previously described. This model was chosen due to the high adhesion seen in the samples upon retraction of the tip, and the fact that the indentations were less than the radius of the chosen tip. Different variations of the basic JKR model were used to compare results between models to include the Ebenstein 2-point, Ebenstein mid-fit, Gupta and Carillo models. Figure 4.5 shows the results of the indentations for sequential indentations. As evident from the graph, there was little variation in the modulus with subsequent measurements for the E3 hydrogel film. However, there was noticeable variation in the modulus estimates between models, although all models yield values on the same order of magnitude. The Gupta model appears to give the highest estimate on average, while the mid-fit model gives the lowest estimate.

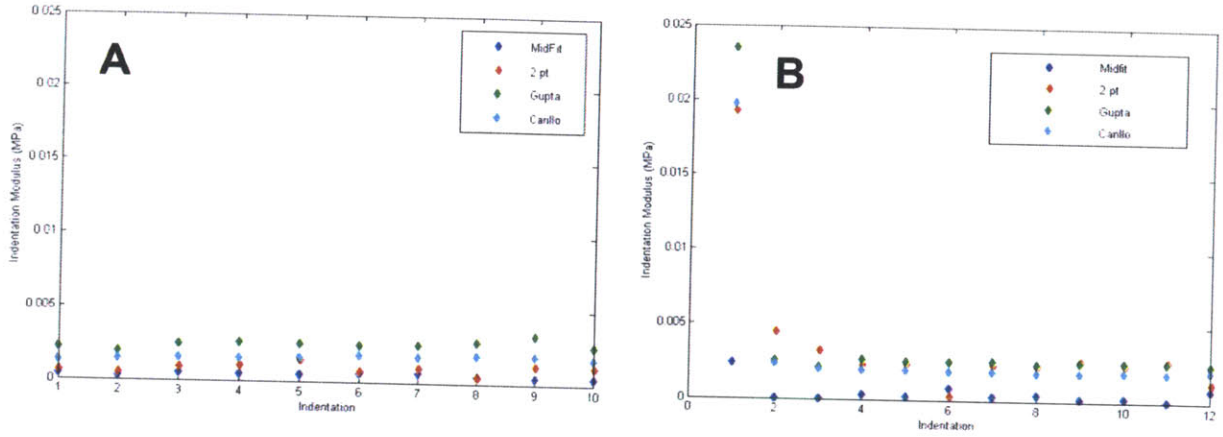

Figure 4.5. Hydrogel indentation modulus vs indentation number. A) E3 hydrogel. B) DSPH-SWCNT hydrogel. Legend colors: Blue – Ebenstein Midfit. Red – Ebenstein 2-point. Green – Gupta. Blue – Carillo.

Figure 4.5 indicates that there was no statistically significant variation between the E3 hydrogel samples and the latter indentations of the DSPH samples functionalized with carbon nanotubes in any of the models. This is contrary to our original hypothesis that the nanotubes would serve to create a stiffer hydrogel. While the initial modulus of the CNT functionalized hydrogels is quite a bit higher, this rapidly decreases after a single indentation. The reasons for this are not immediately apparent, and additional investigation is required to determine if the CNTs are being disrupted or moved within the sample. The reason for the similar values between the two might be justified based on the size difference between the virus used in the synthesis of the hydrogel, and the bound carbon nanotubes. The CNT's are roughly half the axial length of the virus. It may be that the CNT's are predominantly bound to the virus between junctions, meaning that there is little bridging of the crosslinks with the stiffer CNTs. Thus, the junction points likely have the same degrees of freedom in both samples. Another possible explanation is that the stiffening effect of the CNTs is balanced by a lower glutaraldehyde mediated crosslink density in the DSPH film. Further studies on the variation of crosslink density of these films are required to determine whether this is the case.

Table 4.1. E_r comparison based on the four different JKR models.

Sample	Model Modulus (kPa)			
	Mid Fit	2-pt	Gupta	Carillo
Sequential Indents				
Hydrogel film	0.45±0.10	0.87±0.33	2.53±0.3	1.64±0.19
DSPH-CNT Hydrogel	0.46±0.67	3.81±4.98	4.27±6.06	3.45±5.13
Variation Across Surface				
Hydrogel film	0.29±0.20	0.54±0.50	1.43±0.75	0.51±0.33

Table 4.1 shows the results of hydrogel moduli variation with sequential indentations and across the surface of the sample using the four JKR based models. The standard deviations are quite high, leading to the conclusion that the hydrogel stiffness varies across the film. This may result from film heterogeneities that resulted from gelification and subsequent sample handling. Although this particular hydrogel has not previously appeared in the literature, the modulus is within the 0.1-100 kPa range given by Kloxin et al (Kloxin, 2010) for covalently linked hydrogels, and only about an order of magnitude lower than the low end values found for Gelatin, 20 kPa (Domke, 1998). The results in Table 4.1 provide an initial starting point in characterizing phage based hydrogels. The gels used in this study were formed from a single phage concentration of $1x10^{14}$pfu/ml. The variation of mechanical properties of hydrogels formed from different starting concentrations would be of interest, particularly in determining how robust hydrogels are to scaled-up processing steps. Further, different mechanical properties of the DSPH-CNT hydrogels may manifest with differing phage concentrations and phage to carbon nanotube ratios.

4.3.2. Aerogels.

The DSPH-SWNT aerogel force-indentation depth curve in Figure 4.6 displays adhesion behavior during retraction, and also has a slight sawtooth shape at pull-off, which is expected from an adhesive cross-linked chain network. The indentation was performed in air using an AC160TS probe tip at a velocity of 10 um/s. Using the same JKR models as for the hydrogel analysis, the Gupta model yielded the highest reduced modulus of E_r = 442.62 ± 120.27 MPa. One caveat of this analysis is that the probe tip diameter of 9nm was relatively small given the porous nature of the aerogel. In general, the JKR model calls for a large probe radius. Confirmation of these results with a large probe radius is necessary in future work.

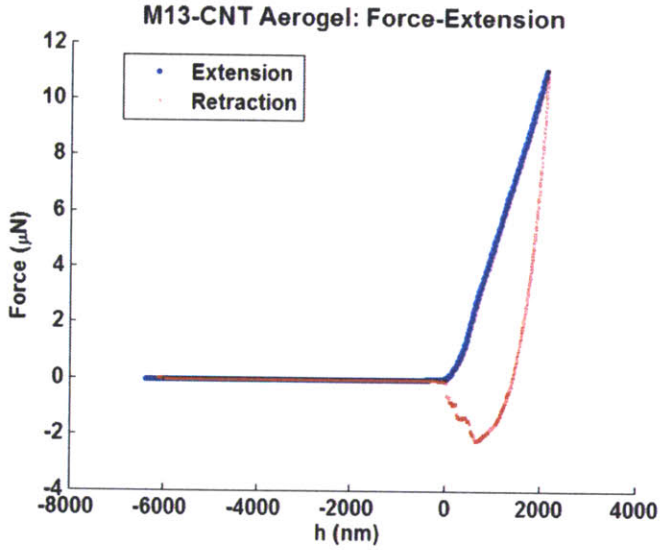

Figure 4.6. Representative phage-aerogel Force-Indentation curve.

Table 4.2. Comparison of aerogel sample E_r using four different JKR models.

Sample	Model Modulus (kPa)			
	Mid Fit	2-pt	Gupta	Carillo
Aerogel	148.68±61.67	157.76±65.41	442.62±120.27	332.34±97.18

4.3.3. Copper Nanowire Networks.

The copper nanowire network films were morphologically characterized using a scanning electron microscope. Figure 4.7 depicts a contiguous network of beaded nanowires with large pores relative to nanowire diameters. The representative force-indentation curve of copper nanowire films in Figure 4.8 indicates a nearly pure elastic response. Every indentation curve had the same curve shape (n=22). At the peak load force, a negative hysteresis is observed and this is regarded as an artifact. Based on the nearly 7μm indentation depth, the AFM z-piezo may have reached a non-linear region of its voltage response. Also, the copper force-indentation curves were manually truncated for the near vertical response when the probe reached the underlying silicon substrate. Based on the inorganic metal nature of the porous copper scaffold being commensurate with metal foam, a plastic component of the force-extension relationship was expected. Given that the peak of the curve lies at the depth of the substrate, densification effects are also expected, but not evident.

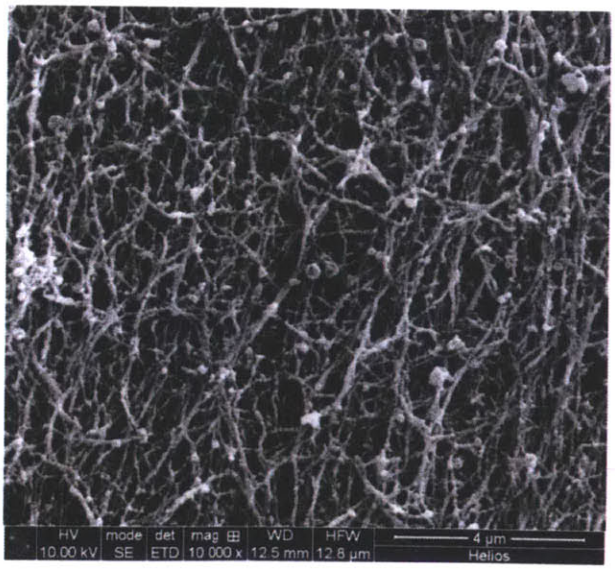

Figure 4.7. SEM image of copper nanowire network.

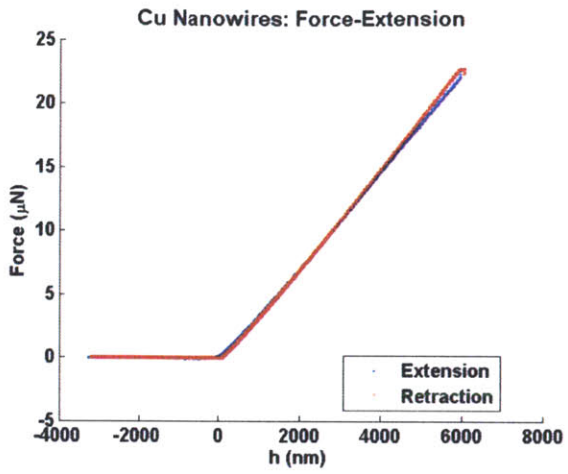

Figure 4.8. Representative copper nanowire Network Force-Indentation Curve.

One possible explanation for the elastic response of the copper nanowire network lies in the sample preparation. In the event that the phage hydrogel did not completely mineralize, it may be that the top layer of the network was mineralized, while the underlying gel network dried to a multi-micron thick organic layer. This hypothesis is shown in the schematic in Figure 4.9. This phenomenon was previously observed for metal nanowire sample synthesis not tested in this study. The cause of a differential layered film is likely due to mass transport of electroless deposition precursors being consumed at the outer gel layer before diffusing into the inner hydrogel layer proximal to the substrate. This layered structure would likely convolute the elasto-plastic response of the copper nanowires with the possible underlying phage organic layer.

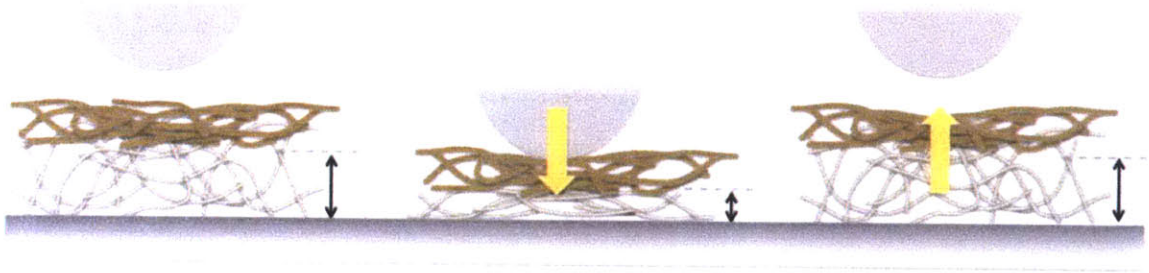

Figure 4.9. Possible mechanism for partially mineralized nanowire networks to exhibit completely elastic indentation behavior. Mineralized copper nanowires form the top layer of the film. Unmineralized phage form the bottom level of the film next to the substrate.

The Oliver-Pharr model was used to determine the copper nanowire film reduced modulus and hardness. These values are 1.24 ± 0.18 MPa and 3.29 ± 0.98 MPa respectively. These values are just below the range of elastic moduli for low density porous films (Ashby, 1999).

4.3.4. Nickel Nanowire "Thick" Film Networks.

The "thick" nickel nanowire network morphology was characterized with a scanning electron microscope shown in Figure 4.10 revealing a 16.9μm thick contiguous network similar to that of the copper nanowires. The "thick" designation is in comparison to the 3μm "thin" films in the next section. The outer or top surface of the network has thicker nanowires, with the diameter decreasing as the underlying substrate is approached. The likely cause of this variable thickness morphology is due to the electroless deposition mass transport phenomenon previously discussed. The nickel film was indented with a diamond DNISP probe. The characteristic force indentation curve in Figure 4.11 depicts successive plastic fracture that appears to correspond to the differential nanowire diameter profile as seen in the SEM image in Figure 4.10. The force-indentation profile shows evidence of elastic, plastic and fracture load responses. The fracture

response of the nickel nanowires is seen in post-indentation SEM images in Figure 4.12. Little evidence is seen of plastic nanowire compaction within the indentations. The Oliver-Pharr model was used to determine the sample reduced modulus and hardness. These values are 40.71 ± 6.41 MPa and 9.15 ± 4.52 MPa respectively. These values are at the low to mid- range of elastic moduli and hardness values for low density porous films (Ashby, 1999).

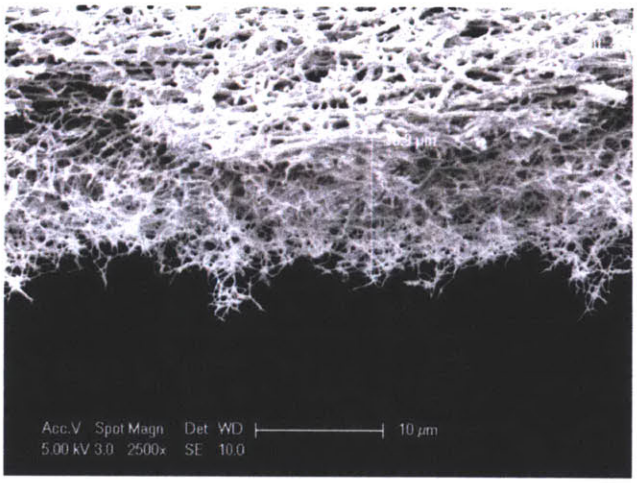

Figure 4.10. SEM cross section of nickel nanowire "thick" film. Thickness scale bar = 16.9µm.

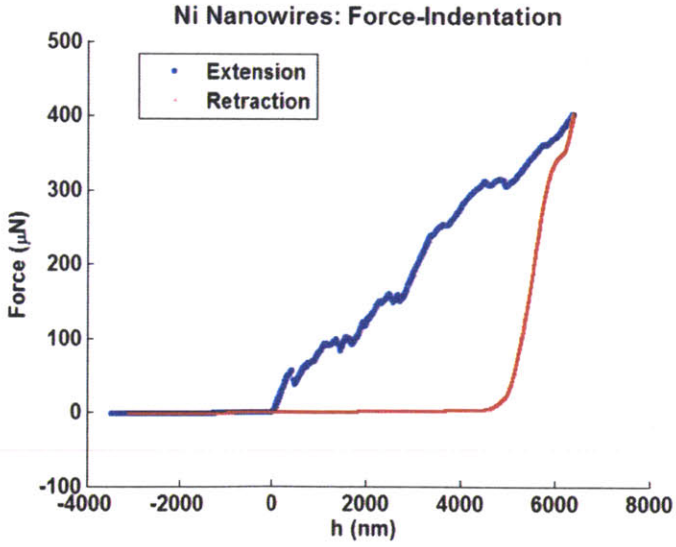

Figure 4.11. Representative "thick" nickel nanowire Network Force-Indentation Curve.

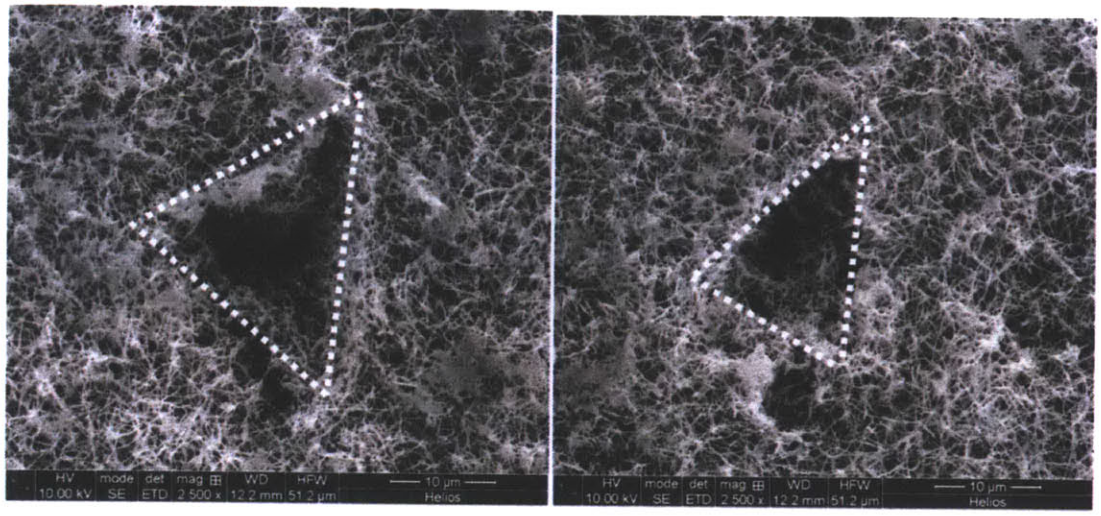

Figure 4.12. SEM view of DISPH diamond probe indentations into the nickel nanowire "thick" film.

4.3.5. Nickel Nanowire Thin Film Networks.

Two nickel nanowire thin films (thickness: ~ 3μm) were tested: a film immersed in a nickel electroless deposition bath for 14.5 hours and one for 20.5 hours. As shown in Figure 4.13, the mineralized nanowires form a crosslinked porous structure that resembles a nanoporous open cell foam structure. The mean diameter of the individual nanowires is 141 nm, and the mean diameter of the open cells is 335 nm based on the measurements using SEM images. The thin nickel nanowire film differs from the thick nanowire film in the previous section in the morphology of the nanowires themselves. The nanowires in the thin film present a more rough and beaded appearance than those in the thick film. This difference likely results from the different ELD bath compositions and reduction times used for each. The film thickness of the two samples was approximately 3μm determined by profilometry. The film thickness was also measured using SEM observations of FIB-milled cross-sections, as shown in Figure 4.13 (B), and the thickness measured agrees with the profilometer measurements.

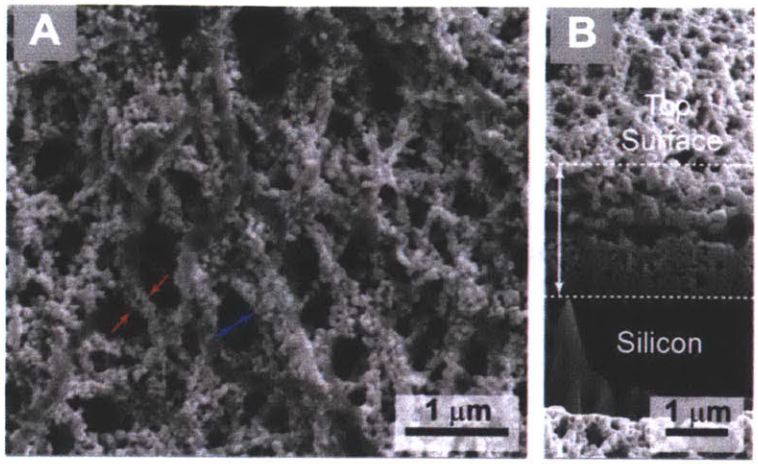

Figure 4.13. SEM image of thin nickel nanowire networks exposed to 14.5h of nickel electroless deposition. A) Top view. B) Cross-section view. Red arrows indicate nanowire diameter. Blue arrows indicate pore size.

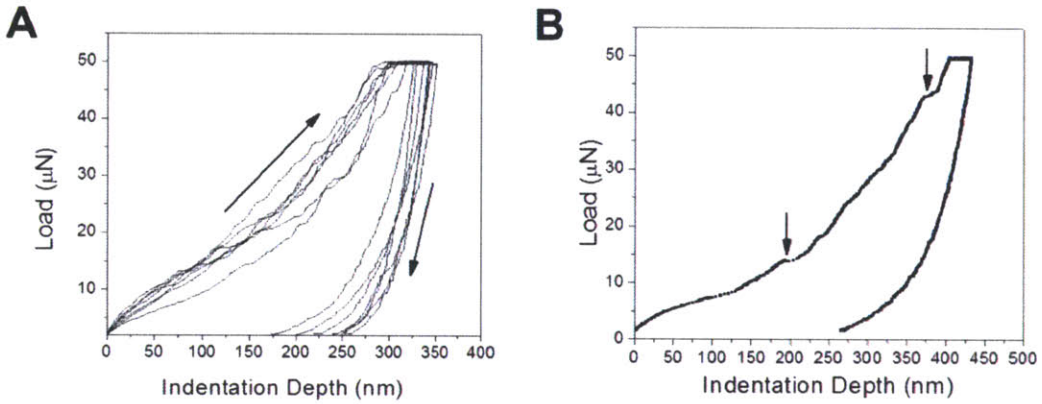

Figure 4.14. A): Nanoindentation curves obtained on the 14.5h nickel nanowire thin film networks using a 10 μm diamond conical indenter. B) A single indentation curve showing kinks (marked by arrows) from collapse in porous structure.

Figure 4.14 shows seven representative individual nanoindentation curves for the 14.5h thin nickel film. Kinks on the loading curve suggest a collapse of the porous structure during the indentation process. Figure 4.15 shows the averaged load-depth curves of the 14.5h and 20.5h films corresponding to two maximum loads (n=25 curves for each experiment condition). Although the initial portions of loading curves overlap with different maximum loads for both

samples, there is a large spread among the individual curves, as indicated by the wide error bars in Figure 4.15. The maximum depth for all the experiments conducted is less than 1100 nm, which corresponds to ~37% of the total depth of the film. There is a slight change in slope for the loading portion at approximately 26 nm, similar to the results of uniaxial compression tests of cellular materials.

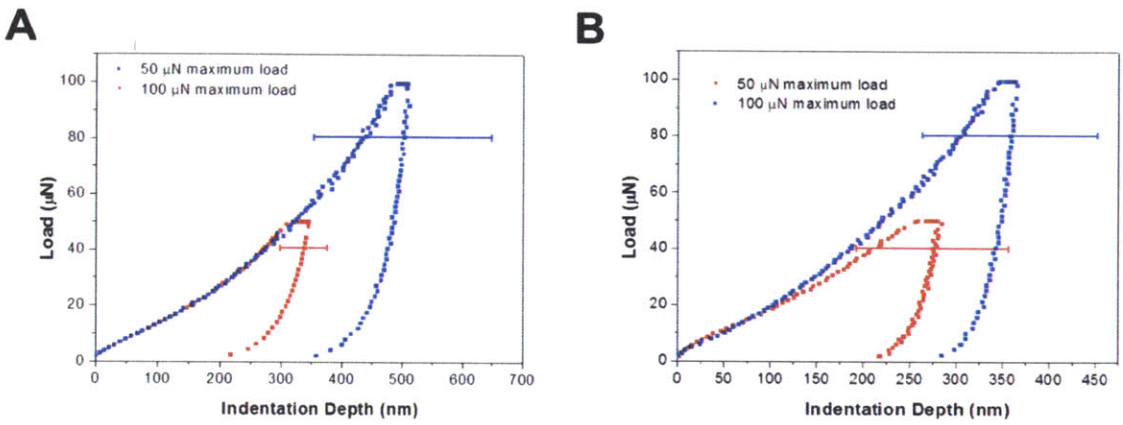

Figure 4.15. Averaged nanoindentation curves with error bars corresponding two maximum loads. A) 14.5h thin nickel film, and B) 20.5h thick nickel film. Blue corresponds to a 50μN maximum load and red to 100μN.

Using the standard Oliver-Pharr scheme as described in the data analysis section, the as-calculated indentation modulus and hardness with a function of indentation depth is summarized inFigure 4.16. As shown in this figure, both modulus and hardness first decrease with indentation depth, remain constant from ~250 to 600 nm, and then increase again when the maximum indentation depth is beyond 600 nm. The indentation modulus and hardness within 250nm and 600nm indentation depth are 0.69±0.48 GPa and 13.18±6.02 MPa (14.5h film), and 0.79±0.48 GPa and 12.37±5.29 MPa (20.5h film), respectively.

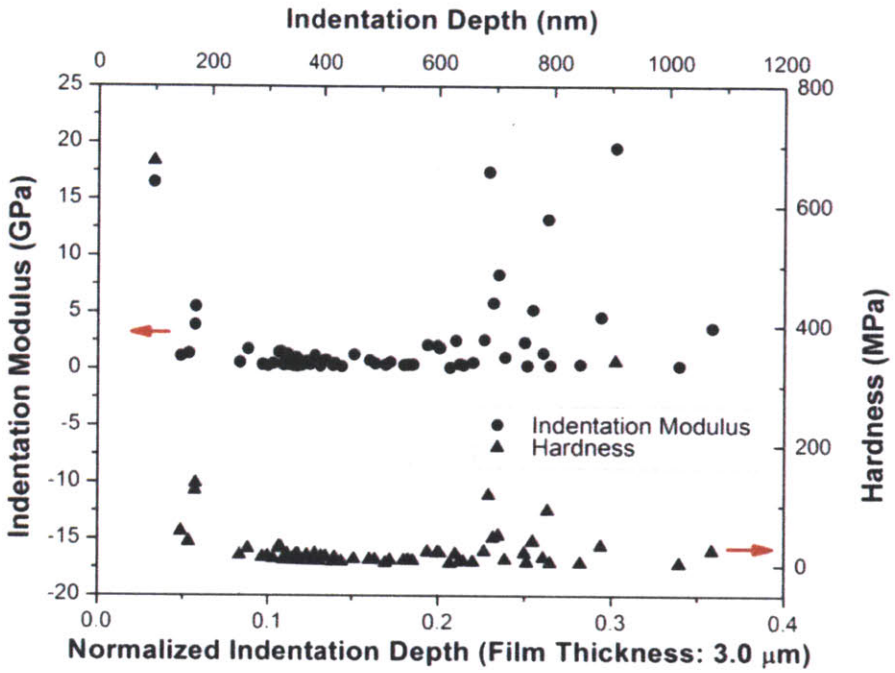

Figure 4.16. Indentation modulus and hardness as function of indentation depth for 14.5h thin Ni nanowire film.

Since the calculated modulus and hardness are strongly depth-dependent, a careful and complete interpretation of the data is critical. The first issue relates to the estimation of the contact area. SEM and FIB were used to accurately determine the indentation depth and remaining indent area, which reveal that the diameter of the remaining indent area is very close to the probe diameter. For example, a typical measurement reveals that the diameter of indent is 9.537μm, from which the indentation depth can be calculated as 1.21μm. The measured indentation depth is 1.13μm found by using FIB cross-sectioning. This measured value is very close to the difference between the calculated maximum indentation depth and the general elastic recovery of approximately 0.1μm. In this case, the contact depth is equal to the maximum indentation depth, h_{max}.

The above reasoning indicates that the contact area found using the standard Oliver-Pharr method is an underestimation, and hence both the modulus and hardness are overestimations. Recently, some researchers also reported that nanoporous gold does not show elastic deformation adjacent to the indentation area, and that the contact depth h_c can be replaced by the maximum indentation depth h_{max} (Biener 2005). Using a new contact area model corresponding to our probe tip geometry, we obtain modulus and hardness estimates shown in Table 4.3 that are about 6-8% and 11-15% lower than those obtained from the standard Oliver-Pharr model.

Table 4.3. Overestimation from standard Oliver-Pharr model due to different contact area approximation.

Nickel Film	E	H
14.5h	7.41%	14.24%
20.5h	6.00%	11.64%

We also consider the relative size between the contact area and average pore sizes of the film. As described above, the average diameter of the nanowires and open pores are 141 and 335 nm, respectively. As shown in Figure 4.17, the nanowire network is simplified as a foam structure with square-shaped cells with the dimension of 476 nm, the sum of the diameter of nanowires and size of pores. Using this scheme, the number of nanowires within the contact area during the indentation test increases with the indentation depth almost linearly. At the initial indentation contact, the number of nanowires under the indentation probe is limited and local deformation of individual nanowires might occur. Moreover, since the indenter first makes contact with the sample surface with a setpoint load of 2μN in order to stabilize the piezo and monitor the drift, the indenter might just be contacting several nanowires. In this case, it is

possible to bend or fracture the nanowires during this stage since the load to require bend a single Ni nanowire is in the tens of μN range (Celik, 2011). Therefore, at the initial loading stage, the indentation depth may not be very accurate, and it is also strongly dependent on the local distribution of nanowires because the film is not homogeneous at this scale.

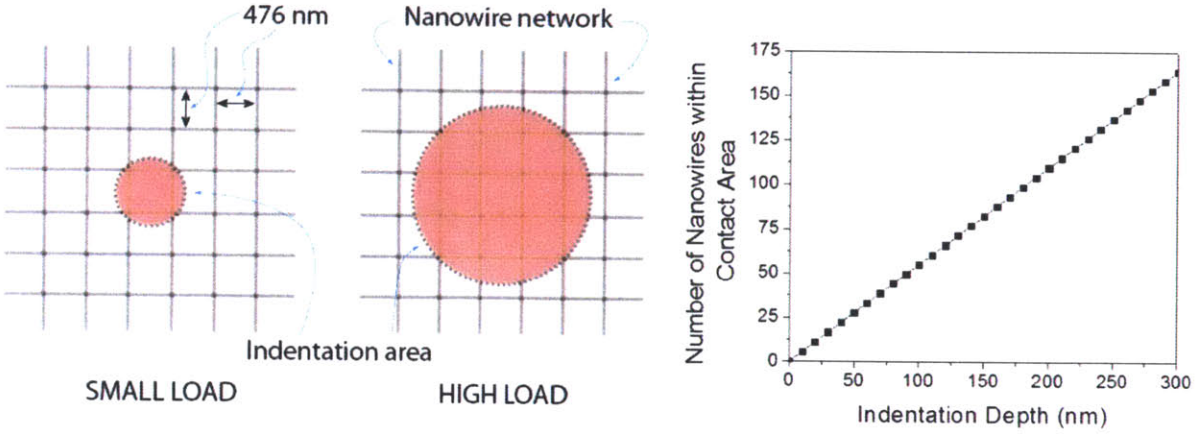

Figure 4.17. Indentation probe geometry comparison to nanowire network. A) Nanowire network simplified as square foam structure. B) Linear relationship between number of nanowires in contact and indentation depth.

For porous materials, both the elastic modulus and yield stress depend on the porosity. It was previously shown that the resistance to indentation increases with decreasing porosity (Fleck, 1992). Volinsky et al. found that both indentation modulus and hardness of porous low-k dielectric films increase with penetration depth as a result of densification of the material (Volinsky, 2003). By using computation simulation and experiment results, Chen et al also studied the effects of densification on the modulus and hardness (Chen, 2001). These studies suggest that the indentation modulus and hardness calculated using the standard Oliver-Pharr method cannot represent the intrinsic material properties of the original porous structure, because the material has densified.

The densification of these nanowire network films can be directly visualized by observing the indents using SEM. As shown in a typical top-view of the indent area in Figure 4.18, the deformation is localized under the indenter. As shown in the magnified image, the pore size within the indentation area is greatly reduced, and in some cases, the pores were completely closed in the center of indentation area (arrow 1). In the area between the center and contact edge, the pores are reduced but not fully closed (arrow 2). In the area immediately beyond the indentation area, the pores have similar dimensions as compared to far-field pores (arrow 3). The structure adjacent the contact area is undeformed, and no brittle fracture or crack emission was observed.

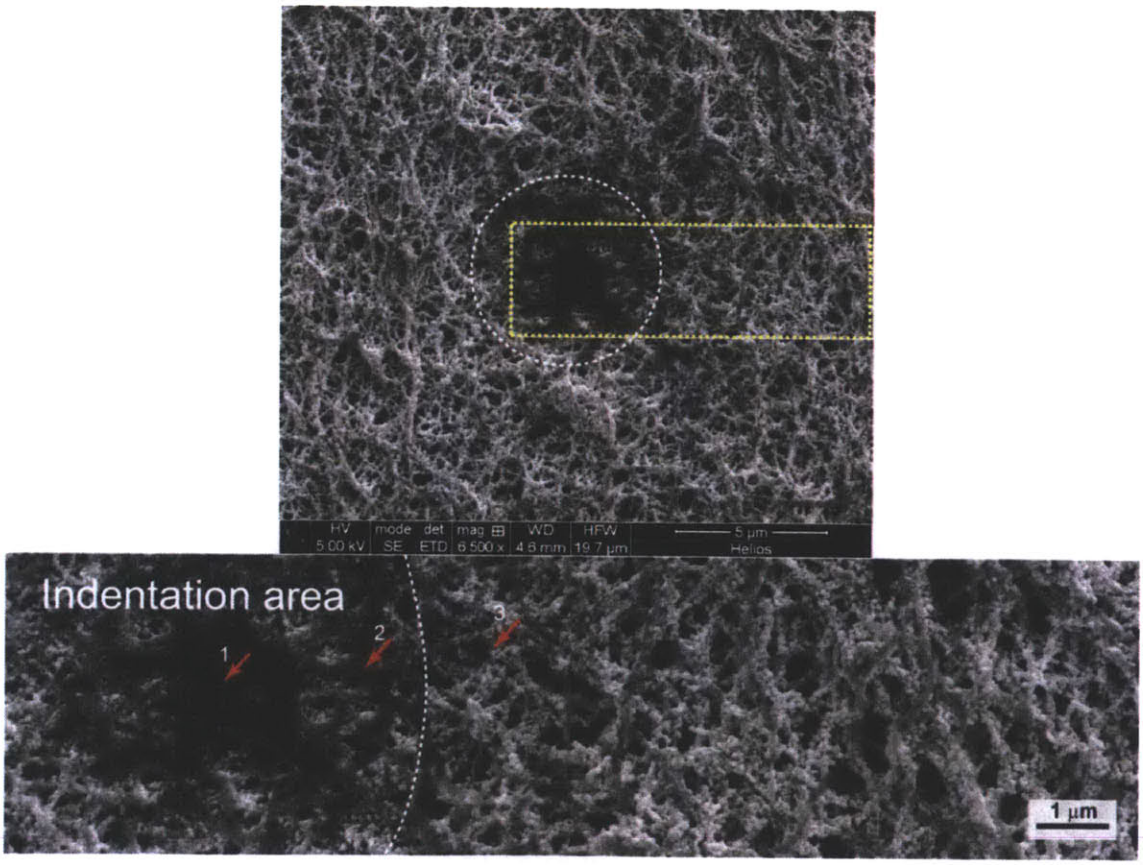

Figure 4.18. Densification of nickel nanowire networks. Top image shows indentation area with the lower enlargement highlighted in yellow. Lower image inidcates 1) closed pores, 2) partially closed pores, and 3) open pores near center.

The densification beneath the surface is more clearly revealed by using FIB, as shown in a typical cross-section image of the indentation area seen in Figure 4.19. Under the indentation area, the pore dimensions and porosity shown with yellow arrows are clearly reduced as compared to the surrounding undeformed area indicated by white arrows.

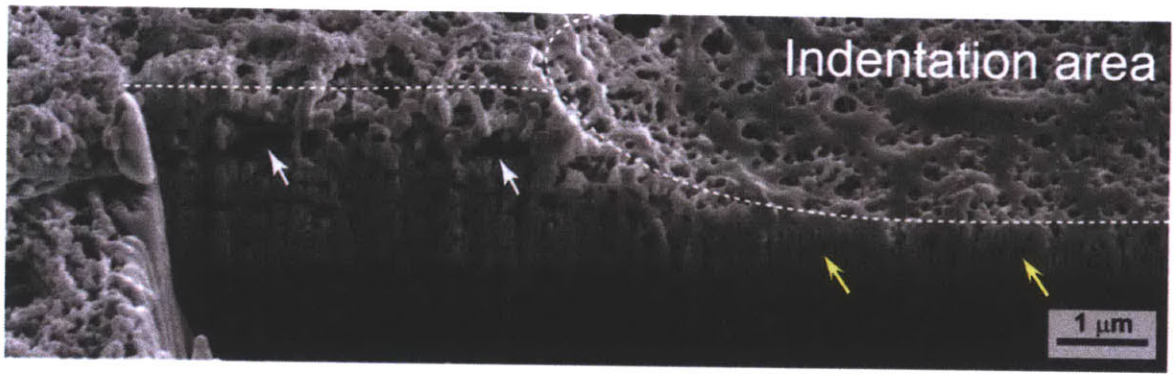

Figure 4.19. FIB cross-section showing pore collapse profile at indentation area. The pore dimensions and porosity shown with yellow arrows are clearly reduced as compared to the surrounding undeformed area indicated by white arrows.

Another issue of concern is the substrate effect. In order to avoid a substrate effect, it is known that generally indentation with maximum depths of less than 10-20% of the film thickness are required to obtain the intrinsic film properties (ASTM E384 – 10e2). However, the maximum depth for the thin nickel film measurements is about 35% of the total depth in order to obtain reliable data. Chen et al. performed a numerical study on the substrate effect of thin film for nanoindentation measurements (Chen, 2001). According to the ratio of E_f/E_s and σ_f/σ_s (E_f and E_s are the moduli for the film and substrate, σ_f and σ_s are the yield stress for the film and substrate, respectively), the authors distinguished the cases between soft film on hard substrate and hard film on soft substrate. The Young's modulus and yield strength of silicon are 150 and 7

GPa, respectively (Bushan, 2006). The yield stress of the film is related to the hardness from indentation measurement through the following equation

$$H = c_b \sigma_f \tag{10}$$

where c_b is a constraint factor that depends on the indenter shape and material properties (Chen, 2010). A value of $c_b = 3$ is usually assumed for dense materials. However, it is shown that the deformation of porous materials is not constrained by the surrounding material due to the densification beneath the indenter. In this case, the indentation test is similar to a uniaxial test, and the yield stress equals to the hardness (Biener, 2005; Fischer-Cripps, 2002; Gibson, 1997)

$$H = \sigma_f \tag{11}$$

If we use the value of hardness in the indentation range of 250-600 nm, the average yield strength is 13.18±6.02MPa and 12.37±5.29MPa for the 14.5h and 20.5h films, respectively. The Young's modulus is calculated using the following relation between the indentation modulus and Young's modulus

$$E_r = \frac{E}{1-\nu^2} \tag{12}$$

In this case, we assume ν is zero as there is almost no lateral deformation upon indentation for this plastic deformation.

Using the values of E_f and σ_f obtained above, the ratios of E_f/E_s and σ_f/σ_s we obtain are 0.0047 and 0.0019, respectively. Therefore, this case of nanoporous film on silicon substrate falls into the soft film on hard substrate category. If we do not consider the densification effect, assuming the film is in dense form, according to the numerical results reported by Chen et al, the hardness measured is close to the true value of the film (Chen, 2001). The estimation of

modulus cannot be judged since the ratios are out of the range of the simulation conditions in the report.

As discussed above, there are several issues that we need to consider when analyzing and reporting the data from this indentation experiment for the thin nickel nanowire network. These include estimation of contact area, initial statistical coverage of nanowires under the indentation probe, substrate effect, and densification. The relative influence of each mechanism with increasing indentation depth are summarized in Figure 4.20.

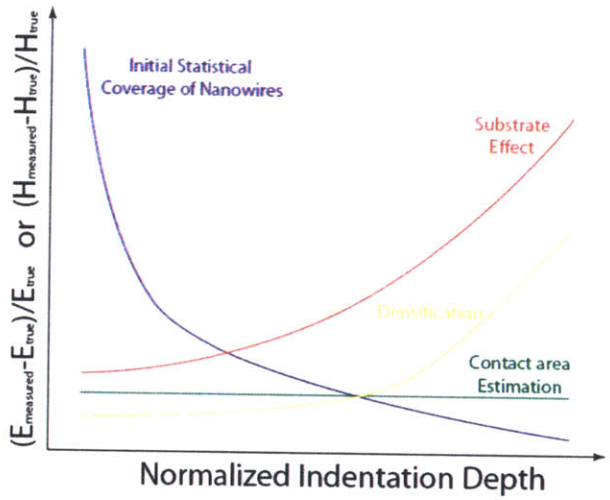

Figure 4.20. Relative influence of various effects on the measured mechanical properties as a function of indentation depth.

In this case, we know only the general trend for each effect and we are not be able to quantify the exact influence as a function of indentation depth, and therefore it is difficult to back-calculate the true materials properties from the current experimental results. In order to overcome this limitation, other mechanical testing (i.e. indentation with other indenter geometries and uniaxial compression) and relevant characterizations (i.e. porosity measurement) should be conducted, and the general mechanical constitutive law of the materials can be either established or adopted using other existing models. Then by using computational simulation, the effects in Figure 4.20

can be studied quantitatively, and fitting the experimental data will allow us to calculate the intrinsic material properties.

Nevertheless, we can use the scaling law for open-cell foams to roughly test our estimations,

$$\sigma_p = C_1 \sigma_b \left(\frac{\rho_p}{\rho_b} \right)^n \tag{13}$$

where σ_b and ρ_b are respectively the yield strength and density of the bulk solid counterpart, and σ_p and ρ_p are respectively the yield strength and density of the porous film. Literature values of σ_b for nickel range from 278 to 930 MPa (Namazu, 2007; Ebrahimi, 1999). Using the higher end of this range, we can estimate the relative porosity of the film to be 85%. This porosity estimate seems consistent with the SEM images of the nickel films.

Figure 22 summaries the indentation modulus and hardness the 14.5h and 20.5h nickel thin films using modified Oliver-Pharr method by modifying the contact area estimation using the above scheme. It can be seen that there is no statistical difference between the 14.5h and 20.5h films, despite the 6h difference in electroless deposition immersion time. This is not surprising since there is no significant morphological difference observed in SEM images between the two exposure times.

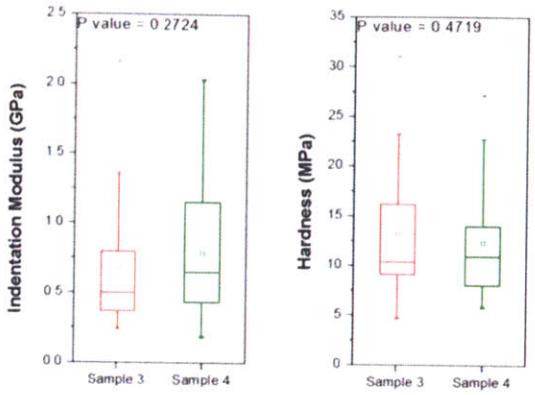

Figure 4.21. Statistical comparison of indentation modulus and hardness between thin nickel nanowire films. Sample 3 corresponds to 14.5h of electroless deposition immersion, and Sample 4 corresponds to 20.5h.

Lastly, the time-dependent mechanical response is studied, and the averaged indentation curves are summarized in the following figure. The curves do not overlap with each other for the loading portion due to non-uniformity of the film. The indentation modulus and hardness calculated using the standard Oliver-Pharr method do not show statistical significance among different unloading rates. No clear trend of these quantities with respect to the unloading rate was observed in the testing conditions.

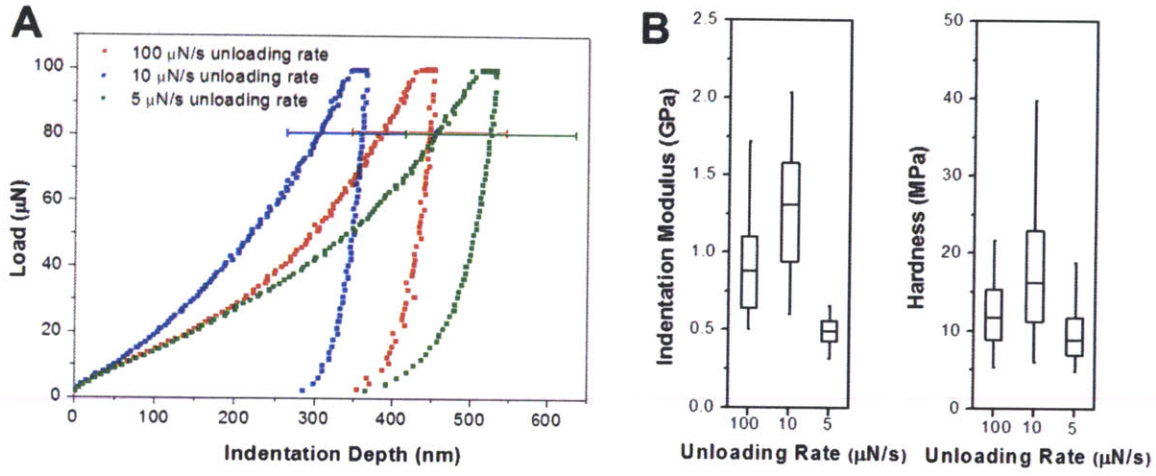

Figure 4.22. Effects of unloading rate on thin nickel nanowire film exposed to 20.5h of electroless deposition. A) averaged indentation curves. Unloading rate colors correspond to: red, 100μN/s; blue, 10μN/s; green, 5μN/s B) Indentation modulus and hardness.

Table 4.4. Mechanical properties sample summary.

Sample	E_r (MPa)	H (MPa)	Probe	Air, Liquid	Tip Speed	Loading Rate	Model
E3 Hydrogel, Film	2.53±0.3	-	20μm sphere	Liquid	8 μm/s	-	JKR-Gupta
DSPH-SECNT Hydrogel	4.27±6.06	-	20μm sphere	Liquid	8 μm/s	-	JKR-Gupta
Aerogel, Virus-SWCNT	442.62±120.27	-	AC160TS	Air	10 μm/s	-	JKR-Gupta
Copper Network	1.24±0.18	3.29±0.89	Diamond	Air	10 μm/s	-	O-P
Nickel "Thick" Film	40.71±6.41	9.15±4.52	Diamond	Air	10 μm/s	-	O-P
Nickel "Thin" Film, 14.5h	641.98±461.95	11.32±5.34	10μm conical	Air	-	10μN/s	Modified O-P
Nickel "Thin" Film, 20.5h	748.27±456.63	10.94±4.75	10 μm conical	Air	-	10μN/s	Modified O-P

Note: Tested samples and corresponding material parameters and testing conditions. JKR values correspond to the model with the highest moduli.

4.4 Conclusions

As summarized in Table 4.4, the virus-based hydrogels demonstrate elastic moduli at the low end of other polymer hydrogels such as poly(N,N-dimethylacrylamide) (PDMA), 2.8-89.5kPa (Kurokawa, 2002), PHEMA–co-EGDMA, ca 300kPa – 1.5MPa, and gelatin, 20kPa – 1MPa (Domke, 1998). With a minimal volume decrease from the initial phage solution to resulting cross-linked hydrogel, there is an estimated 99.7% water in the gel. This water content is near the upper range for hydrogels and the low observed elastic modulus is rationalized based on this parameter (Matzelle, 2008).

The inorganic copper and nickel nanowire networks form open pore systems that are structurally and mechanically similar to open cell metal foams. Commercially available metal foams have elastic moduli that range from ca 20MPa to 10GPa (Ashby, 2000). The nickel nanowire assemblies tested have elastic moduli at the low to mid-range of commercial foams. The elastic modulus of the copper nanowire sample is an order of magnitude less than the lower range of commercial foams and at the upper range for hydrogels, resulting from possibly incomplete mineralization of the hydrogel.

Based on these results, the two primary objectives of this study have been met: 1) indentifying appropriate sample indentation conditions and analysis models for each sample type, and 2) initially characterizing the elastic moduli of phage-based porous hydrogel, aerogel, and inorganic nanowire samples. Given the breadth of samples tested and indentation conditions optimized, the moduli values represent an initial material characterization. These initial results indicate that the range of phage-based 3-dimensional materials are mechanically robust and suitable for further materials development and device integration. Further investigation of each sample type should examine creep compliance, stress relaxation, and oscillatory load testing. In particular the hydrogels should be interrogated for a visco-elastic response.

4.5 References

Ashby, M. F., *Metal foams : a design guide*. Butterworth-Heinemann: Boston, **2000**; p xiv, 251.

ASTM E384 - 10e2: Standard Test Method for Knoop and Vickers Hardness of Materials. American Society for Testing and Materials: **2010**.

Biener, J.; Hodge, A. M.; Hamza, A. V.; Hsiung, L. M.; Satcher, J. H., Nanoporous Au: A high yield strength material. *Journal of Applied Physics* **2005,** *97* (2).

Bushan, B., Springer Handbook of Nanotechnology. **2006**. (Heidelberg: Springer)

Carrillo, F.; Gupta, S.; Balooch, M.; Marshall, S. J.; Marshall, G. W.; Pruitt, L.; Puttlitz, C. M., Nanoindentation of polydimethylsiloxane elastomers: Effect of crosslinking, work of adhesion, and fluid environment on elastic modulus. *Journal of Materials Research* **2005,** *20* (10), 2820-2830.

Celik, E.; Guven, I.; Madenci, E., Mechanical characterization of nickel nanowires by using a customized atomic force microscope. *Nanotechnology* **2011,** *22*, 155702.

Chen, X.; Vlassak, J. J., Numerical study on the measurement of thin film mechanical properties by means of nanoindentation. *Journal of Materials Research* **2001,** *16* (10), 2974-2982.

Chen, X.; Xiang, Y.; Vlassak, J. J., Novel technique for measuring the mechanical properties of porous materials by nanoindentation. *Journal of Materials Research* **2006,** *21* (3), 715-724.

Domke, J.; Radmacher, M., Measuring the elastic properties of thin polymer films with the atomic force microscope. *Langmuir* **1998,** *14* (12), 3320-3325.

Ebenstein, D., Nano-JKR force curve method overcomes challenges of surface detection and adhesion for nanoindentation of a compliant polymer in air and water. *Journal of Materials Research* **2011,** *26* (8), 1026-1035.

Ebrahimi, F.; Bourne, G. R.; Kelly, M. S.; Matthews, T. E., Mechanical properties of nanocrystalline nickel produced by electrodeposition. *Nanostructured Materials* **1999,** *11* (3), 343-350.

Fan, T. X.; Chow, S. K.; Di, Z., Biomorphic mineralization: From biology to materials. *Progress in Materials Science* **2009,** *54* (5), 542-659.

Fischer-Cripps, A. C., *Nanoindentation*. Springer: New York, 2002; p xx, 197.

Fleck, N. A.; Otoyo, H.; Needleman, A., Indentation of Porous Solids. *International Journal of Solids and Structures* **1992,** *29* (13), 1613-1636.

Gibson, L. J.; Ashby, M. F., *Cellular solids : structure and properties*. 2nd ed.; Cambridge University Press: Cambridge ; New York, 1997; p xviii, 510.

Gupta, S.; Carrillo, F.; Li, C.; Pruitt, L.; Puttlitz, C., Adhesive forces significantly affect elastic modulus determination of soft polymeric materials in nanoindentation. *Materials Letters* **2007,** *61* (2), 448-451.

Johnson, K. L., *Contact mechanics*. Cambridge University Press: Cambridge Cambridgeshire ; New York, **1985**; p xi, 452.

Johnson, K. L.; Kendall, K.; Roberts, A. D., Surface Energy and Contact of Elastic Solids. *Proceedings of the Royal Society of London Series a-Mathematical and Physical Sciences* **1971,** *324* (1558), 301.

Kloxin, A. M.; Kloxin, C. J.; Bowman, C. N.; Anseth, K. S., Mechanical Properties of Cellularly Responsive Hydrogels and Their Experimental Determination. *Advanced Materials* **2010,** *22* (31), 3484-3494.

Kovacs, G. T. A., *Micromachined transducers sourcebook*. WCB/McGraw-Hill: Boston, MA, 1998; p xx, 911.

Kurokawa, T.; Gong, J. P.; Osada, Y., Substrate Effect on Topographical, Elastic, and Frictional Properties of Hydrogels. *Macromolecules* **2002,** *35* (21), 8161–8166.

Lin, C. X.; Liu, Y.; Rinker, S.; Yan, H., DNA tile based self-assembly: Building complex nanoarchitectures. *Chemphyschem* **2006,** *7* (8), 1641-1647.

Matzelle, T.; Reichelt, R., Review: Hydro, micro- and nanogels studied by complementary measurements based on SEM and SFM. *Acta Microscopica* **2008,** *17* (1), 45-61.

Migneault, I.; Dartiguenave, C.; Bertrand, M. J.; Waldron, K. C., Glutaraldehyde: behavior in aqueous solution, reaction with proteins, and application to enzyme crosslinking. *Biotechniques* **2004,** *37* (5), 790.

Namazu, T.; Inoue, S., Characterization of single crystal silicon and electroplated nickel films by uniaxial tensile test with in situ X-ray diffraction measurement. *Fatigue & Fracture of Engineering Materials & Structures* **2007,** *30* (1), 13-20.

Oliver, W. C.; Pharr, G. M., An Improved Technique for Determining Hardness and Elastic-Modulus Using Load and Displacement Sensing Indentation Experiments. *Journal of*

Materials Research **1992,** *7* (6), 1564-1583.

Peelle, B. R.; Krauland, E. M.; Wittrup, K. D.; Belcher, A. M., Design criteria for engineering inorganic material-specific peptides. *Langmuir* **2005,** *21* (15), 6929-6933.

Spiering, V. L.; Bouwstra, S.; Spiering, R. M. E. J., On-Chip Decoupling Zone for Package-Stress Reduction. *Sensors and Actuators a-Physical* **1993,** *39* (2), 149-156.

Volinsky, A. A.; Vella, J. B.; Gerberich, W. W., Fracture toughness, adhesion and mechanical properties of low-K dielectric thin films measured by nanoindentation. *Thin Solid Films* **2003,** *429* (1-2), 201-210.

Xu, A. W.; Ma, Y. R.; Colfen, H., Biomimetic mineralization. *Journal of Materials Chemistry* **2007,** *17* (5), 415-449.

Yoo, P. J.; Nam, K. T.; Qi, J. F.; Lee, S. K.; Park, J.; Belcher, A. M.; Hammond, P. T., Spontaneous assembly of viruses on multilayered polymer surfaces. *Nature Materials* **2006,** *5* (3), 234-240.

CHAPTER 5

Future Work: Device Applications for 3-Dimensional Phage-Templated Scaffolds

5.1 Introduction

The work in Chapters 2-4 demonstrates the ability to synthesize multi functional, biotemplated inorganic 3-dimensional porous materials. These materials present beneficial electrical conductivity and mechanical stability. Such multi-functional materials should facilitate numerous applications in devices requiring 3-dimensional porous architectures. These applications include catalytic, photovoltaic, energy storage, and electro-optical devices. A solution-based approach using environmentally benign chemistries to create the active materials should provide a low cost synthesis route for applications that currently rely on expensive fabrication instrumentation and facilities. The covalently linked hydrogel, in itself, might serve as a generic platform for multi-functionalization.

To further the development the processing techniques for synthesizing 3-dimensional nanowire films, three approaches are examined here: 1) the development of catalytic film materials through the direct synthesis of palladium nanowires and the galvanic displacement of copper and nickel nanowires to more noble metals; 2) thermal annealing of the 3-dimensional nanowire films; and 3) the synthesis of phage films dried from phage hydrogels. Development of these approaches should expand the materials application space for 3-dimensional nanowire films.

5.2 Experimental

Hydrogel Formation. Stock 50% Glutaraldehyde Solution (Sigma Aldrich, CAS# 111-30-8) was placed in a reservoir. The specific gravity of the glutaraldehyde solution is 1.106. Virus solutions (either E3 or Y21M) in 1xPBS were pipetted onto a substrate. The loading factor for test samples was 10μl on an approximately $1cm^2$ untreated silicon wafer substrate. Substrates

with phage solution were inverted and placed onto the glutaraldehyde solution. The phage solution was allowed to remain in contact with the glutaraldehyde solution 30min. Cross-linked phage solutions were removed from the glutaraldehyde solution and transferred to 1L 1xPBS for 12-24h to remove excess glutaraldehyde from the resulting hydrogel.

Silver decorated copper nano-networks. Phage hydrogels were incubated in 10mM tetraaminepalladium (II) chloride monohydrate, $(NH_3)_4PdCl_2$ (Sigma Aldrich, CAS# 13933-31-8) for 8 hours. Excess palladium solution was removed by rinsing palladium sensitized hydrogels in 0.1M MOPS buffer for 12h. Copper electroless deposition solution consisted of: 0.032M $CuSO_4 \cdot 5H_2O$ (Mallinckrodt Chemicals, CAS# 4844-02); 0.040M ethylenediaminetetraacetic acid, disodium, dehydrate (EDTA) (Mallinckrodt Chemicals, CAS# 6381-92-6); 0.1M 3-(N-morpholino) propanesulfonic acid (MOPS) (Sigma Life Science, CAS# 1132-61-2); 0.067M dimethyl amine borane (DMAB) (Aldrich, CAS# 74-94-2). Sensitized hydrogels were incubated in the copper electroless deposition bath for 6 hours. Subsequent to metallization, films were rinsed in deionized water for two hours. Copper nanowires were not dried at this stage, but left hydrated in deionized water. A suspension of silver nanospheres stored in ethylene glycol was centrifuged at 14,000rpm and resuspended in ethanol. Centrifugation and resuspension of silver nanoparticles in ethanol was repeated. The copper nanowire film was removed from the deionized water rinse excess water droplets blotted away. Then 10μl of the silver nanoparticle solution was dropcast onto the hydrated copper network. The film was allowed to dry on the lab bench for 2 hours.

Palladium 3-dimensional networks. Phage hydrogels were prepared and as described above and incubated in 10mM $Na_2(NH_3)4PdCl_2$ in 0.1M MOPS buffer. Palladium was reduced with 10mM DMAB for 5min. Films were dried with deionized water and dried at ambient temperature.

Nano-Network galvanic displacement reactions. Copper and nickel nanowire 3-dimensional networks were exposed to 10mM Pd, Pt, Ag, and Au salt solutions for 1h. Films were rinsed with deionized water and dried at ambient temperature.

Thermal annealing for copper and nickel 3-dimensional networks. A Thermolyne 79300 tube furnace was used to anneal copper and film samples synthesized on silicon wafers. Argon gas with 4% hydrogen gas was used during annealing. Annealing temperatures ranged from 400-600°C with 30-45min ramp times.

Scanning Electron Microscope/Focused Ion Beam. A FEI Company Helios 600i Nanolab Dual Beam SEM/FIB was used for high resolution imaging and for cross-sectional etching samples. A working distance of 4.0-4.2mm was used with accelerating voltages between 5-10kV. When a high magnification level allowed, magnetic immersion mode was preferred for imaging. ICNA software was used for electron diffraction spectroscopy (EDS). FEI XL-30 ESEM (Environmental Scanning Electron Microscope) was used for general purpose imaging.

Dried phage films. Stock 50% Glutaraldehyde Solution (Sigma Aldrich, CAS# 111-30-8) was placed in a reservoir. The specific gravity of the glutaraldehyde solution is 1.106. Virus solutions (either E3 or Y21M) in 1xPBS were pipetted onto an untreated silicon wafer substrate.

Concentrations of $1x10^{13}$, $3x10^{13}$, $7x10^{13}$, and $1x10^{14}$pfu/ml were dropcast with a loading factor of 10μl on an approximately $1cm^2$ substrate. Substrates with phage solution were inverted and placed onto the glutaraldehyde solution. The phage solution was allowed to remain in contact with the glutaraldehyde solution 30min. Cross-linked phage solutions were removed from the glutaraldehyde solution and transferred to 1L 1xPBS for 12-24h to remove excess glutaraldehyde from the resulting hydrogel. Hydrogels were removed from the rinse solution and allowed to dry on the lab bench for 24 hours.

Profilometry. A Veeco DEKTAK 150 Profilometer was used to determine sample thicknesses. A razor blade was used to cut a "Z" at multiple locations along a profile path to assist in leveling the profile during analysis. A step height calibrated 2.5μm stylus was drawn over the sample with a 2.0-3.0mg force setting at an approximately 200μm/s scan rate. Average step heights were determined by calculating the difference between average profile height values of the substrate and top of the film surface. Surface roughness, R_q, values were determined over length scales of greater than 1000μm.

5.3 Results and Discussion

5.3.1. Catalytic 3-Dimensional Networks.

Three approaches were used to synthesize 3-dimensional films for possible catalytic applications. First a direct reduction of palladium onto an E3 hydrogel was done using 10mM $Na_2(NH3)_4PdCl_2$ in a 0.1M MOPS buffer and dimethyl amine borane as the reducing agent. The resulting scaffolds shown in Figure 5.1 indicate a beaded nanowire morphology, but a 3-dimensional porous structure is maintained similar to copper and nanowire films previously

demonstrated. Given the ability to directly reduce noble metals onto a virus hydrogel, many other bio-templating protocols should be amenable thereby expanded the set of possible porous materials.

Another approach to creating catalytic films was to expose a copper nanowire film to noble metal nanoparticles. In this case a suspension of silver nanoparticles deposited on a 3-dimensional copper nanowire network and allowed to dry. The resulting nanowires are shown in Figure 5.2. The silver nanopartilces appear to have fused to the copper nanowire frame creating a high surface area structure with minimal mass content of the noble metal. Further investigation with other noble metal nanoparticles is warranted. If this approach is successful with metals such as platinum and palladium. Lower cost catalytic films for catalytic applications may be possible.

A third approach to a synthesizing nobel metal 3-dimensional scaffolds was to galvanically displace copper and nickel nanowires to a more noble metal. An example of this is seen in the nickel-to-gold displacement nanowires Figure 5.3. The same displacement reaction approach was used to convert copper and nickel films to silver, palladium and platinum. By varying the noble metal solution concentration and exposure time a range of material compositions was achieved. Further optimization of this technique should allow for maximal nanowire surface area coverage of the noble metal with minimal noble metal mass.

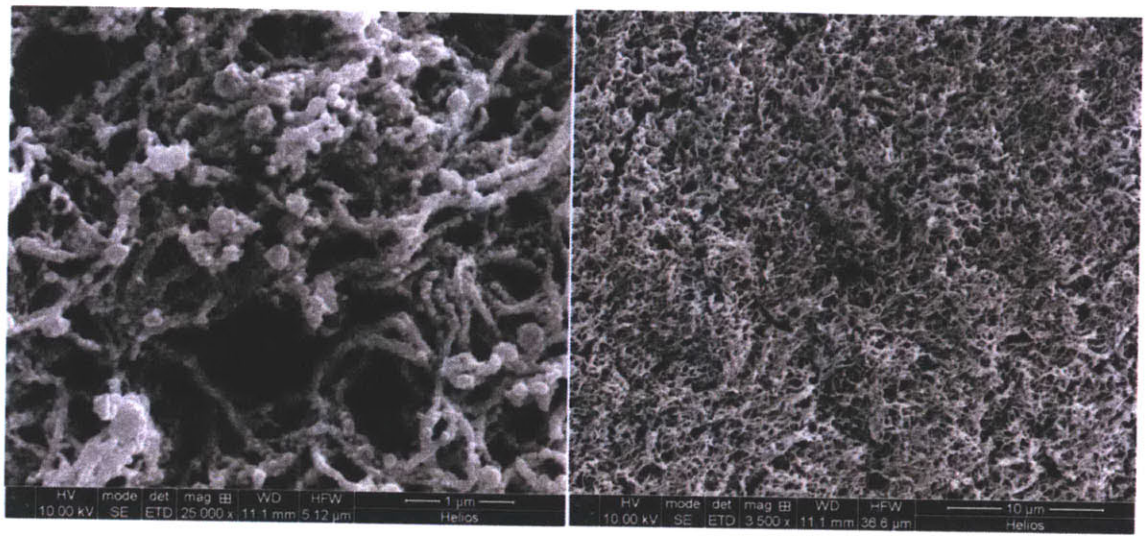

Figure 5.1. 3-dimensional palladium nanowire film.

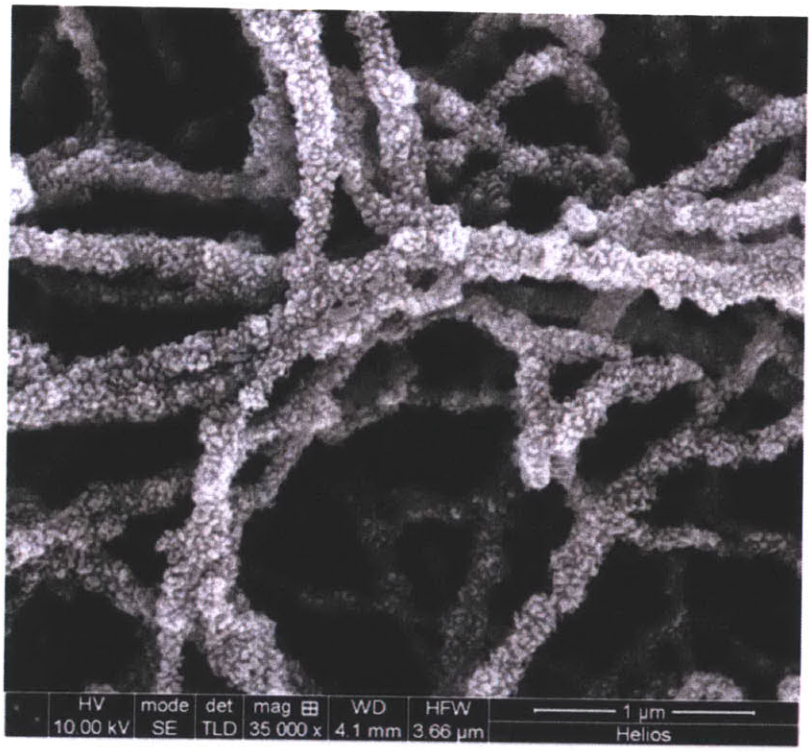

Figure 5.2. Copper nanowires with bound silver nanoparticles. A 3-dimensional copper nanowire film was wetted with a suspension of silver nanoparticles and allowed to dry resulting in the apparent fusion of the silver nanoparticles to the copper scaffold.

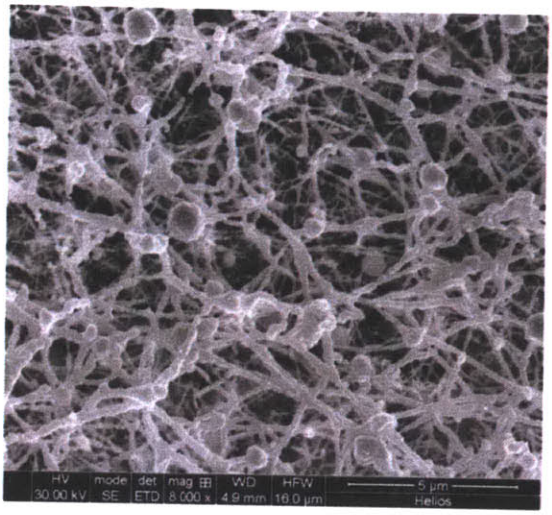

Figure 5.3. Nickel nanowires displaced to gold. Based on EDS composition, gold nanowires had a mass composition of Au:Ni: O of 97.48:0.33:2.19.

5.3.2. Heat Treatment of 3-Dimensional Copper Nanowire Networks

Copper nanowire network films were subject to thermal annealing at 450°C for 30 minutes to test the stability of the porous structure at high temperatures. As seen in Figure 5.4, the nanowires become smoother in morphology and the 3-dimensional porous structure is preserved. At temperatures above 600°C, the nanowires coalesce into large nanoparticles. Thermal stability to at least 450°C raises the possibility for larger crystallite sizes, fewer grain boundaries and consequently higher conductivities.

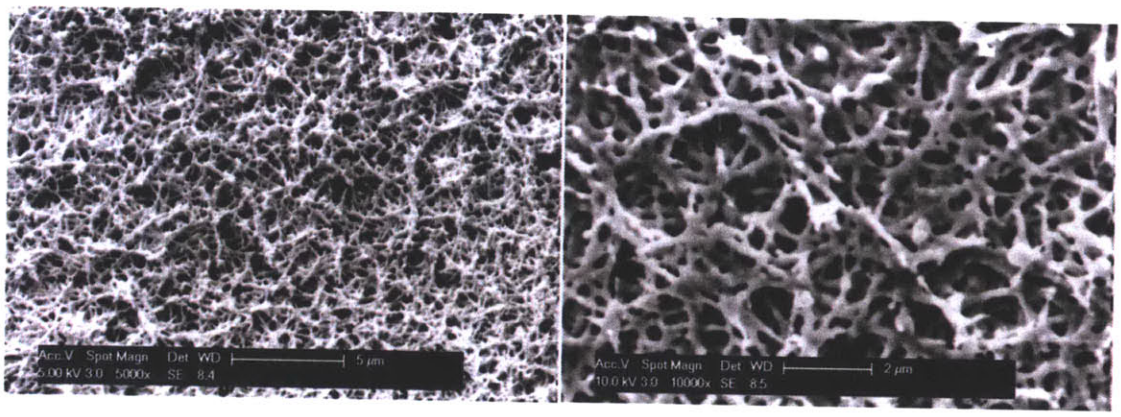

Figure 5.4. Copper nanowire film annealed at 450°C.

5.3.3. Dried Phage Hydrogel Films.

Phage films were prepared by dropcasting E3 and Y21M virus solutions onto untreated silicon substrates. A range of solutions from 10^{13} to 10^{14}pfu/ml was used. Specifically, concentrations of $1x10^{13}$, $3x10^{13}$, $7x10^{13}$, and $1x10^{14}$pfu/ml were dropcast in order to develop a film thickness growth curve for hydrogels of varying concentrations. The virus solutions were cross-linked into hydrogel films for 30 minutes inverted in a 50% glutaraldehyde solution. Subsequent to glutaraldehyde exposure, the hydrogels were rinsed in phosphate buffer solution overnight to remove excess glutaraldehyde from the gels. Phage hydrogels presented a faint white transluscent appearance on the silicon substrate.

Gels were removed from the rinse bath and allowed to dry at ambient temperature, pressure and humidity. After approximately 1-2 hours the gels dried and presented varying degrees of iridescence based on the resulting film thickness. The iridescent appearance was consistent with polymer electrolyte multilayers (PEM) developed from linear polyethylenimine (LPEI) and polyacrylic acid (PAA) with film thicknesses up to a micron.[2] Film thickness and

surface roughness were determined using a profilometer. The resulting film thicknesses were plotted as a function of the initial phage concentrations as shown in Figure 5.5(A). In order to control for possible variations in the thickness of the hydrogels prior to drying, the surface area of the dried films was measured from optical photographs using ImageJ software.[3] The phage deposition solution volume was divided by the dried film surface area to estimate the initial thickness of the deposition solution. The dried film thickness in units of nanometers was divided by the initial phage solution thickness in units of micrometers. The resulting units of nm/μm can be interpreted as the dried film thickness that results from depositing a phage solution with a given solution thickness as measured from the substrate. The porosity of the dried films from phage is shown in Table 5.1 below. Porosity was estimated by comparing the dried film volume with the volume a non-porous, close-packed virus film would occupy based on van der Waals contacts between virus particles. The difference in volumes is taken to be void volume contributing to film porosity.

Table 5.1 Dried Phage Film Porosities

[Phage]	E3	Y21M
7.00E+13	9.1%	22.5%
1.00E+14	35.0%	47.0%

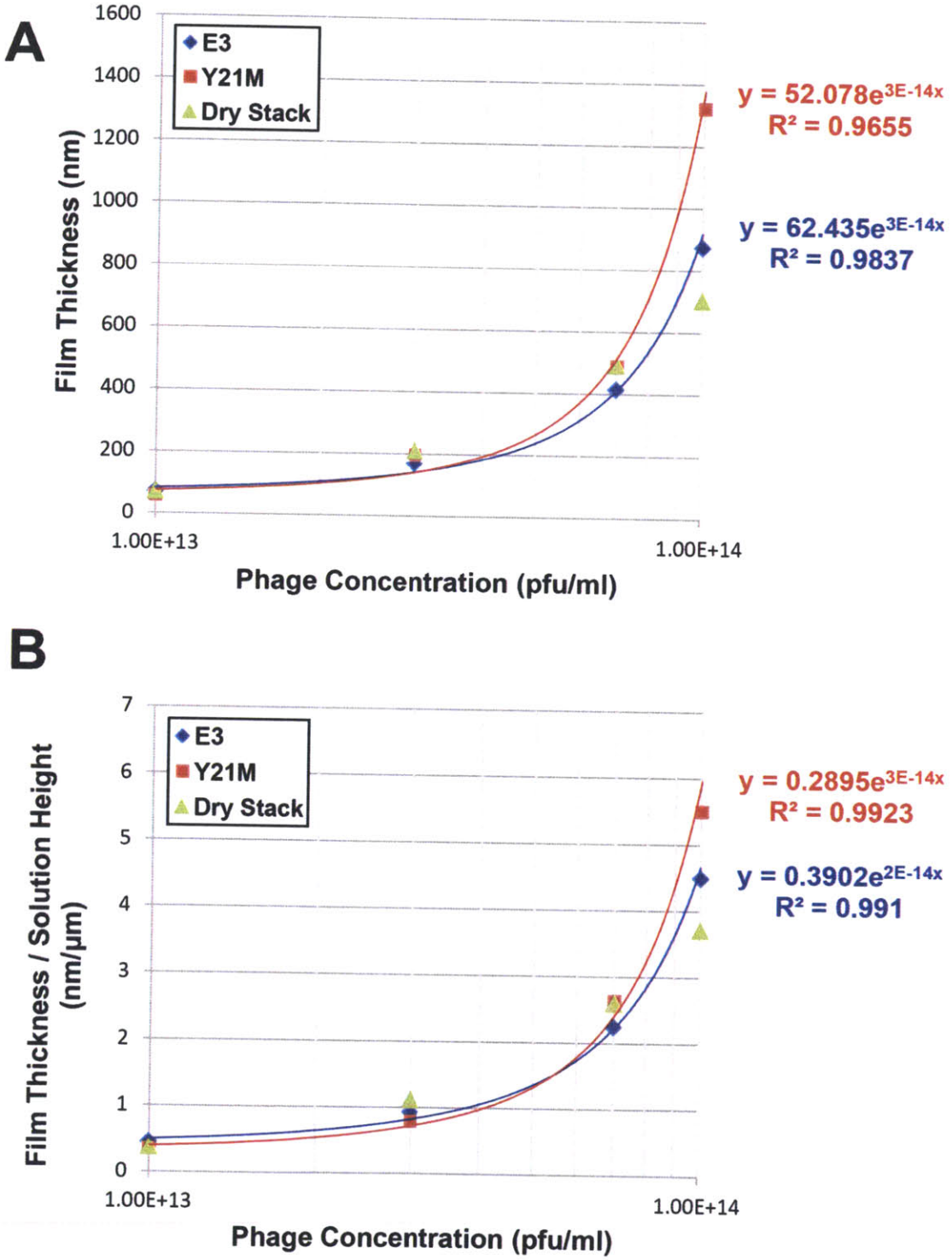

Figure 5.5. Dried film growth curves. A) Dried phage growth curve. Film thickness is plotted as a function of phage concentration. Exponential trend lines are shown for the E3 (blue) and Y21M (red) clones. Green triangles depict a theoretical linear plot of a close packed dried phage. B) Dried phage growth curve. Film thickness normalized by deposition solution height is plotted as a function of phage concentration.

5.4 Conclusions

The M13 virus serves as a versatile unit for assembly into 3-dimensional hydrogel biotemplates to mineralize copper and nickel nanowires. These metal frames, in turn, can be chemically modified through displacement reactions and nanoparticle exposure to create a variety of possible catalytic materials. These approaches use inexpensive metals as the structural and electrical frame of the material, while maximizing noble metal surface area at a minimum of required mass. These approaches coupled with thermal annealing should enable the synthesis of a broad range of materials.

The development of organic phage films via dried hydrogels should enable the further development of multifunctional polymer films. This approach is comparable to a one-step polyelectrolyte film assembly, but with a phage being a single polyelectrolyte. In the future various mixtures of phage clones might be stochastically combined into hydrogels and dried as films in order to tune porosity and binding properties.

5.5 References

1. Chiang, C.Y. et al. Weaving genetically engineered functionality into mechanically robust virus fibers. *Advanced Materials* **19**, 826-+ (2007).
2. Yoo, P.J. et al. Spontaneous assembly of viruses on multilayered polymer surfaces. *Nature Materials* **5**, 234-240 (2006).
3. Rasband, W.S. ImageJ, U. S. National Institutes of Health, Bethesda, Maryland, USA. (1997-2005).